

ALMA MATER STUDIORUM
UNIVERSITÀ DEGLI STUDI DI BOLOGNA

Dipartimento di Fisica e Astronomia

DOTTORATO DI RICERCA IN
ASTROFISICA

Ciclo XXXI

Tesi di Dottorato

SIMULATING HIGHLY NON-LINEAR
DARK MATTER DYNAMICS BEYOND Λ CDM

Presentata da: Matteo Nori

Coordinatore Dottorato:
Francesco Rosario Ferraro

Supervisore:
Marco Baldi

Esame finale anno 2019

Settore Concorsuale: 02/C1 – Astronomia, Astrofisica, Fisica della Terra e dei Pianeti
Settore Scientifico Disciplinare: FIS/05 – Astronomia e Astrofisica

Simulating highly non-linear Dark Matter dynamics beyond Λ CDM

a dissertation presented
by

Matteo Nori

to
The Department of Physics and Astronomy

Doctor of Philosophy
in
Computational Cosmology

Alma Mater Studiorum - Bologna University
Bologna, Italy
April 2019

Simulating highly non-linear Dark Matter dynamics beyond Λ CDM

Abstract

Most of the presently available data regarding the structure and the properties of the Universe are well described within the standard Λ CDM cosmological scenario. However, the underlying assumptions on which the standard framework is based on have been tested only over a restricted range of cosmic scales and cosmic epochs, and extremely severe fine-tuning problems still affect the rather peculiar choice of its parameters. Therefore, a wide range of extended cosmological models have been proposed in the literature to overcome these obstacles. Given the expected excellent high-precision data that will be available in the Precision Cosmology era, it will be possible to test such extensions of the standard cosmological model systematically, to constrain them or rule them out. This will require the theoretical predictions of observable quantities to achieve the same outstanding quality for many competing non-standard cosmologies. In order to obtain such accuracy over a wide range of scales and epochs, the use of large and complex numerical simulations will represent an essential tool. In this thesis, we present the research activity carried out during three years of Ph.D., focused on the implementation and application of alternative cosmological models beyond- Λ CDM in the cosmological hydrodynamical code P-GADGET3. In particular, our work concerned the development of refined numerical routines to perform and improve simulations of two classes of strongly and non-linearly interacting dark matter scenarios: Fuzzy Dark Matter and Growing Neutrino Quintessence models.

Fuzzy Dark Matter (FDM) represents an alternative and intriguing description of the standard Cold Dark Matter (CDM) fluid, able to explain the lack of direct detection of dark matter particles in the GeV sector and to alleviate some of the small-scale tensions that still plague Λ CDM. In these models, the mass of the dark matter particle is so tiny that it exhibits quantum behaviour at cosmological scales. The typical decoherence and interference features, a peculiar characteristic of quantum systems, are encoded by an additional Quantum Potential (QP) in the dark matter dynamics. Given the strong non-linearity of the QP, full numerical simulations

of FDM models at high resolution have been limited so far to the investigation of individual objects with grid-based codes. Alternatively, when turning to cosmologically representative volumes, important approximations had to be introduced in N-body algorithms, due to the otherwise prohibitive computational cost of the simulations. In this thesis, we present the AX-GADGET module that we specifically developed for cosmological simulations of FDM, which is able to achieve high scalability and good performance by computing the QP-induced acceleration through refined Smoothed Particle Hydrodynamics (SPH) routines, with improved schemes to ensure precise and stable derivatives, thereby strongly alleviating the total computational load. Along with an overview of the algorithm, we show the comparison between theoretical predictions and numerical results, both for analytical and cosmological test cases, for which AX-GADGET proves to be a reliable tool for numerical simulations of FDM systems. As an extension of the P-GADGET3 code, AX-GADGET inherits all the additional physics modules implemented up to date, opening a wide range of possibilities to constrain FDM models and to explore degeneracies with other physical phenomena. We then present the results of one major application of the AX-GADGET code, obtained from a simulation suite designed to constrain the FDM mass through Lyman- α forest observations and to characterise the statistical properties of collapsed objects. Both the Lyman- α constraints and the characterisation of structure properties are obtained for the first time in the literature in an N-body set-up without approximating the FDM dynamics. Given the large halo sample available, we extract valuable information about how FDM affects the mass function, the shape and density distribution of dark matter haloes, showing for the first time that massive haloes become even more massive in FDM models by accreting matter at the expenses of smaller haloes.

Moving to the second class of models, we present a independent – and still ongoing – project involving a generalised implementation of strongly coupled scenarios in the P-GADGET3 code. The approach of this new technique is very general and accounts for a wide range of models – like Coupled Dark Energy and Modified Gravity – that involve the solution of a non-linear Poisson equation. We extended to these models the implementation of the so-called Newton-Gauss-Seidel scheme, which is a tree-based iterative solver of differential equations, previously limited to the $f(R)$ gravity case. We apply our generalised method to the case of Growing Neutrino Quintessence (GNQ) models, where the neutrinos are coupled with a dark energy scalar field, that could not be successfully tested so far due to the numerical complexity of the problem. Our implementation improves numerical scalability and is flexible enough to accommodate custom specifications, covering a wide spectrum of models for future investigations.

Contents

I	Introduction	2
1	Modern Cosmology	3
1.1	The Homogeneous Universe	4
1.2	The Inhomogeneous Universe: Linear growth of perturbations . .	15
1.3	The Inhomogeneous Universe: Non-linear growth of perturbations	26
2	The Simulated Universe	30
2.1	Computing the gravitational potential	33
2.2	Evolving in time: Time-integration schemes	36
2.3	From particle to fields: Smoothed Particle Hydrodynamics	40
2.4	P-GADGET3	43
2.5	Beyond Cold Dark Matter	47
II	Fuzzy Dark Matter	49
3	Ultralight bosonic dark matter	50
3.1	Theory and perturbation evolution	52
3.2	Simulation approach in the literature	55
4	AX-Gadget	57
4.1	The algorithm	58
4.2	Analytical tests	65
4.2.1	1D Density Front	66
4.2.2	3D Gaussian distribution	71
4.2.3	Solitonic core	72

4.3	Cosmological tests	75
4.3.1	Quantum Potential effects on dynamics	76
4.3.2	Quantum Potential and initial conditions	81
4.3.3	Performance	86
4.4	Summary of the AX-GADGET implementation	88
5	Lyman- α forest constraint and structure characterisation	91
5.1	Simulation suite	92
5.1.1	Lyman- α forest simulations	93
5.2	Matter and Lyman- α power spectrum	96
5.2.1	Matter Power spectrum	96
5.2.2	Lyman- α forest flux statistics	99
5.3	Structure characterization	103
5.3.1	Numerical Fragmentation	103
5.3.2	Inter-simulations halo matching	108
5.4	Summary on Lyman- α and structure characterisation	117
III Generalised Strongly Coupled models		120
6	Coupled Dark Energy and Modified Gravity	121
6.1	Beyond the Cosmological Constant	122
6.2	$f(R)$ -models and the MG-GADGET implementation	129
6.2.1	The multi-grid Newton–Gauss–Seidel solver	131
6.3	Growing Neutrino Quintessence	137
6.3.1	Our generalised implementation: the GNQ case	139
IV Conclusions		142
7	Discussion & Conclusions	143
7.1	Future Prospects	147
References		169

Part I

Introduction

Scientific revolutions are inaugurated by a growing sense, [...] often restricted to a narrow subdivision of the scientific community, that an existing paradigm has ceased to function adequately in the exploration of an aspect of nature to which that paradigm itself had previously led the way.

Thomas Kuhn

The Structure of Scientific Revolutions (1962)

1

Modern Cosmology

In the introduction of the controversial and irreverent essay *Against Method* (Feyerabend, 1975), the Austrian philosopher Paul Feyerabend claims that “*the history of science, after all, does not just consists of facts and conclusions drawn from facts. It also contains ideas, interpretations of facts, problems created by conflicting interpretations, mistakes, and so on. On closer analysis, we even find that science knows no bare facts at all, but that the facts that enter our knowledge are already viewed in a certain way and are, therefore, essentially ideational*”. Even if he criticized his contemporary fellow epistemologist Thomas Kuhn for retreating from the more radical implications of his theory about the structure of scientific revolutions, they were both deeply inspired by the astonishing paradigm shift occurred in the first decades of the twentieth century, with the rise of the probabilistic quantum theories by Schrödinger and Planck in the micro-world and Einstein’s relativity theories of gravity in the macro-world.

Indeed, Einstein’s work completely re-framed the Newtonian notion of space and time, paving the way for the development of modern scientific cosmology. More than a hundred years later, our understanding of the origin, the evolution, and the eventual fate of the Universe has profoundly expanded. Nevertheless, the current cosmological paradigm has posed even more unanswered questions, emphasizing the lack of a complete picture of the physical nature of the Universe.

In this chapter we will cover the main – in Feyerabend’s words – “*facts*” and “*conclusions drawn from facts*”, as well as the “*interpretations of facts*”, that led to the development of the current standard cosmological model.

1.1 The Homogeneous Universe

In Einstein’s theory of gravity, space and time constitute two complementary aspects of the same geometrical identity so that any event takes place on a four dimensional *space-time* manifold. The distance between two events (t, x, y, z) and $(t + dt, x + dx, y + dy, z + dz)$ in Special Relativity (Einstein, 1905) is given by the line element

$$ds^2 = -c^2 dt^2 + dx^2 + dy^2 + dz^2 \quad (1.1)$$

and it is invariant under coordinate transformation. The properties of the flat space-time of Eq. 1.1 are then extended in General Relativity (Einstein, 1916) to a more generic case, to account for curved geometries that incorporate the geometrical interpretation of the gravity sourced by a massive body

$$ds^2 = g_{ij} dx^i dx^j \quad (1.2)$$

where g_{ij} is the *metric* of space-time and $dx = (ct, x, y, z)$ is the position *quadri-vector**. The two Relativity theories are described through a complex but elegant tensor formalism and have interesting geometrical interpretations. In particular, General Relativity characterises how mass is able to curve space-time, influencing light and particle trajectories in its surroundings.

*The subscripts and superscripts indicate the coordinate index, as in Einstein’s formalism.

On curved manifolds, two vectors that are mutually parallel at a given point will not remain necessarily parallel when they are moved apart, in the same way in which the Eiffel Tower in Paris and its replica in Tokyo are nearly perpendicular to each other, despite both being safely perpendicular to the ground. The distortion of the λ coordinate of vector A , that is parallel transported along the μ component of the basis, is quantified through the covariant derivative

$$\nabla_{\mu} A^{\lambda} = \partial_{\mu} A^{\lambda} + \Gamma_{\mu\nu}^{\lambda} A^{\nu} \quad (1.3)$$

where the $\Gamma_{\mu\nu}^{\lambda}$ coefficients are defined as

$$\Gamma_{\mu\nu}^{\lambda} = \frac{1}{2} g^{\lambda\sigma} (\partial_{\mu} g_{\sigma\nu} + \partial_{\nu} g_{\sigma\mu} - \partial_{\sigma} g_{\mu\nu}) \quad (1.4)$$

and are called the *Christoffel symbols*.

Therefore, if the two parallel vectors are transported along closed circuits, they may point in different directions when they meet again at the origin. Imagine, for example, a closed circuit generated by two vectors X and Y with sides $[tX, tY, -tX, -tY]$ regulated by a generic size parameter t . In the limit of $t \rightarrow 0$, the transformation $R(X, Y)$ experienced by the vector Z transported along such loop is described by the so-called *Riemann curvature tensor* $R_{\mu\nu\sigma}^{\lambda}$

$$R_{\mu\nu\sigma}^{\lambda} X^{\mu} Y^{\nu} Z^{\sigma} = (R(X, Y)Z)^{\lambda} = (\nabla_X \nabla_Y Z - \nabla_Y \nabla_X Z - \nabla_{XY - YX} Z)^{\lambda} \quad (1.5)$$

that can be expressed as

$$R_{\mu\nu\sigma}^{\lambda} = \partial_{\nu} \Gamma_{\mu\sigma}^{\lambda} - \partial_{\sigma} \Gamma_{\mu\nu}^{\lambda} + \Gamma_{\nu t}^{\lambda} \Gamma_{\mu\sigma}^t - \Gamma_{\sigma t}^{\lambda} \Gamma_{\mu\nu}^t \quad (1.6)$$

in terms of the Christoffel symbols. The transformation generated by such geometrical effect is connected with the *Ricci curvature tensor*

$$R_{\mu\sigma} = R_{\mu\nu\sigma}^{\nu} \quad (1.7)$$

whose trace $R = g^{\mu\nu} R_{\mu\nu}$ is the *Ricci curvature scalar*.

In Einstein's theory, the geometry of space-time is entirely described by the Ricci tensor and it is modified by the presence of energy and matter, as elegantly condensed in the Einstein equation

$$R_{\mu\nu} - \frac{1}{2}g_{\mu\nu}R = \frac{8\pi G}{c^4}T_{\mu\nu} \quad (1.8)$$

where G is Newton's constant and the mass and energy distribution sourcing the gravitational potential are enclosed in the stress-energy tensor $T_{\mu\nu}$.

Within a general space-time framework, the analytic solutions of Einstein equation are extremely complex to be derived and, in the first attempts to describe the Universe, two assumptions were introduced. In particular, our role as Earth-based observers was assumed to be unprivileged with respect to other possible observers in the Universe, and combined with the isotropy hypothesis, considering the Universe statistically similar in every direction. The union of the two constitutes the so-called *Cosmological principle*, which implies the homogeneity of the Universe at sufficiently large scales.

The translational and rotational symmetries implied by the Cosmological Principle can be used to rewrite the spatial part of the metric $d\vec{r} = (dx, dy, dz)$ of Eq. 1.2 in spherical coordinates $(dr, d\theta, d\phi)$ as

$$ds^2 = -c^2 dt^2 + a^2(t) \left[\frac{dr^2}{1 - Kr^2} + r^2 (d\theta^2 + \sin^2\theta d\phi^2) \right] \quad (1.9)$$

named Friedmann–Lemaître–Robertson–Walker (FLRW) metric. The *curvature parameter* K has units [L^{-2}] and is related to the topological geometry of the space-time, that can be either flat ($K = 0$), closed ($K > 0$) or open ($K < 0$): in this three geometries, two rays of light that are locally parallel will remain parallel, converge or diverge, respectively. The dimensionless parameter $a(t)$ is the *scale factor* and accounts for the time-dependence of distances, allowing the fabric of space-time to contract or expand.

In fact, we can define the *physical distance* between two points as

$$\vec{r} = a(t) \hat{r} \int \frac{dr}{\sqrt{1 - Kr^2}} = a(t) \hat{r} \begin{cases} \operatorname{arcsinh} r & \text{for } K < 0 \\ r & \text{for } K = 0 \\ \operatorname{arcsin} r & \text{for } K > 0 \end{cases} \quad (1.10)$$

and the *comoving distance* as

$$\vec{x} = \frac{a_0}{a(t)} \vec{r} \quad (1.11)$$

where the 0 subscript refers to the value at present time.

Depending on the specific case, physical processes are more elegantly described in the physical or the comoving frame: in order to recover one from the other it is useful to recall the definition of *total derivative* of a generic function f with n arguments $\{a_1, a_1, \dots, a_n\}$

$$\frac{d}{dt} f(a_1, a_1, \dots, a_n) = \sum_{i=1}^n \frac{da_i}{dt} \partial_i f \quad (1.12)$$

where ∂_i is the *partial derivative*. Since total derivative is invariant under coordinate transformation, we have that

$$\begin{cases} \partial_t f(\vec{r}, t) = \partial_t f(a\vec{x}, t) - \frac{\dot{a}}{a} (\vec{x} \cdot \vec{\nabla}_x) f(a\vec{x}, t) \\ \vec{\nabla}_r = \frac{1}{a} \vec{\nabla}_x \end{cases} \quad (1.13)$$

where we adopt the conventional dot operator \dot{a} to represent the total time derivative.

The velocities in comoving and physical coordinates are

$$\vec{u} = \dot{\vec{x}} \quad (1.14)$$

$$\vec{v} = \dot{\vec{r}} = \dot{a}\vec{x} + a\vec{u} \quad (1.15)$$

respectively, where the factor

$$H(t) \equiv \frac{\dot{a}}{a} \quad (1.16)$$

is the *Hubble function*, named after the American physicist Edwin Hubble, whose value at present time – the *Hubble parameter* H_0 – is often conveniently reduced to the dimensionless variable $h = H_0/(100 \text{ km/s/Mpc})$.

In 1929, Hubble was able to estimate the value of H_0 using the observations of several Cepheid variables collected together with Milton Humason, using the Hooker Telescope located at the Mount Wilson Observatory (Hubble, 1929; Hubble and Humason, 1931). Combining distance measures resulting from the intrinsic Cepheid variability with the velocities, obtained from the Doppler redshift effect of their emission, he was able to prove not only that the objects observed belonged to extra-galactic systems – called *nebulae* at that time – but also that such systems were all moving away from Earth, with velocities proportional to their distance independently from their position in the sky.

The Doppler effect is the observed shift in the wavelength λ of signals emitted by a moving source, that exhibit smaller (*blueshift*) or larger (*redshift*) wavelength with respect to the original one if the source is approaching or receding from the observer, respectively. In cosmology, the signals emitted by a source are redshifted by the expansion of space-time

$$z = \frac{d\lambda}{\lambda} = \frac{dv}{v} \simeq H \frac{dr}{v} = H dt = \frac{da}{a} \quad (1.17)$$

and this can be directly related to the scale factor

$$1 + z = \frac{a_0}{a} \quad (1.18)$$

as the redshift is *de facto* commonly used as a substitute for the scale factor itself.

In Hubble's work, the statistical estimate of H_0 was derived from the linear regression between the physical velocity and the distance

$$\vec{v} \sim H\vec{r} \quad (1.19)$$

exhibited by objects in nearby galaxies under the assumption of constant $H(t) = H_0$. This is considered the first observation of the expansion of the Universe: in fact, it is possible to describe the velocity of each object as

$$\vec{v} = H \vec{r} + a \vec{u} \simeq H \vec{r} \quad (1.20)$$

where the contribution of the comoving velocity \vec{u} is considered to be negligible with respect to the cosmic drift and statistically irrelevant since it should be randomly distributed in the sample.

With the assumptions of the Cosmological Principle, the general metric of the space-time on the left-hand side of Einstein equation Eq. 1.8 can be reduced to a more symmetric and simple form that involves two main components: a curvature K and a scale factor $a(t)$ describing the geometry of the space and its intrinsic expansion rate, respectively.

In order to have a complete picture of evolution of the Universe, let us now turn to the right-hand side of Einstein equation: the stress-energy tensor $T_{\mu\nu}$. It is useful to describe – at first – the energy and matter content of the Universe as a single and perfect fluid, which does not experience conduction ($T_{0,\nu} = T_{\mu,0} = 0$) nor shear stresses ($T_{\mu\nu} = 0 : \mu \neq \nu$), such that the stress-energy tensor reads

$$T_{\mu\nu} = \text{diag}(\rho c^2, P, P, P) \quad (1.21)$$

where ρ and P are the density and pressure of the fluid, respectively.

Solving Eq. 1.8 for the T_{00} component and for its trace $\text{tr}T$, we obtain the two Friedmann Equations (Friedmann, 1924)

$$H^2 = \frac{8\pi G}{3}\rho - \frac{Kc^2}{a^2} \quad (1.22)$$

$$\dot{H} = -4\pi G \left(\rho + \frac{P}{c^2} \right) + \frac{Kc^2}{a^2} \quad (1.23)$$

from which we can derive

$$\frac{\ddot{a}}{a} = -\frac{4\pi}{3}G \left(\rho + 3\frac{P}{c^2} \right) \quad (1.24)$$

to explicit the second derivative of the scalar factor.

Taking the derivative of Eq. 1.22 and substituting it in Eq. 1.23 we find

$$\partial_t \rho + 3H \left(\rho + \frac{P}{c^2} \right) = 0 \quad (1.25)$$

which exemplifies an interesting property of the Universe under study. In fact, the previous equation can be rewritten as the definition of *adiabatic* expansion

$$dU + PdV = 0 \quad (1.26)$$

where we recognize the internal energy $U = \rho c^2 a^3$ and the volume $V = a^3$, meaning that – in this framework – the Universe is a closed system: matter and energy cannot be lost to or gained from an external source.

Let us note from Eq. 1.23 that a static solution of the two Friedmann equations exists, but it requires

$$H = 0 \Leftrightarrow P = -\rho c^2 \quad (1.27)$$

$$\dot{H} = 0 \Leftrightarrow \rho = \frac{3Kc^2}{8\pi G a^2} \quad (1.28)$$

meaning that the density ρ or the pressure P should be negative, even if both are expected to be positive for a standard fluid. This was one of the reasons – among others – that led Einstein to introduce a *cosmological constant* Λ and the relative density component $\rho_\Lambda = \Lambda c^2 / 8\pi G$ through the invariant transformation of coordinates (Einstein, 1917)

$$P \rightarrow \tilde{P} + P_\Lambda \quad (1.29)$$

$$\rho \rightarrow \tilde{\rho} - \rho_\lambda \quad (1.30)$$

that would effectively resemble a fluid with negative pressure $P_\Lambda = -\rho_\Lambda c^2$.

In order to divide the single fluid in several fluid species i , we define each equation of state $P_i = P_i(\rho_i)$ in the form of

$$P_i = w_i \rho_i c^2 \quad (1.31)$$

where w_i is a parameter describing the nature of the fluid component that can be related to the sound velocity $c_{s,i}$

$$w_i = \frac{c_{s,i}^2}{c^2} = \frac{\partial \rho_i P_i}{c^2} \quad (1.32)$$

and to the time evolution of each species density

$$\rho_i = \rho_{i,0} a^{-3(1+w_i)} \quad (1.33)$$

as obtained from Eq. 1.25. Rearranging Eq. 1.26, it is also possible to see that the parameter w_i determines how the internal energy changes with respect to a volume variation

$$\frac{dU_i}{dV} = -P_i = -w_i \rho_i c^2 \quad (1.34)$$

in the case of adiabatic expansion. Therefore, it is possible to identify three main different behaviours:

- *Non-relativistic matter* $w_{mat} = 0 \Rightarrow \rho_{mat} \propto a^{-3}$:
the internal energy is dominated by mass contribution $U_i \simeq m_i c^2$, which is constant in time, implying that the fluid is pressure-less and its density scales as the inverse of the volume;
- *Relativistic matter and radiation* $w_{rad} = 1/3 \Rightarrow \rho_{rad} \propto a^{-4}$:
the redshift effect contributes with an additional a^{-1} factor to the volume scaling, identifying this case as radiation and ultra-relativistic particles in thermal equilibrium;

- *Cosmological constant* $w_\Lambda = -1 \Rightarrow \rho_\Lambda \propto 1$:
this behaviour is consistent with the properties of the cosmological constant of negative pressure and of constant density as previously described.

Since matter, radiation and the cosmological constant density evolutions scale differently with respect to the cosmic expansion, the Universe lifetime can be divided into three eras with respect to the dominant component at each time. Given a non-zero value for $\rho_{mat,0}$, $\rho_{rad,0}$ and $\rho_{\Lambda,0}$, there exist three crossover moments in which the densities of a pair of the species equate. These are identified with the three equality redshifts

- *Matter–Radiation equality* $1 + z_{eq} = \rho_{mat,0}/\rho_{rad,0}$
- *Radiation– Λ equality* $1 + z_{rad,\Lambda} = (\rho_{\Lambda,0}/\rho_{rad,0})^{1/4}$
- *Matter– Λ equality* $1 + z_{mat,\Lambda} = (\rho_{\Lambda,0}/\rho_{mat,0})^{1/3}$

where matter–radiation equality is referred as *equality* conventionally when not specified otherwise. In the degenerate case for which the three redshifts are equal – i.e. $z_{eq} = z_{rad,\Lambda} = z_{mat,\Lambda} \Rightarrow \rho_{mat,0}^4 = \rho_{rad,0}^3 \rho_{\Lambda,0}$ –, there is a transition from radiation to cosmological constant dominated era. A matter dominated era can break through between the two if $\rho_{mat,0}^4 \geq \rho_{rad,0}^3 \rho_{\Lambda,0}$, so that the first era during cosmic evolution is characterised by radiation, followed by matter and later on by the cosmological constant.

To better analyse the relative contribution of the different species to the cosmic evolution let us switch to dimensionless coordinates, in particular defining the useful dimensionless *density parameters* Ω_{mat} , Ω_{rad} and Ω_Λ as

$$\Omega_i = \frac{\rho_i}{\rho_c} \quad (1.35)$$

and *total density parameter* as

$$\Omega_{tot} = \frac{1}{\rho_c} \sum_i \rho_i = \sum_i \Omega_i \quad (1.36)$$

where we defined also

$$\rho_c = \frac{3H^2}{8\pi G} \quad (1.37)$$

as the *critical density*.

The Friedmann equations can be rewritten as

$$1 + \frac{Kc^2}{a^2H^2} = \sum_i \Omega_i \quad (1.38)$$

$$\frac{\ddot{a}}{a} = -\frac{H^2}{2} \sum_i \Omega_i (1 + 3w_i) \quad (1.39)$$

where is underlined the dependence of the curvature K and the scale factor acceleration \ddot{a} on the content of the Universe.

It appears clearly from the previous equations that, in a Universe with only matter and radiation – treated as perfect fluids –, the acceleration of the scale factor is always negative. In fact, three scenarios can be outlined for the expansion dynamics – keeping in mind that Hubble’s result confirmed the cosmic expansion $H_0 > 0$ –, in particular studying how the cosmic acceleration \ddot{a} changes with respect to the relative weight of the cosmological constant in the total energy-matter content of the Universe:

- $\ddot{a} < 0$ for $\Omega_\Lambda < \frac{1}{2}\Omega_{mat} + \Omega_{rad}$: for all the cosmic eras when the cosmological constant is (still) irrelevant, matter and radiation decelerate cosmic expansion.
- $\ddot{a} = 0$ for $\Omega_\Lambda = \frac{1}{2}\Omega_{mat} + \Omega_{rad}$: this case represents the flex point of the accelerated expansion onset and it is eventually reached if a non-zero cosmological constant component exists.
- $\ddot{a} > 0$ for $\Omega_\Lambda > \frac{1}{2}\Omega_{mat} + \Omega_{rad}$: when the cosmological constant becomes the dominant component in the Universe, the Universe expands at an exponentially accelerated pace without end.

It is also possible to link the three different values for the curvature K at each time to the total density parameter Ω_{tot} :

- $\Omega_{\text{tot}} < 1 \Rightarrow K < 0$:
the curvature of space-time geometry induced by the content of the Universe is not enough to compensate the one deriving from cosmic expansion, and it results in an open geometry and ever-expanding Universe.
- $\Omega_{\text{tot}} = 1 \Rightarrow K = 0$:
in this case, all species contributions sum up to the critical density, exactly balancing the expansion and recovering a flat Euclidean geometry.
- $\Omega_{\text{tot}} > 1 \Rightarrow K > 0$:
if the critical density is surpassed, the curvature induced on the space-time overtake the expansion of the Universe and the geometry is closed. A turning point is eventually reached in the case of null cosmological constant $\Omega_{\Lambda} = 0$ and the Universe starts to shrink towards a singularity – often referred to as *Big Crunch* –.

To summarize, the symmetries assumed for the metric of the space-time of General Relativity are combined with the perfect fluid description of the energy-matter content of the Universe into the Friedmann equations, that represent the master equations for the dynamics of an expanding Universe and provide several predictions for the past, present and future evolution of the Universe as well as its intrinsic geometrical properties. The description of the Universe is crucially related to the present value of the Hubble parameter H_0 and the three density parameters $\Omega_{i,0}$, in order to solve

$$\left(\frac{H}{H_0}\right)^2 = \Omega_{rad,0}(1+z)^4 + \Omega_{mat,0}(1+z)^3 + \left(1 - \sum_i \Omega_{i,0}\right)(1+z)^2 + \Omega_{\Lambda,0} \quad (1.40)$$

and get a defined description of cosmic evolution at the background level.

1.2 The Inhomogeneous Universe: Linear growth of perturbations

As detailed in the previous Section, the results obtained through the Friedmann equations are valid as long as the Cosmic principle holds – i.e. if the homogeneous assumption is legitimate – so that the evolution of matter and energy densities can be described through their mean value.

In 1964, Arno Penzias and Robert Wilson, with the Holmdel horn antenna at the Bell Labs in Holmdel Township, serendipitously discovered an electromagnetic emission in the microwave band, isotropically distributed as a micro-wave *background* (Penzias and Wilson, 1965): it was the first observation of the *Cosmic Microwave Background* (CMB) already hypothesized by Alpher *et al.* (1948); Alpher and Herman (1948).

After the discovery of the expansion of the Universe by Hubble, it was still debated whether this result suggested that the Universe was smaller in earlier times, thus implying a singularity for $a \rightarrow 0$ – i.e. the *Big Bang* or, in Lemaître’s words, the *Cosmic Egg* (Lemaître, 1933) –, or that the expansion was not an adiabatic process as stated by Eq. 1.26 and matter and energy were constantly input to reach a *Steady State* (Bondi and Gold, 1948).

It was already evident at the time that, if the Universe was smaller throughout its history, it should also be hotter and denser. Therefore, it exists a moment in the past when the protons and electrons were so energetic to be unable to bound and form atoms, continuously scattering with photons in a hot state called *plasma*, thus effectively impeding light transmission and making the Universe an opaque medium. When the temperature and the density of the plasma lowered enough due to the cosmic expansion, electrons and protons combined into atoms in a process identified as *recombination*, suddenly clearing the path to the photons that eventually were detected by Penzias and Wilson billions of years later and still permeate the Universe.

The observed emission had the characteristic *Planckian* shape of a perfect black body thermal emission with a peak temperature of 2.7 K, as measured by the NASA COBE experiment in 1992 (Smoot *et al.*, 1992). Knowing the temperature required

for the recombination process ($T \sim 3000$ K) and the evolution of radiation temperature during cosmic expansion ($T = T_0(1+z)$), the CMB was identified as the relic radiation emitted during the recombination era when the Universe was approximately 379,000 years old, at redshift $z \sim 1100$, that contributes today to the total energy-matter content with $\Omega_{rad,0} = 9.2 \times 10^{-5}$. Therefore, the discovery of the CMB confirmed that the homogeneity approximation was correct and that the Universe has expanded from a *Hot* Big Bang state, contradicting the Steady State hypothesis.

The homogeneity of the CMB, however, was expected to break down by tiny fluctuations derived from the dynamical equilibrium of the plasma, since a perfectly homogeneous Universe would not feature the inhomogeneities that eventually turn into planets, galaxies and the structures surrounded by empty space we see today. The presence of acoustic oscillations was predicted as a possible effect in the CMB in the late 1960s (Sakharov, 1966) and further studies (Bond and Efstathiou, 1984; Efstathiou and Bond, 1986; Hu and White, 1996) investigated possible methods to use the scale of inhomogeneities as a *standard ruler* as we will describe below (Kamionkowski *et al.*, 1994; Jungman *et al.*, 1996).

Since it is possible to relate the temperature fluctuations with the density ones, in order to study the deviations of T and ρ from the homogeneous background solutions T_b and $\rho_b(a) = \rho_{b,0} a^{-3}$, we define the *temperature contrast*

$$\Delta(\vec{x}) = \frac{T(\vec{x}) - T_b}{T_b} \quad (1.41)$$

and the *density contrast*

$$\delta(\vec{x}, a) = \frac{\rho(\vec{x}, a) - \rho_b(a)}{\rho_b(a)} \quad (1.42)$$

in each point \vec{x} of the space. Moreover, since fluctuations of the early Universe distribution are nearly acoustic, it is more convenient to perform perturbation analysis in Fourier space, where the density contrast reads

$$\delta_k = \frac{1}{(2\pi)^3} \int d\vec{x} \delta(\vec{x}) e^{i\vec{k}\cdot\vec{x}} \quad (1.43)$$

and its 2-point correlation function is

$$P(k) \equiv \langle \delta_k^2 \rangle = \langle \int d(\vec{x} - \vec{x}') \delta(\vec{x}) \delta(\vec{x}') e^{i\vec{k} \cdot (\vec{x} - \vec{x}')} \rangle \quad (1.44)$$

often referred as *Power Spectrum* (PS)[†], where the angle brackets $\langle \rangle$ indicate ensemble average over smaller patches of the Universe volume. The 2-point correlation function related to temperature perturbations is more conveniently represented in spherical coordinates, thus called *Angular Power Spectrum*, where the polar and azimuthal angles (θ, ϕ) are expressed through the multiple moment and order (l, m) of the spherical harmonic

$$C_l = \langle \frac{1}{2l+1} \sum_{m=-l}^l |\Delta_{lm}|^2 \rangle \quad (1.45)$$

and the angular scale can be derived through $180^\circ/l$.

In Fig. 1.1 the projected sky map of the δ^T fluctuations as seen by the Planck experiment – *upper panel*, red and blue for positive and negative values, respectively – and the relative Angular PS are represented, the latter plotted in terms of $T_0^2 l(l+1) C_l$ as function of both l and the angular scale of separation – *bottom panel* –.

The Angular PS has very distinctive features, mainly represented by an initial slope, several peaks of different heights and a damping tail. These features, called *Barionic Acoustic Oscillations* (BAO), can be described within a single theoretical picture in which baryonic matter and radiation acoustically oscillate in the primordial plasma, driven by the opposite influence of gravity and radiation pressure. Odd and even peaks represent the maximal compression and rarefaction states due to gravitational attraction and pressure repulsion, respectively[‡]. The CMB photons, once recombination occurs, freely stream through the Universe retaining information on this oscillatory pattern.

The correlation between two points of the CMB map is a function of their angu-

[†]Note that $P(k) = P(|\vec{k}|)$ because of isotropy.

[‡]Compression and rarefaction states have positive and negative temperature fluctuations, but their correlation is always a positive quantity.

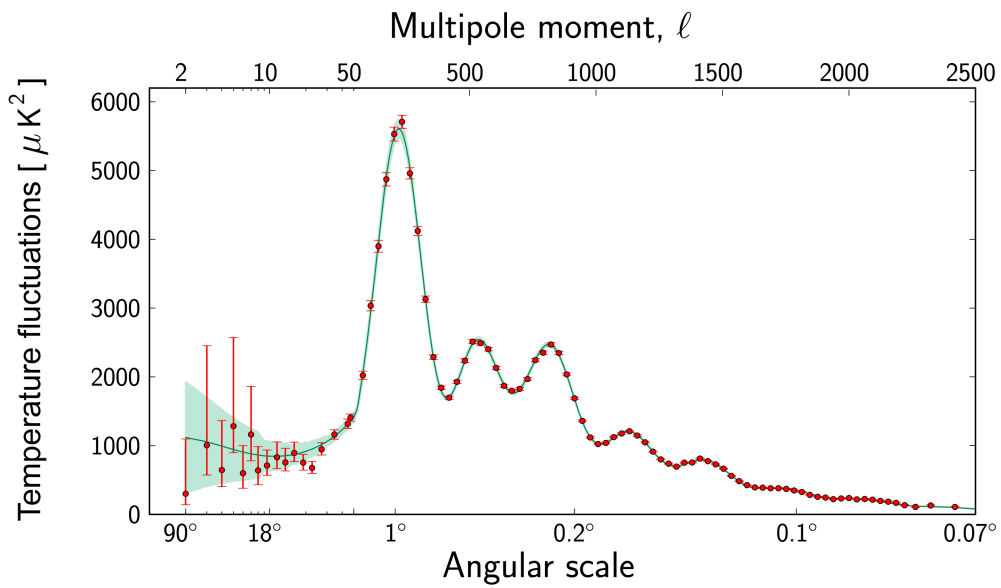
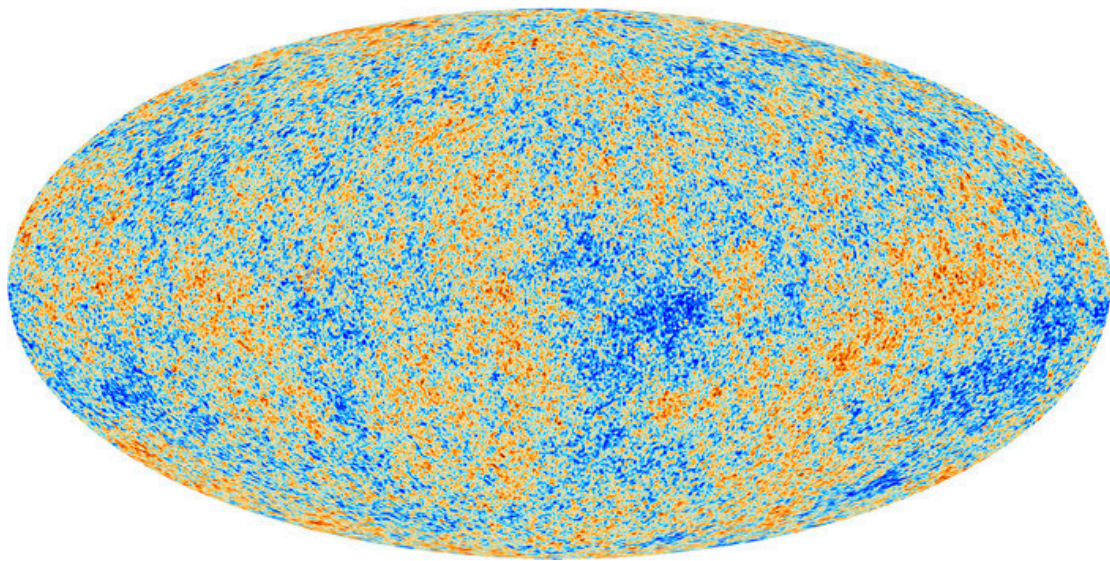


Figure 1.1: The Cosmic Microwave Background: a map of the temperature deviations from the mean value (*top panel*) and the Angular Power Spectrum of such fluctuations (*bottom panel*). Credit: ESA and PLANCK Collaboration ([Planck Collaboration, 2018](#))

lar separation compared to the size of the Universe at the time of recombination, approximately corresponding to $l \sim 50$ at $z \sim 1100$: for example, points with small angular separation – $l \gg 50$ – experienced several oscillation cycles while very distant points – $l \ll 50$ – did not even start to oscillate.

In this sense, the shape at low multipoles still holds information of the primordial spectrum of the early Universe, which is well described by a (nearly) scale invariant relation

$$C_l = A_l (l/l_0)^{n_s-1} \quad (1.46)$$

that translates into a primordial matter PS

$$P(k) = A_s (k/k_0)^{n_s} \quad (1.47)$$

where the parameters A_s (A_l) and n_s representing the *scalar (angular) amplitude* and the *scalar spectral index*, respectively, can be fitted to the data.

The first peak represents the leading compressed state given by matter gravitational in-fall and was observed for the first time by the high-altitude balloon experiment BOOMERanG flying around the Antarctic South Pole in the years 1998-2003 (de Bernardis *et al.*, 2000; Masi *et al.*, 2002). Given the size of the Universe, its age, matter and radiation content, it is possible to calculate the expected moment $l_{\text{first}}^{\text{exp}}$ of this first peak at recombination and use it as a *standard ruler*. Therefore, any discrepancy between the observed value $l_{\text{first}}^{\text{obs}}$ and the theoretical one would indicate a curvature of the space-time K that modified the path of CMB photons, either shrinking – $l_{\text{first}}^{\text{obs}} < l_{\text{first}}^{\text{exp}}$ – or expanding – $l_{\text{first}}^{\text{obs}} > l_{\text{first}}^{\text{exp}}$ – the projected size of such signal. Hence, with the use of the first peak only it was possible to fix the curvature K to good precision; however, it was impossible to break down the contribution of each species represented by the density parameters Ω_i , for which exploiting higher order peaks is required.

The second peak denotes the first bounce induced by radiative pressure and was captured by the WMAP satellite in 2001 (Bennett *et al.*, 2013). In a plasma where the electrons and protons contribution is negligible with respect to radiation, the first and the second peak would have the same height in an almost symmetric state,

but this is not the case: the symmetry, in fact, is broken by gravity, that enhances the collapse (first peak) with respect to the rarefaction (second peak). Therefore, the ratio between the first two peaks is sensitive to the relative abundance of the species belonging to the plasma.

If the Universe at recombination consisted only in plasma, the other acoustic peaks would be a sequence of exponentially decaying higher order harmonics of the first and the second peak, where the damping originates from the photon random-walk diffusion in the recombination process that effectively suppresses temperature correlation above $l_S \gtrsim 800$ – called *Silk damping*, after the British astrophysicist Joseph Silk (Silk, 1968) –.

The measurement of higher order peaks, performed by the Planck satellite from 2009 to 2018, highlighted an excess power in the third peak and a lack of power in the tail with respect to the primary and secondary peaks. Since the third peak is related to the matter re-collapse after the first acoustic oscillation, a higher power in this peak suggests that the gravitational well originated with the first collapse was not entirely restored by radiation pressure bounce. Such asymmetry can be explained with the addition of another fluid that is coupled gravitationally with the plasma but does not experience radiative pressure, enhancing consecutive matter in-falls, which can be associated with a form of *dark matter*.

While – at the turn of the third millennium – the CMB was providing an impressive amount of crucial information about the early and present Universe, two independent projects were able to prove that the rate of expansion of the Universe is not constant and is indeed *accelerated*. In 1998 the Supernova Cosmology Project (Perlmutter *et al.*, 1999; Schmidt *et al.*, 1998) at Lawrence Berkeley National Laboratory and the High-Z Supernova Search Team (Riess *et al.*, 1998) at the Australian National University both used Supernovae of type Ia to extend Hubble’s diagram to more considerable distances, observing a deviation at high redshifts from the linear law that implied a variation of the rate of expansion. Supernovae Ia, as the Cepheid variables, are considered *standard candles* as their distance can be inferred through their luminosity properties and the hydrogen and silicon lines of the emitted spectrum can be used to determine their redshift. The distance-redshift relation

obtained by the high- z Supernovae was consistent with an accelerating expansion and was best fitted by the combination of the density parameters $\Omega_{mat} \sim 0.3$ and $\Omega_{\Lambda} \sim 0.7$ when combined with CMB results.

By the time of this measurement, other observations spanning through many orders of magnitude in scale were compatible with the presence of a *cold* and *dark* form of matter (CDM) – a not-strongly electromagnetically interacting particle or a gravitational *quid* that mirrors the effect of such fluid –. These are related to dynamical properties of systems, as e.g. the inner dynamics of galaxy clusters (Zwicky, 1937; Clowe *et al.*, 2006) and the rotation curves of spiral galaxies (Rubin *et al.*, 1980; Bosma, 1981; Persic *et al.*, 1996), to the gravitational impact on the underlying geometry of space-time, as strong gravitational lensing of individual massive objects (Koopmans and Treu, 2003) and the weak gravitational lensing arising from the large-scale matter distribution (Mateo, 1998; Heymans *et al.*, 2013; Planck Collaboration *et al.*, 2015; Hildebrandt *et al.*, 2017), as well as on the clustering of luminous galaxies (see e.g. Bel *et al.*, 2014; Alam *et al.*, 2017), on the abundance of massive clusters (Kashlinsky, 1998) and their large-scale velocity field (Bahcall and Fan, 1998).

To summarise, the CMB Angular PS and the Supernovae Ia projects provided an incredible source of information regarding the past and present Universe. It allowed to estimate the density parameters Ω_{rad} , Ω_{mat} – in its components Ω_{bar} and Ω_{cdm} –, the curvature K , the cosmological constant density contribution Ω_{Λ} and equation of state w_{Λ} , as well as the present value of the Hubble parameter H_0 , the age of the universe and the primordial PS scalar parameters A_s and n_s . The parameters mentioned above are reported in Tab. 1.1 as measured by the 2018 release of the Planck collaboration results.

The theoretical cosmological framework originated by these results is called Λ -CDM, and describe the Universe as composed of radiation and standard baryonic matter, together with cold and *dark matter* – that enhances the gravitational collapse and drives structure formation – and a non-zero cosmological constant Λ with equation of state $w_{\Lambda} = -1$, generally called *dark energy*, prompting the late-time cosmic expansion acceleration.

As seen in the previous paragraphs, the CMB Angular PS is consistent with a primordial density PS in the form of

$$P(k) = A_s k^{n_s} \quad (1.48)$$

where the exponent n_s estimated by Planck (Planck Collaboration, 2018) is very close, even if not equal, to unity. A value of $n_s = 1$ is characteristic of a perfect scale-invariant system, where the perturbations are equally likely to arise irrespectively of the scale considered. The scale-invariance of the primordial PS and the possible deviations from it are intimately connected with the properties of the Universe at early times.

The flatness of the space-time, the overall temperature homogeneity of the CMB and the near scale invariance of its perturbations could all be considered curious and peculiar properties from an *a priori* point of view. Since they require a particular set of cosmological parameters that in principle could have any value, such coincidence poses a *fine-tuning* problem to the standard cosmological model. Due to the cosmic expansion, progressively more and more regions of the Universe are casually connected: it is natural to wonder how previously separated regions shared the same temperature and were characterised by energy-matter content that adds up exactly to the critical density preserving the Universe flatness.

It is now commonly accepted that approximately between 10^{-36} and 10^{-32} seconds after the Big Bang the Universe experienced a remarkably rapid exponential expansion by a factor $\sim 10^{26}$. A similar mechanism would have put in causal contact – thus in thermal equilibrium, given enough time – very distant regions in the Universe and would have also stretched any given initial curvature to an almost flat ge-

Table 1.1: Cosmological parameters as measured (or derived) by the Planck Collaboration in combination with BAO and Supernovae Ia measurements (see Planck Collaboration, 2018, for detail).

$\Omega_{rad,0}$	$\Omega_{bar,0}$	$\Omega_{cdm,0}$	$\Omega_{\Lambda,0}$	w_{Λ}
$(9.2 \pm 0.2) \times 10^{-5}$	0.0490 ± 0.0007	0.261 ± 0.004	0.689 ± 0.006	-1.03 ± 0.03
Kc^2/\dot{a}_0^2	h	Age [Gyr]	$A_s \times 10^9$	n_s
0.001 ± 0.002	0.677 ± 0.004	13.78 ± 0.02	2.10 ± 0.03	0.967 ± 0.004

ometry. The idea of such cosmic *inflation* was proposed by Alan Guth (Guth, 1981), Andrei Linde (Linde, 1982) and Alexei Starobinsky (Starobinsky, 1982) among others. In these models, the Universe faced a phase transition, described by the dynamical evolution of a scalar field – called *inflaton* – under the influence of a potential with multiple minima. In this picture, inflation is the exponential expansion of the Universe induced by the shift of the field from a local minimum of the potential to another one. However, despite being commonly accepted and consistent with data, experimental confirmation of the particular physical mechanism have yet to be found, and many inflationary models are still competing.

The set of equations that defines the density and velocity evolution in comoving coordinates of the matter fluid after recombination is

$$\left\{ \begin{array}{ll} \dot{\rho} + 3H\rho + \vec{\nabla} \cdot (\rho\vec{u}) = 0 & \text{Continuity Equation} \\ \dot{\vec{u}} + 2H\vec{u} + (\vec{u} \cdot \vec{\nabla})\vec{u} = -\frac{\vec{\nabla}P}{a^2\rho} - \frac{\vec{\nabla}\Phi}{a^2} & \text{Euler Equation} \\ P = P(\rho) & \text{Equation of state} \\ \nabla^2\Phi = 4\pi Ga^2(\rho - \rho_b) & \text{Poisson Equation} \end{array} \right. \quad (1.49)$$

which is closed by the background evolution of the Hubble function of Eq. 1.40; the variable Φ represents the gravitational potential that satisfies the usual Poisson equation (Peebles, 1980).

The stationary – but unstable – solution of this system is a perfectly homogeneous density distribution

$$\left\{ \begin{array}{l} \rho(\vec{x}) = \rho_b = \rho_{b,0} a^{-3} \\ u(\vec{x}) = 0 \\ P = \text{const} \\ \Phi = 0 \end{array} \right. \quad (1.50)$$

which is exactly what defines our background solution.

We are interested now in perturbing such background solution, in order to study the linearised evolution of the density contrast $\delta(a)$ defined in Eq. 1.42, which will be valid only in the regime of *small* perturbations $|\delta| \ll 1$ (for a complete review on the growth of linear density perturbation see e.g. [Peebles, 1993](#); [Peacock, 1999](#), to which we refer for details). If we take the time derivative of the Continuity Equation, apply the divergence of the Euler Equation and combine the two, substituting the pressure and gravitational potential, we obtain

$$\ddot{\delta} + 2H\dot{\delta} + \frac{c_s^2}{a^2}\nabla^2\delta - 4\pi G\rho_b\delta = 0 \quad (1.51)$$

that, expressed in Fourier space using the definition in Eq. 1.43, reads

$$\ddot{\delta}_k + 2H\dot{\delta}_k + \delta_k \left(\frac{k^2 c_s^2}{a^2} - 4\pi G\rho_b \right) = 0 \quad (1.52)$$

that describes the linear evolution of density perturbation.

This equation features a stationary solution, identified by a periodic density perturbation characterized by

$$\frac{2\pi}{k_J} = \lambda_J = \frac{c_s}{a} \sqrt{\frac{\pi}{G\rho_b}} = \frac{2\pi c_s}{aH} \sqrt{\frac{2}{3\Omega_m}} \quad (1.53)$$

called *Jeans* length, that represents the scale at which the collapse induced by gravity is balanced by the fluid pressure.

As a reference, let us focus on the case of a pressure-less matter fluid, for which $c_{s,mat}^2 = c^2 w_{mat} = 0$. It is interesting to notice that for a static Universe – i.e. $H = 0$ –, Eq. 1.52 reduces to

$$\ddot{\delta}_k = 4\pi G\rho_{b,0} \delta_k \quad (1.54)$$

whose solution is given by the linear combination of

$$D_+(k, t) = \delta_{k,0} e^{+t\sqrt{4\pi G\rho_{b,0}}} \quad (1.55)$$

$$D_-(k, t) = \delta_{k,0} e^{-t\sqrt{4\pi G\rho_{b,0}}} \quad (1.56)$$

where $D_+(k, a)$ and $D_-(k, a)$ are the density perturbation *growing* and *decaying* mode, respectively. In this case, the growth of perturbation is exponential in time.

Instead, in the case of an expanding Universe and – in particular – in the matter dominated era $\Omega_{mat} \simeq 1$, we have that the Hubble function obtained from Eq. 1.40 satisfies

$$H = H_0(a/a_0)^{-3/2} \Rightarrow a = a_0 (t/t_0)^{2/3} \quad (1.57)$$

and the solution of Eq. 1.52 is a linear combination of

$$D_+(k, a) = \delta_{k,0} a(t) \quad (1.58)$$

$$D_-(k, a) = \delta_{k,0} a(t)^{-3/2} \quad (1.59)$$

where the growth of perturbation is now proportional to the scale factor a . The growth is slower with respect to the exponential one of the static Universe, since the gravitational collapse of structures has to overcome the expansion of space-time and the two mechanisms have opposite effect on structure formation[§].

It is useful to recall that the CMB temperature fluctuations are of the order 10^{-5} and can be mapped into baryonic density fluctuations of comparable intensity. If the total matter content of the Universe consisted in baryons exclusively, the density perturbation would have grown from $\delta \sim 10^{-5}$ at recombination – happened at $z \sim 1100$ – to $\delta \sim 10^{-2}$ at the present day, thus implying the complete linear evolution of perturbations and the absence of non-linear structures in the present Universe.

Such estimation is quite heuristic, but it well illustrates the need of a gravitational mechanism that is able to accelerate *baryonic* matter collapse into the complex structures that we observe and are part of today: this is one of the primary motivation supporting the existence of *non-baryonic* dark matter.

[§]For this reason, the friction term $2H\delta_k$ is sometimes referred as *Hubble drag*.

1.3 The Inhomogeneous Universe:

Non-linear growth of perturbations

On an analytical level, it is quite difficult to venture beyond the linear approximation and solve exactly the evolution of density perturbations when these become comparable, or exceed, the background density value. Nevertheless, it exists a simple and integrable model that describes the formation of bounded gravitational structures, called *Spherical collapse* model (Gunn and Gott, 1972). For a detailed description of the model we are here going to review see e.g. Peebles (1993); Coles and Lucchin (2002).

Imagine to carve an over-dense spherical region in a spatially flat and matter-dominated universe – i.e. $\Omega_{mat,0} \simeq 1$ –: the growth of the spherical density is independent from the background solution and effectively evolves as if it was a sub-Universe with its own density parameter $\tilde{\Omega}_{mat,0} > 1$ and, consequently, positive curvature. In this framework, the background evolution of such sub-Universe is described by Eq. 1.40 and it reads

$$H = H_0 \left[\tilde{\Omega}_{mat,0} R^{-3} + (1 - \tilde{\Omega}_{mat,0}) R^{-2} \right]^{1/2} \quad (1.60)$$

where R is the analogue of the scale factor a for the sub-Universe and t is characteristic time of the collapse. It is possible to express Eq. 1.60 in the parametric form

$$\begin{cases} R(\theta) = A(1 - \cos \theta) \\ t(\theta) = B(\theta - \sin \theta) \end{cases} \quad (1.61)$$

through the dimensionless *development angle* parameter $\theta \in [0, 2\pi]$ and two factors

$$\begin{cases} A = R_0 \frac{\tilde{\Omega}_{mat,0}}{2(\tilde{\Omega}_{mat,0} - 1)} \\ B = \frac{\tilde{\Omega}_{mat,0}}{2H_0(\tilde{\Omega}_{mat,0} - 1)^{3/2}} \end{cases} \quad (1.62)$$

that are defined by the boundary condition at $R = R_0$ and $H = H_0$.

It is clear from Eq. 1.61 that the over-density expands until it reaches a turn-around point, defined by

$$R_{max} = 2 A \quad (1.63)$$

$$t_{max} = \pi B \quad (1.64)$$

corresponding to the scale factor

$$R_{max} = \left(\frac{3}{2} H_0 t_{max} \right)^{2/3} = \left(\frac{3\pi}{4} \tilde{\Omega}_{mat,0} \right)^{2/3} (\tilde{\Omega}_{mat,0} - 1)^{-1} \quad (1.65)$$

After t_{max} , it starts to fold back and eventually ends at the final collapsed

$$R_{col} = 0 \quad (1.66)$$

$$t_{col} = 2\pi B \quad (1.67)$$

singularity state.

The density ratio between the collapsing object and the background evolves as

$$\frac{\rho}{\rho_b} = \frac{\tilde{\Omega}_{mat,0} \rho_c / R^{-3}}{\rho_c / a^{-3}} = \tilde{\Omega}_{mat,0} \left(\frac{a}{R} \right)^3 \quad (1.68)$$

that for the turn-around point is

$$\frac{\rho_{max}}{\rho_b} = \frac{9\pi^2}{16} \simeq 5.55 \quad (1.69)$$

meaning that a spherical perturbation is 555% more dense than the background when it enters the collapsing phase.

In this simple model there is no pressure to prevent the final singularity state. However, the singular state is not physically reached and the collapse stops once the *virial condition*

$$2 \mathcal{K} = -\mathcal{U} \quad (1.70)$$

is satisfied, where \mathcal{K} and \mathcal{U} are the kinetic and potential energy of the system, respectively. Therefore, after virialization, $R(t > t_{vir})$ simply saturates to the constant value R_{vir} . For a spherical configuration, the potential energy is

$$\mathcal{U}(R) = -\frac{3GM^2}{5R^2} \quad (1.71)$$

that accounts for the total energy $\mathcal{E} = \mathcal{U} + \mathcal{K}$ at $t = t_{max}$, since at the turn-around point the sphere stands still – i.e. $\dot{R}_{max} = 0 \Rightarrow \mathcal{K}(R_{max}) = 0$ –. In this process the total energy is conserved, thus we can easily retrieve the kinetic energy of the virialized state to obtain the scale relation

$$R_{vir} : 2\mathcal{K}(R_{vir}) = 2[\mathcal{U}(R_{max}) - \mathcal{U}(R_{vir})] \stackrel{!}{=} -\mathcal{U}(R_{vir}) \Rightarrow R_{vir} = \frac{R_{max}}{2} \quad (1.72)$$

that characterizes such state.

Using the definition of Eq. 1.61, virialization happens at

$$\theta_{vir} : A(1 - \cos \theta_{vir}) = A \wedge (\theta_{vir} > \pi) \Rightarrow \theta_{vir} = \frac{3\pi}{2} \quad (1.73)$$

that correspond to a time interval of

$$\frac{t_{vir}}{t_{max}} = \left(\frac{a_{vir}}{a_{max}} \right)^{3/2} = \left(\frac{3}{2} + \frac{1}{\pi} \right) \simeq 1.81 \quad (1.74)$$

The density contrast with the background is

$$\frac{\rho(t = t_{vir})}{\rho_b} = \frac{\rho_{vir}}{\rho_b} = \frac{\rho_{max}}{\rho_b} \left(\frac{R_{vir}}{R_{max}} \right)^3 \left(\frac{a_{vir}}{a_{max}} \right)^3 = \frac{9\pi}{4} (3\pi + 2) \simeq 145 \quad (1.75)$$

in the virialized state and

$$\frac{\rho(t = t_{col})}{\rho_b} = \frac{\rho_{col}}{\rho_b} = \frac{\rho_{max}}{\rho_b} \left(\frac{R_{vir}}{R_{max}} \right)^3 \left(\frac{a_{col}}{a_{max}} \right)^3 = 18\pi^2 \simeq 178 \quad (1.76)$$

at the collapse time.

The physical consequence that can be drawn from this simple but useful model is

that perturbations can be considered gravitationally bound in non-linear structures when they become 150 – 180 times denser with respect to the background density.

The extent of the failure of linear extrapolation can be appreciated if we contrast the exact non-linear density ratio with the one obtained by linearisation

$$\left. \frac{\rho}{\rho_b} \right|_{lin} = 1 + \frac{3}{20} \left(6\pi \frac{t}{t_{max}} \right)^{2/3} \quad (1.77)$$

that for the turn-around and final times are

$$\left. \frac{\rho_{max}}{\rho_b} \right|_{lin} = 1 + \frac{3}{20} (6\pi)^{2/3} \simeq 2.06 \quad (1.78)$$

$$\left. \frac{\rho_{col}}{\rho_b} \right|_{lin} = 1 + \frac{3}{20} (12\pi)^{2/3} \simeq 2.686 \quad (1.79)$$

meaning that the linear break down is already significant at the time of turn-around.

To summarise, the spherical collapse represents a valuable analytical result that describes how collapsed systems form in an expanding Universe. Even if the scaling relations obtained as well as the timings and the order of magnitude of density and size as compared to the background can be used in observable estimations, this solution refers to a highly idealised set-up. A physical cosmological system features multiple perturbations at various scales with no particular symmetry, thus hindering the possibility to solve the density evolution analytically. Moreover, we showed that the linear approximation might deviate seriously from the exact non-linear solution, hence representing a valid alternative only at early times and on large scales. For this reasons, starting from the '60s, the exploration of the non-linear regime relied more and more on a different tool that has proven to be essential in the investigation of the Universe evolution: numerical simulations.

2

The Simulated Universe

The dramatic improvements of our understanding of the Cosmos have prompted by the comparison between ground-breaking observational data – e.g. the Hubble Cepheids observation, the CMB and the results of the Supernovae Ia projects – with the forecast of the theoretical models of the Universe. However, in order to fully exploit the tremendous increment of the quantity and quality of observational data that new technologies allow for, it is required to have equally reliable and precise theoretical predictions of the key observables of interest.

The impossibility to rely on robust and general analytical results in the non-linear regime led to the implementation of numerical simulations that, with the thriving of computational power, now play a crucial role in the estimation of cosmological observables regarding the formation and evolution of collapsed systems and the expected forecast related to future experiments design.

In particular, numerical simulations significantly contributed to the establish-

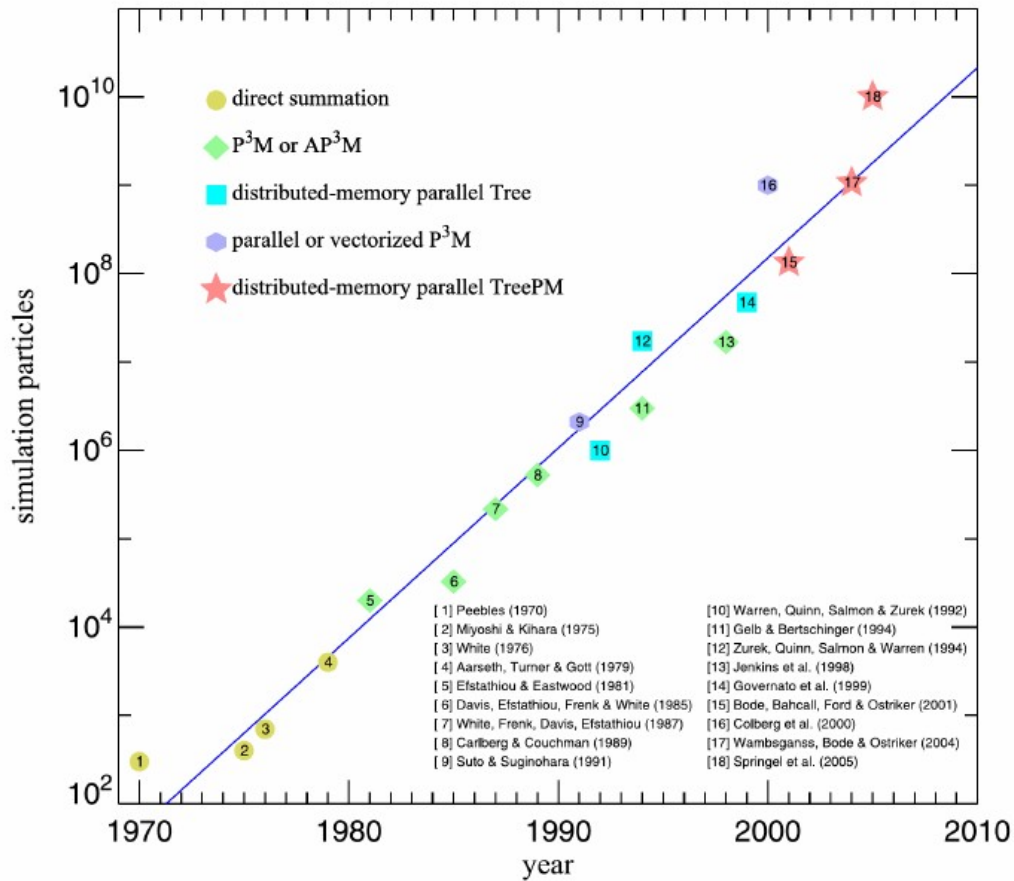


Figure 2.1: The most important cosmological simulations from 1970 to 2010 are plotted year-wise against their particle number. The numerical strategies related to the gravitational potential evaluation are represented by the different marker as described in the legend. Credit: Debora Sijacki

ment of Λ CDM as the standard cosmological scenario, providing decisive predictions on the non-linear structure formation driven by the presence of CDM and on the role of dark energy in the late-time accelerated expansion of the Universe.

The combined effects of the development of advanced numerical methods and the availability of increasing technological resources have induced the exponential evolution of simulation complexity and predictive power. The accuracy of numerical simulations of collapsed objects dynamics and large-scale structures formation has experienced a striking improvement during the years, as schematically portrayed in Fig. 2.1, where the most important simulations *milestones* in a 40-year lapse of time are plotted against their number of particles – i.e. the smallest singular components resolved in the system –.

Consistently with the resolution obtainable at the time, several systems have been the target of N-body simulations in the literature. First were investigated the formation and the dynamics of galaxy clusters (see e.g. [Aarseth, 1963](#); [Peebles, 1970](#); [White, 1976](#); [Aarseth *et al.*, 1979](#); [Frenk *et al.*, 1983](#); [Davis *et al.*, 1985](#); [White *et al.*, 1987](#)) as well as their density and velocity statistical analysis (see e.g. [Miyoshi and Kihara, 1975](#); [Efstathiou and Eastwood, 1981](#); [Davis *et al.*, 1985](#); [Carlberg and Couchman, 1989](#); [Zurek *et al.*, 1994](#)). In the early '90s, the comparison between the large-scale correlation of galaxies simulated with the observations available already suggested a tension if no cosmological constant was taken into account ([Maddox *et al.*, 1990](#); [Efstathiou *et al.*, 1990](#); [Suginohara and Suto, 1991](#)), well before the cosmic acceleration had been observed and confirmed by the Supernovae Ia projects ([Riess *et al.*, 1998](#); [Perlmutter *et al.*, 1999](#)). The internal structure of haloes and its substructures were the object of investigation in the next decade ([Warren *et al.*, 1992](#); [Gelb and Bertschinger, 1994](#); [Navarro *et al.*, 1996, 1997](#); [Klypin *et al.*, 1999](#); [Moore *et al.*, 1999](#)) and the establishment of Λ CDM was then confirmed with large-scale and high-resolution simulations ([Jenkins *et al.*, 1998](#); [Governato *et al.*, 1999](#); [Colberg *et al.*, 2000](#); [Bode *et al.*, 2001a](#); [Wambsganss *et al.*, 2004](#); [Springel *et al.*, 2005, 2008](#)).

The overview we presented on role of N-body simulations in the establishment of the Λ CDM model is far from being an exhaustive review, but it well represents

how numerical simulations have accompanied – and in some cases even anticipated – the outstanding theoretical progress that the available technologies have been able to stimulate with new observations and computational resources.

2.1 Computing the gravitational potential

The numerical simulations divide into two main categories with respect to the essential elements that are used to represent the system: the *Lagrangian* or *N-body* simulations are particle-based, with each particle having a position \vec{x} and a velocity \vec{v} , while the *Eulerian* grid-based codes are based on cells, that possess a density ρ and a set of boundary fluxes $\{\phi\}$. These two approaches have somewhat complementary strengths and weaknesses, as we will detail below, and it is not uncommon for them to coexist in different forms within the same simulation, connected by particle–cell mapping routines.

As a matter of fact, the particle-based approach is more suitable for fine-structure systems driven by local physical mechanisms as it focuses the computational resources automatically in the most needed regions and adjusts the resolution accordingly – i.e. the densest regions are the most crowded with particles – while having problems in shocks and high entropy situations. On the contrary, the Eulerian cell-based approach is best performing in the circumstances where N-body codes do not excel since it does not suffer from divergence problems – e.g. arising in $\propto 1/r$ potentials when two particles overlap –, at the cost of having an *a priori* fixed resolution set by the initial number of essential elements*. Since this work is related to the implementation and application of physical modules within the N-body code P-GADGET3, a non-public extension of the GADGET2 code (Springel, 2005), we will mainly focus on the properties of particle-based codes.

N-body simulations follow the evolution of a gravitational system composed of N particles, whose positions and velocities are evolved according to the gravitational force originated by the density field represented by the particle configuration. While CDM is collisionless, thus not requiring any additional physical imple-

*In fact, adaptive schemes for grid refinement can be devised, but these inevitably increase the number of essential elements – i.e. cells –, with consequential memory and computational costs.

mentation, the baryonic matter needs to be treated with hydrodynamical equations that have to be properly taken into account. Astrophysical processes as gas cooling, star formation and feedback mechanisms can be implemented in the effort of simulating a system which is the most realistic and consequently relevant for scientific study. However, we have to consider that the development of rich and multifaceted numerical simulations has to be adequately related to the time and memory computational resources available, in order to be feasible and useful.

In N-body simulations, it is assumed that the underlying matter fluid evolution can be analogously described with a set of discrete bodies – i.e. the *simulation particles*, each with its position \vec{x} and velocity \vec{u} – that collectively represent a coarse-grained gauge for the full continuous density distribution. In the collisionless case, the dynamics of particle i is governed by the linearized Euler equation of Eq. 1.49

$$\dot{\vec{u}}_i + 2H\vec{u}_i = -\frac{\vec{\nabla}\Phi}{a^2} \quad (2.1)$$

that can be simplified applying the coordinates transformation

$$\vec{p}_i = a^2 \vec{u}_i \quad (2.2)$$

that leads to

$$\dot{\vec{p}}_i = \frac{\vec{F}_i}{m_i} \quad (2.3)$$

where we defined \vec{F}_i is the total force experienced by particle i . In terms of algorithm design, the recasting of comoving velocity \vec{u} into a new velocity \vec{p} – which has no direct physical meaning – is rather useful since the friction term $2H\vec{u}_i$ is now implicit.

The simplest approach to evaluate the gravitational force applied to particles – i.e. the only contribution to the total force for collisionless fluids – is called *Particle-Particle*, where \vec{F}_i is computed by the direct summation of each particle pair contribution

$$\vec{F}_i = -Gm_i \sum_{j \neq i}^N \frac{m_j}{|\vec{x}_i - \vec{x}_j|^2 + \epsilon^2} \frac{\vec{x}_i - \vec{x}_j}{|\vec{x}_i - \vec{x}_j|} \quad (2.4)$$

where the sum runs over $N - 1$ particles and ε is the *gravitational softening length* that prevents divergence and can be physically interpreted as the incompressible dimension of the particles. This method is accurate and, not less importantly, easy to implement; however, the numerical operations required scale as the square of the particle number $\sim N(N - 1)/2 \sim N^2$ that, compared to the resolution scaling $\sim N^{-1}$, rapidly overturn the algorithm performance when the number of particles becomes too large.

In order to reduce the computational cost of the Particle-Particle direct summation, we can group particles in a smart coarse-grained fashion and only then compute the gravitational force. One possibility is to build a grid and use it as to approximate the underlying particle distribution: this is called *Particle-Mesh* approach. First, one needs to estimate the density field on the mesh-nodes through particle interpolation, then to calculate the gravitational potential solving the Poisson equation in the Fourier space, and finally obtain the gravitational force field with Fourier anti-transformation. There are several schemes to map the particle masses to the grid cells, some examples are presented and discussed in Section 2.3 focused on the construction of density fields.

Using the Particle-Mesh strategy, the number of operations reduce to $\sim M \log M$ with a M point mesh. Nevertheless, the decreasing computational cost is convenient only if we are not interested in the close encounters between particles or if we analyse weakly correlated systems, cases in which the mesh-based approach is not optimal.

The natural evolution of the previous two algorithms presented, given their complementary properties, is the combination of the two schemes in order to exploit each one at its best: the so-called *Particle-Particle/Particle-Mesh* or *P3M* method consists in a Particle-Particle summation in a spherical domain enclosing the particle of interest and a Particle-Mesh in the outer regions. The choice of the characteristic radius of the connection has to be chosen wisely to have a good balance between the computational cost and the accuracy at small scales.

Another widely used strategy is the hierarchical multipole expansion, commonly

called *Tree* algorithm. It represents a variant of the Particle-Particle approach and can be combined with Particle-Mesh in a *TreePM* setting. It is based on the flexible construction and exploration of a spatial tree that, starting from the coarsest level – i.e. the whole simulation domain –, is recursively subdivided into 2^{dim} sub-domains until all cells are either empty or containing just one particle. In this way, each non-empty node of the tree represents either a single particle in the most refined level, a group of particles in the intermediate ones or the totality of particles in the root level. For each particle, the force is then calculated through direct summation on the *macro* particle represented by the tree nodes and the depth reached in the tree exploration can be tuned requiring a given accuracy in the force evaluation. It is clear that the full exploration of the tree to the most refined level coincides with the Particle-Particle approach with $\sim N^2$ operations, while the use of the single root level corresponds to a pure *mean-field* approach scaling as $\sim N$. Tree codes do not waste time to process void regions, they are not confined to a fixed grid and the number of operations they require – in a balanced set-up – scales as $\sim N \log N$. However, the computational cost of tree construction and a considerable amount of additional memory usage to store the tree variables are required; therefore, an efficient update scheme for the tree has to be devised.

The algorithms presented have been developed during the years to fully exploit the computational resources available at the time. As we can see in Fig. 2.1, several schemes characterised by growing complexity, a hybrid design and parallelised computational approach have been used in the literature.

2.2 Evolving in time: Time-integration schemes

Along with the method used to compute the gravitational potential, another aspect that identifies a numerical simulation is the time integration scheme adopted to discretise time and update the relevant quantities of the system, namely positions and velocities in the case of a N-body simulation. It exists a long list of time integration schemes, from first-order – as e.g. the Forward Euler and Backward Euler – to second-order or higher order – as e.g. Velocity Verlet, Leapfrog and Runge-Kutta – methods. However, a detailed review of such schemes is beyond

the scope of this thesis, and we will focus on the method used in the P-GADGET3 code: the Leapfrog scheme, as described in [Quinn *et al.* \(1997\)](#) and [Springel \(2005\)](#).

The Leapfrog integration is a second order method consisting in two different phases devoted to update the variables \vec{x}_i and \vec{p}_i and expressed by the operators D and K . The former is called *Drift*

$$D(\Delta t) : \begin{cases} \vec{x}_i \rightarrow \vec{x}_i + \vec{p}_i \int_t^{t+\Delta t} \frac{dt'}{a^2} \\ \vec{p}_i \rightarrow \vec{p}_i \end{cases} \quad (2.5)$$

and is related to the position update while the latter, called *Kick*,

$$K(\Delta t) : \begin{cases} \vec{x}_i \rightarrow \vec{x}_i \\ \vec{p}_i \rightarrow \vec{p}_i + \frac{\vec{F}_i}{m_i} \int_t^{t+\Delta t} \frac{dt'}{a} \end{cases} \quad (2.6)$$

corresponds to the velocity update. The two phases are combined into the complete *Kick-Drift-Kick* – or equivalently in the *Drift-Kick-Drift* – time propagator

$$\begin{pmatrix} \vec{x}_i \\ \vec{p}_i \end{pmatrix} (t + \Delta t) = K\left(\frac{\Delta t}{2}\right) D(\Delta t) K\left(\frac{\Delta t}{2}\right) \begin{pmatrix} \vec{x}_i \\ \vec{p}_i \end{pmatrix} (t) \quad (2.7)$$

which results in a symplectic and time-reversible algorithm ([Saha and Tremaine, 1992](#)). These properties are particularly helpful to resolve astrophysical and cosmological systems – as e.g. the Kepler problem of orbitating objects ([Kinoshita *et al.*, 1991](#)) –, in which long-term stability is crucially dependent on energy conservation (for a comparison between different time integration schemes, see [Springel, 2005](#)).

The peculiar symmetric form of the Leapfrog update scheme, that involve half step updates, can be explained with the following argument. On a very general

level, the transformation S that, for a finite timestep Δt , evolves

$$\vec{x}_i(t) \rightarrow \vec{x}_i(t + \Delta t) \quad (2.8)$$

$$\vec{p}_i(t) \rightarrow \vec{p}_i(t + \Delta t) \quad (2.9)$$

can be expressed in exponential terms

$$\vec{q}(t + \Delta t) = e^{\Delta t S} \vec{q}(t) \quad (2.10)$$

where $\vec{q} = \{\vec{x}, \vec{p}\}$ are the generalized coordinates of the system. If we split the total transformation in the two sequential steps \mathcal{A} and \mathcal{B}

$$\vec{q}(t + \Delta t) = e^{\Delta t \mathcal{A}} e^{\Delta t \mathcal{B}} \vec{q}(t) \quad (2.11)$$

the two transformations are related by the Baker–Campbell–Hausdorff formula

$$\Delta t S = \ln \left(e^{\Delta t \mathcal{A}} e^{\Delta t \mathcal{B}} \right) = \Delta t (\mathcal{A} + \mathcal{B}) + \frac{\Delta t^2}{2} [\mathcal{A}, \mathcal{B}] + \frac{\Delta t^3}{12} ([\mathcal{A}, [\mathcal{A}, \mathcal{B}]] - [\mathcal{B}, [\mathcal{B}, \mathcal{A}]]) + O(\Delta t^4) \quad (2.12)$$

where the operator $[\mathcal{A}, \mathcal{B}] = \mathcal{A}\mathcal{B} - \mathcal{B}\mathcal{A}$ is the commutator *Lie bracket*, which evidently satisfies the anti-symmetric property $[\mathcal{A}, \mathcal{B}] + [\mathcal{B}, \mathcal{A}] = 0$. With a peculiar symmetric combination it is possible to cancel the Δt^2 term

$$\begin{aligned} \Delta t S &= \frac{1}{2} \ln \left(e^{\Delta t \mathcal{A}} e^{\Delta t \mathcal{B}} \right) + \frac{1}{2} \ln \left(e^{\Delta t \mathcal{B}} e^{\Delta t \mathcal{A}} \right) = \\ &= \ln \left(e^{\frac{\Delta t}{2} \mathcal{A}} e^{\Delta t \mathcal{B}} e^{\frac{\Delta t}{2} \mathcal{A}} \right) = \Delta t (\mathcal{A} + \mathcal{B}) + O(\Delta t^3) \end{aligned} \quad (2.13)$$

so that we can rewrite the total transformation of Eq. 2.10 as

$$\vec{q}(t + \Delta t) = \left[e^{\Delta t \mathcal{A}} e^{\Delta t \mathcal{B}} + O(\Delta t^2) \right] \vec{q}(t) = \left[e^{\frac{\Delta t}{2} \mathcal{A}} e^{\Delta t \mathcal{B}} e^{\frac{\Delta t}{2} \mathcal{A}} + O(\Delta t^3) \right] \vec{q}(t) \quad (2.14)$$

which reduces the error on the time integration with respect to the direct application of \mathcal{A} and \mathcal{B} . This is the argument backing the symmetric nature of the Leapfrog method: since it is needed to update positions and velocities separately, the updates

are not applied sequentially but symmetrically arranged as above to reduce the final error (a more rigorous derivation of the algorithm in the astrophysical N-body context can be found in [Yoshida, 1993](#); [Duncan *et al.*, 1998](#), and references therein).

[Yoshida \(1990\)](#) paved the way towards the optimization of the Leapfrog scheme to higher order by noticing that the fourth order scheme previously found by [Forest \(1989\)](#) – that symmetrically cancelled the Δt^3 and Δt^4 terms – was a composition of the fundamental operator

$$S_2(\Delta t) \equiv e^{\frac{\Delta t}{2} \mathcal{A}} e^{\Delta t \mathcal{B}} e^{\frac{\Delta t}{2} \mathcal{A}} \quad (2.15)$$

and it could be expressed as

$$S_4(\Delta t) = S_2(w_0 \Delta t) S_2(w_1 \Delta t) S_2(w_0 \Delta t) \quad (2.16)$$

with weights $w_0 = 1/(2 - 2^{1/3})$ and $w_1 = -2^{1/3} w_0$. [Suzuki \(1992\)](#) later generalized this result to a n -th arbitrary order, where the force has to be computed $n - 1$ times in-between steps.

The typical large dynamic range of time-scales of cosmological systems allows us to further improve performances in a similar way to what it is done for the evaluation of the gravitational potential. In fact, it is evident that in low-density regions, like the intergalactic medium, the time-step required to detail particle dynamics is much larger than the one needed to characterise the high-density regions with the same accuracy, thus making the “*one size fits all*” approach a suboptimal choice for the time-step Δt ([Quinn *et al.*, 1997](#)). Therefore, we can devise an integration scheme that supports individual time-steps, in order not to waste the computational resources that using uniquely the smallest time-step would imply. The evolution of the system with individual particle time-steps does not retain the symplectic nature of the Leapfrog time integration scheme; however, due to the collisionless nature of the fluid, in the limit of single particle-particle interaction being much smaller than the total force given by the collective potential, the two-body collisions are negligible and the energy conservation is only negligibly affected ([Springel, 2005](#)).

The choice of the individual time-step can be computed as function of the softening length ε and the particle acceleration \ddot{u}_i

$$\Delta t_i = \min \left\{ \Delta t_{max}, \sqrt{\frac{2\varepsilon}{|\ddot{u}_i|}} \right\} \quad (2.17)$$

and binned in a power of two hierarchy, where all time-steps are a power of two subdivision of a global time-step Δt_{max} (see [Power *et al.*, 2003](#), for a detailed convergence study of different time-stepping strategies).

2.3 From particle to fields: Smoothed Particle Hydrodynamics

In N-body simulations, whether it is to calculate the gravitational potential or to derive hydrodynamical quantities – as e.g. the gas pressure –, it is necessary to map the particle ensemble into a continuous density distribution. In fact, fluid particles are a discrete representation of an underlying physical density distribution ρ^{phys} that is required to solve the dynamical equations (for an extensive review on the topic see e.g. [Hockney and Eastwood, 1981](#)). The problem is then to relate ρ^{phys} with the numerical density distribution ρ^{num} of particles

$$\rho^{num}(\vec{x}) = \frac{1}{V} \sum_i^N m_i \delta(\vec{x} - \vec{x}_i) \xrightarrow{?} \rho^{phys} \quad (2.18)$$

given by the sum of δ Dirac delta functions.

The strategies that are used to compute the density have different forms according to the Eulerian or Lagrangian nature of the problem. In the former, the density is represented with a single value for each cell, in which the volume is given by construction but the corresponding mass has to be estimated.

The interpolation scheme to assign the particle masses to the grid cells can have different forms ([Harlow, 1988](#)), and the most used ones are:

- *Nearest Grid Point* (NGP):
each particle is assigned to nearest cell, whose mass is then the bare sum of the nearest particle masses;

- *Cloud In Cell* (CIC):
the mass of each particle is divided between its 2^{dim} nearest cells, weighted with respect to the position of the particle within the cell, where dim is the system dimensionality;
- *Triangular Shape Cloud* (TSC):
similar to the CIC scheme but with higher order interpolation, the cells involved are 3^{dim} .

The density reconstruction on a lattice has the appealing property of being evaluated at evenly distributed points in the simulation box – i.e. the grid centres – and the volume associated with each value is given by definition – i.e. the grid volume –. Furthermore, density derivatives are easily obtained with finite-difference methods. However, once the observables of interest are calculated on the grid, the interpolation scheme must be applied backwards from cells to particles compromising the accuracy of the physical representation of dynamics that are near the resolution scale. Moreover, density calculated in cells admits a zero-value – i.e. if there are no particle near the cell –, propagating numerical errors in low-dense regions whenever the computation involves density factors with negative exponent.

In the Lagrangian approach, instead, density is evaluated at the particle positions thus requiring a systematic method to assign a volume of integration to each one. The most used scheme in astrophysics is called Smoothed Particle Hydrodynamics (SPH), initially developed by [Gingold and Monaghan \(1977\)](#) and [\(Lucy, 1977\)](#) and later improved during the years by many contributors, as thoroughly reported in the review by [Monaghan \(1992\)](#) on the topic, followed by a second one twenty years later ([Monaghan, 2012](#)).

The general SPH approach relies on the concept that the density field can be approximated at particle i position with the weighted sum of the mass m of neighbouring particles $NN(i)$

$$\rho_i = \sum_{j \in NN(i)} m_j W_{ij}, \quad (2.19)$$

where the mass is convolved with a kernel function W_{ij} of choice, characterized by a particle-specific smoothing length h_i , and whose extent is fixed imposing

$$\frac{4}{3}\pi h_i^3 \rho_i = \sum_{j \in \text{NN}(i)} m_j \quad (2.20)$$

so that only a given number of neighbours – or a given mass, equivalently – is enclosed within it.

Once the density field is reconstructed, every observable is locally computed through weighted sums as

$$O_i = \sum_{j \in \text{NN}(i)} m_j \frac{O_j}{\rho_j} W_{ij} \quad (2.21)$$

and its derivatives are iteratively obtained with

$$\vec{\nabla} O_i = \sum_{j \in \text{NN}(i)} m_j \frac{O_j}{\rho_j} \vec{\nabla} W_{ij} \quad (2.22)$$

where the derivative is applied on the window function.

Within the SPH framework, the density calculated at particle positions cannot be zero and the varying smoothing length allows for a dynamical adaptivity of resolution, but the algorithm tends to over-smooth sharp density discontinuities and accumulate numerical error for higher order derivatives. Nevertheless, the exact scheme of the SPH algorithm is not fixed, since each observable can be expressed in many analytically equivalent forms that, however, translate into different operative summations. The important consequence of such flexibility is that different but analytically equivalent expressions will map into operative sums that carry different numerical errors. We will discuss in the next chapters which strategy is the most suitable for our problem among the several ones that have been employed in the literature to reduce the residual numerical errors (see e.g. [Brookshaw, 1985](#); [Cleary and Monaghan, 1999](#); [Colin *et al.*, 2006](#)).

2.4 P-GADGET3

In this thesis, we will discuss the implementation of physical models regarding the dark sector in the P-GADGET3 code. Therefore, in this Section, we will review the basic properties of P-GADGET3 in view of the different numerical approaches described in this Chapter (as we said earlier, P-GADGET3 is a non-public extension of the GADGET2 code, see [Springel, 2005](#), for the comprehensive code characterisation).

P-GADGET3 is an N-body TreePM code written in C programming language ([Kernighan and Ritchie, 1978](#)), in which the gravitational potential is solved with a combination of the Hierarchical 3D Tree and the Particle-Mesh methods for the short- and long-range evaluations, respectively. The time integration scheme is a Kick-Drift-Kick second-order Leapfrog, where the individual time-steps depend on the particle acceleration as in Eq. 2.17.

In order to have fluids governed by different dynamics simultaneously, particles are divided into *types* that correspond to C classes retaining all the relevant information. For example, particles of type 0 and type 1 are usually considered as baryonic and dark matter particles, respectively.

While for dark matter particles it needs to compute only the gravitational potential and the relative gravitational acceleration, due their collision-less dynamics, for baryonic particles – often referred simply as *gas* particles for historical reasons – a complete description of the thermodynamic state of the fluid ([Springel and Hernquist, 2002](#)) is required. To this end, an SPH routine is devoted to extrapolate the underlying density of the gas distribution used to estimate the pressure gradient that enters the Euler Equation of Eq. 1.49.

The evaluation of the density values is performed through consecutive iterations on each particle: starting with an initial guess for the smoothing length h_i , a fixed *desideratum* number of neighbours \mathbb{N} and a tolerance ε , the following scheme is repeated until the condition at point (*iv*) is satisfied for all particles

- i. set the temporary variables $h_i^- = h_i^+ = 0$

- ii. define the nearest neighbours ensemble $\text{NN}(i) = \{j : |\vec{r}_{ij}| \leq h_i\}$
- iii. using Eq. 4.12, calculate the quantity ρ/m which is used to represent the weighted number of neighbours

$$\bar{N}_i = \frac{4}{3} \pi h_i^3 \sum_{j \in \text{NN}(i)} W_{ij} \quad (2.23)$$

- iv. if $|\mathbb{N} - \bar{N}_i| < \varepsilon$ stop and keep h_i as the smoothing length for particle i
- v. update the values of h_i^- and h_i^+ as

$$\begin{cases} h_i^- = \max(h_i^-, h_i) & \text{if } \bar{N}_i \leq \mathbb{N} \\ h_i^+ = \min(h_i^+, h_i) & \text{if } \bar{N}_i \geq \mathbb{N} \end{cases} \quad (2.24)$$

- vi. calculate

$$\begin{cases} h_i = \sqrt[3]{2} h_i^- & \text{if } h_i^+ = 0 \\ h_i = h_i^+ / \sqrt[3]{2} & \text{if } h_i^- = 0 \\ h_i = \sqrt[3]{\frac{(h_i^-)^3 + (h_i^+)^3}{2}} & \text{otherwise} \end{cases} \quad (2.25)$$

which will be used as the new smoothing length guess, starting again from point (ii).

Once the smoothing length for each particle is defined, the corresponding density is computed through the standard SPH summation on the neighbouring particles.

Based on gas particle densities, the pressure contribution to the acceleration of particle i is

$$\dot{\vec{u}}_i|_P = - \sum_{j \in \text{NN}(i)} m_j \left[\frac{P_j}{\rho_j^2} \vec{\nabla} W_{ij} + \frac{P_i}{\rho_i^2} \vec{\nabla} W_{ij} \right] \quad (2.26)$$

as obtained applying the SPH derivative formula Eq. 2.22 to the pressure gradient

$$-\frac{\vec{\nabla}P}{\rho} = -\vec{\nabla}\left(\frac{P}{\rho}\right) - \frac{P}{\rho^2}\vec{\nabla}\rho \quad (2.27)$$

conveniently split in two terms. Provided the absence of shocks or external sources of heat, the equations above are entropy conserving – i.e. describe a reversible process –. However, flows of ideal gases are characterized by discontinuities, where entropy is generated by (unresolved) micro-physics. To take into account the thermodynamic production of entropy, the evolution of pressure and density is mediated by a function A defined as

$$A = P/\rho^\gamma \quad (2.28)$$

where γ is the gas *adiabatic index*. The function A is called *entropic function*, since $A = A(S)$ is only a function of entropy in the case of an ideal gas.

The loss of kinetic energy in favour of temperature is introduced in the dynamics of gas particles as an *artificial viscosity* (in the version of [Monaghan, 1997](#)), that enters the Euler equation as

$$\dot{\vec{u}}_i|_{visc} = - \sum_{j \in \text{NN}(i)} m_j \Pi_{ij} \vec{\nabla} W_{ij} \quad (2.29)$$

where the positive-defined function Π

$$\Pi_{ij} = \frac{\alpha}{\rho_i + \rho_j} \frac{\vec{u}_{ij} \cdot \vec{r}_{ij}}{|r_{ij}|} \left(\frac{c_{s,i} + c_{s,j}}{2} - 3 \frac{\vec{u}_{ij} \cdot \vec{r}_{ij}}{|r_{ij}|} \right) \Theta(-\vec{u}_{ij} \cdot \vec{r}_{ij}) \quad (2.30)$$

depends on the velocity of the particles and the sound speed c_s of the two, multiplied by a free parameter α and a Theta function Θ that applies viscosity only to converging particles (see e.g. [Monaghan and Gingold, 1983](#); [Balsara, 1995](#), for different forms of the artificial viscosities). The viscosity generates a variation in the

entropic function

$$\frac{dA_i}{dt} = \frac{\gamma-1}{2\rho_i^{\gamma-1}} \sum_{j \in \text{NN}(i)} m_j \Pi_{ij} \vec{u}_i \cdot \vec{\nabla} W_{ij} \quad (2.31)$$

that accounts for the heating of the gas and regulates the equation of state $P_i = A_i \rho_i^\gamma$ (Springel and Hernquist, 2002). Due to the introduction of the artificial viscosity, the sound speed is taken into account to estimate the individual time-step chosen for the gas particles. In particular, the time-step used corresponds to the minimum between the usual acceleration dependent one and

$$\Delta t_i^{\text{gas}} = C h_i \left[\max_{j \in \text{NN}(i)} \left(c_{s,i} + c_{s,j} - 3 \frac{\vec{u}_{ij} \cdot \vec{r}_{ij}}{|r_{ij}|} \right) \right]^{-1} \quad (2.32)$$

where C is the Courant number of choice (Courant *et al.*, 1928, see).

Finally, P-GADGET3 is a massively parallel simulation code, containing instructions for communication encoded with the standardized Message Passing Interface (MPI). Moreover, it exploits the parallelised routines of the open-source libraries *GNU Scientific Library* (GSL) (Galassi, 2018), and *Fastest Fourier Transform in the West* (FFTW) (Frigo and Johnson, 2005), resulting in a very high degree of portability. The total memory and computational load are distributed among processors using a space-filling fractal, the *Peano–Hilbert curve*, to map 3D space on to a 1D curve (as first suggested by Warren and Salmon, 1993, 1995). The latter is then divided into intervals that define the individual domains, identifying the particles and tree leaves to be committed to every processor (see Springel, 2005, for the details on space decomposition). The parallelisation algorithms of the code are flexible enough to allow its use on an arbitrary number of processors. As a result, P-GADGET3 can be run on a large variety of machines, ranging from a laptop to High-Performance Computing (HPC) clusters.

2.5 Beyond Cold Dark Matter

As we said in the previous Sections, according to the currently accepted standard cosmological scenario – known as the Λ CDM model – about 80% of the matter content of the present universe is in the form of cold and collisionless dark matter particles, whose contribution to the gravitational instability of density perturbations drives the formation of present cosmic structures stemmed from the tiny primordial fluctuations observed in the CMB (Planck Collaboration, 2018).

The success of the Λ CDM model has been significantly supported over the past decades by the development and continuous improvement of numerical techniques, that allowed us to simulate the evolution of cosmic structures in an expanding universe from the well understood linear domain, constrained by CMB observations, down to the highly non-linear regime that characterises the present-day density field at small scales. In this respect, large and sophisticated cosmological N-body simulations – as well as their hydrodynamical extensions accounting for the complex astrophysical processes, related to the subdominant baryonic matter component – have undeniably become an essential tool in contemporary astrophysics and cosmology.

Whether dark matter consists indeed of a yet undetected fundamental particle or it represents an indirect effect of some modification of Einstein’s General Relativity theory of gravity is still widely debated. Nevertheless, it has been possible to exclude some of the proposed dark matter effective models, such as e.g. the Modified Newtonian Dynamics and its variants (MOND see e.g. Milgrom, 1983; Sanders and McGaugh, 2002; Bekenstein, 2004), recently ruled out (Chesler and Loeb, 2017) by the implications of the gravitational wave event GW170817 (Abbott *et al.*, 2017). The lack of detection of dark matter particles in the GeV mass range through neither of indirect astronomical observations (see e.g. Albert *et al.*, 2017), direct laboratory detections (see e.g. Danninger, 2017), nor artificial production in high-energy collisions experiments (see e.g. Buonaura, 2018) has been undermining the appeal of the most massive dark matter particle candidates, as e.g. the Weakly Interactive Massive Particles (WIMPs), and it is presently shifting the scientific community efforts in the hunt of direct observations from such high mass

ranges towards lower ones (see e.g. [Bertone et al., 2005](#)).

A good starting point where to focus research and to clarify such long-standing uncertainties would be the apparent failures of the Λ CDM model at scales $\lesssim 10$ Kpc – as given e.g. by the cusp-core problem ([Oh et al., 2011](#)), the missing satellite problem ([Klypin et al., 1999](#)), the too-big-to-fail problem ([Boylan-Kolchin et al., 2012](#)), all arising as an apparent inconsistency between simulations and observations, the latter being more in line with less pronounced density fluctuations at those scales than predicted by the former. However, the nature of such apparent failures has been subject of debate in the astrophysics community. It is still unclear, in fact, whether they should be ascribed to an imperfect baryonic physics implementation in numerical simulations (see e.g. [Macció et al., 2012](#); [Brooks et al., 2013](#)), to an intrinsic diversity of properties related to the formation history and local environment of each individual dark matter halo ([Oman et al., 2015](#)), to the fundamental nature of the dark matter particle (see e.g. [Spergel and Steinhardt, 2000](#); [Rocha et al., 2013](#); [Kaplinghat et al., 2000](#); [Medvedev, 2014](#)) or even to a combination of all these possible causes.

With the next generation of cosmological surveys (as e.g. Euclid, LSST, SKA, see [Laureijs et al., 2011](#); [Ivezic et al., 2008](#); [Blake et al., 2004](#), respectively) starting to take data in the near future, holding the promise to pinpoint with unprecedented precision the parameters involved in the Λ CDM model and to detect even extremely feeble signals of deviations from the standard cosmology, the urge for more accurate predictions on the expected signatures of alternative scenarios is now a high priority for the community. In this respect, developing numerical tools for cosmological simulations of alternative dark matter candidates represents a necessary step to provide such predictions.

Part II

Fuzzy Dark Matter

3

Ultralight bosonic dark matter

One intriguing solution to the CDM problems might involve an extremely light non-thermal boson acting as dark matter, whose de-Broglie wavelength arising from its fundamental quantum nature would be relevant at cosmological scales (see e.g. [Marsh and Ferreira, 2010](#); [Hui *et al.*, 2017](#)). The lightness and quantum behaviour of such bosonic dark matter particles could simultaneously explain its elusiveness and alleviate tensions at small scales (see e.g. [Marsh and Pop, 2015](#)). This type of dark matter has been generically termed *Fuzzy Dark Matter* (FDM hereafter, see [Hu *et al.*, 2000](#)) and several particles that fit in this description have been proposed in the literature, the most popular class being Ultra Light Axions (ULAs, [Marsh, 2016a](#)).

The typical wave-like quantum effects effectively add to the standard CDM dynamics a repulsive behaviour while creating oscillating interference patterns. This requires a description of dark matter dynamics in terms of the Schrödinger equation, in order to take into account quantum corrections, and can be mapped in a

fluid-like description where a *quantum potential* (QP) enters the classical Euler equation (Hu *et al.*, 2000).

Such interaction actively smoothes matter overdensities below a redshift dependent scale that decreases with the cosmic evolution, as confirmed by FDM linear simulations (see e.g. Marsh and Ferreira, 2010; Hlozek *et al.*, 2015), thus potentially easing some of the previously mentioned small-scale inconsistencies of the CDM model.

The lack of density perturbations at small scales induced by the QP is represented, in Fourier space, by a sharp suppression of the matter power spectrum, that persists at any given scale until the action range of the QP shrinks below such scale and cannot balance any longer the effect of the gravitational potential (see e.g. the reviews on the topic Marsh, 2016a; Hui *et al.*, 2017).

As a matter of fact, while linear theory predicts that perturbations at scales smaller than the cutoff scale never catch up with those at larger scales – untouched by FDM peculiar dynamics –, non-linear cosmological simulations have shown that gravity is indeed able to restore intermediate scales to the unsuppressed level, in a sort of *healing* process (Marsh, 2016b; Nori and Baldi, 2018).

Given that gravity, as mentioned above, can restore the suppressed power at intermediate scales in the non-linear regime, major observables related to the LSS at such scales may appear similar in both FDM and CDM picture cosmologies at sufficiently low redshifts. For this reason, Lyman- α forest observations could play a crucial role in distinguishing such radically different models of dark matter, being one of the most far-reaching direct astrophysical probes in terms of redshift of the LSS observables, sampling the redshift range $z \sim 2 - 5$ (see e.g. Iršič *et al.*, 2017c, for Lyman- α forest analysis in N-body simulations, with neglected QP dynamical effects).

In this chapter, we present a modification of the cosmological N-Body and hydrodynamical code P-GADGET3– a non-public extension of the public GADGET2 code (Springel, 2005) – to simulate the non-linear evolution of FDM scenarios featuring light boson fields as dark matter particles.

3.1 Theory and perturbation evolution

Let $\hat{\phi}$ be a bosonic field evolving accordingly to the Gross-Pitaevskii-Poisson equation (Gross, 1961; Pitaevskii, 1961)

$$i\hbar \partial_t \hat{\phi} = -\frac{\hbar^2}{m_\chi^2} \nabla^2 \hat{\phi} + m_\chi \Phi \hat{\phi} + \lambda (\hat{\phi}^\dagger \hat{\phi}) \hat{\phi} \quad (3.1)$$

where Φ is the Newtonian gravitational potential, λ and m_χ represent the self-interaction coupling constant and typical mass of the field, respectively.

In order to describe the dynamics of such field in terms of fluid equations, we use the Madelung form (Madelung, 1927)

$$\hat{\phi} = \sqrt{\frac{\rho}{m_\chi}} e^{i\frac{\theta}{\hbar}} \quad (3.2)$$

where ρ is the fluid density and θ is related to the fluid velocity as $\vec{u} = \vec{\nabla}\theta/m_\chi$. Extending this approach to the case of an expanding universe – in a comoving frame with a and $H = \dot{a}/a$ being the usual cosmological scale factor and Hubble function, respectively – we recover the well known Madelung equations, consisting in the continuity equation

$$\dot{\rho} + 3H\rho + \vec{\nabla} \cdot (\rho\vec{u}) = 0 \quad (3.3)$$

and a modified Euler equation

$$\dot{\vec{u}} + 2H\vec{u} + (\vec{u} \cdot \vec{\nabla}) \vec{u} = -\frac{\vec{\nabla}\Phi}{a^2} - \frac{\vec{\nabla}P}{a^2\rho} + \frac{\vec{\nabla}Q}{a^4} \quad (3.4)$$

where three distinct sources of particle acceleration appear: the gravitational potential Φ , a pressure-like term P accounting for the self-interaction of the field, and an additional potential Q .

The gravitational potential Φ satisfies the usual Poisson equation

$$\nabla^2 \Phi = 4\pi G a^2 \rho_b \delta \quad (3.5)$$

where $\delta = (\rho - \rho_b)/\rho_b$ is the density contrast with respect to the background field

density ρ_b (Peebles, 1980).

The self-interaction term P can be regarded as a pressure and, in principle, can be generalised with a parametric equation of state $P = P(\rho)$ to take into account self-interactions of different forms. In the case of quartic self-interaction, as in Eq. 3.1, it reads $P = \lambda \rho^2 / 2m_\chi$.

The potential Q has the form of

$$Q = \frac{\hbar^2}{2m_\chi^2} \frac{\nabla^2 \sqrt{\rho}}{\sqrt{\rho}} = \frac{\hbar^2}{2m_\chi^2} \left(\frac{\nabla^2 \rho}{2\rho} - \frac{|\vec{\nabla} \rho|^2}{4\rho^2} \right) \quad (3.6)$$

and we acknowledge its use in the literature since the 50s as *Quantum Potential* (QP) (Bohm, 1952). In recent applications in cosmology, it has been expressed sometimes as a pressure tensor

$$\vec{\nabla} Q = \frac{1}{\rho} \vec{\nabla} P_Q = \frac{\hbar^2}{2m_\chi^2} \frac{1}{\rho} \vec{\nabla} \cdot \left(\frac{\rho}{4} \vec{\nabla} \otimes \vec{\nabla} \ln \rho \right) \quad (3.7)$$

thus addressed as *Quantum Pressure* (see e.g. Mocz and Succi, 2015). In this work we prefer the former *potential* terminology, given its uninvolvement with classical thermal interactions. We find necessary, indeed, to stress that this potential has neither links with temperature nor any classical thermodynamics origin. Its mathematical form and physical behaviour are related to a self-organizing process and are connected to basic principles of quantum information and occupation of states (Boehmer and Harko, 2007).

The set of Eq. 3.3-3.5 has a stable solution for $\delta = \Phi = |\vec{v}| = 0$ which can be linearised assuming small perturbations in order to end up with a new set of equations. The resulting equations can be combined in the density contrast time evolution reading

$$\ddot{\delta} + 2H\dot{\delta} + \left(\frac{\hbar^2 k^4}{4m_\chi^2 a^4} + \frac{c_s^2 k^2}{a^2} - \frac{4\pi G \rho_b}{a^3} \right) \delta = 0 \quad (3.8)$$

where $\delta(\vec{x}, t)$ has been decomposed in Fourier modes $\delta_k e^{i\vec{k} \cdot \vec{x}}$ and $c_s^2 = \partial_\rho P(\rho)|_{\rho_b}$ is the sound speed of the fluid (Chavanis, 2012).

Our implementation (see below) is able to simulate models with any given self-interaction encoded in $P(\rho)$ as a parametrised input. However, in this work we restrict our focus only on the effects of the QP and leave the exploration of self-interacting models for future work. We therefore consider $\lambda = 0$, thus $P = c_s = 0$, hereafter.

A perturbed stable solution of Eq. 3.8, is given by a density contrast with mode

$$k_Q(a) = \left(\frac{16\pi G \rho_b a^3 m_\chi^2}{\hbar^2} \right)^{1/4} a^{1/4} \quad (3.9)$$

and corresponding wavelength $\lambda_Q = 2\pi/k_Q$, representing a quantum version of the Jeans wavenumber and Jean length, respectively.

Given the cosmological scale factors $a(t)$ at each time t , the wavelengths λ_Q represent the scale at which the QP perfectly balances gravity, dividing a region of gravitational collapsing instability – $\lambda > \lambda_Q$ – from a region of expansion – for $\lambda < \lambda_Q$ – due to the net repulsive effect of the QP (Chavanis, 2012; Woo and Chiueh, 2009).

In the matter dominated era of an expanding Universe, the general solution of Eq. 3.8 can be expressed as the linear combination of a growing mode $D_+(k, a)$ and a decaying mode $D_-(k, a)$ – as for the CDM case of Eq. 1.58 – that have the form

$$\begin{aligned} D_+(x) &= [(3 - x^2) \cos x + 3 x \sin x] / x^2 \\ D_-(x) &= [(3 - x^2) \sin x - 3 x \cos x] / x^2 \end{aligned} \quad (3.10)$$

where we defined the parameter $x(k, a) = \sqrt{6} k^2 / k_Q^2(a)$. The linear solution, therefore, predicts a suppression of structures in the density field on small scales – i.e. for $k \gg k_Q$ – in which both the growing and decaying mode oscillate in time, effectively halting density perturbation evolution. At large scales – i.e. for $k \ll k_Q$ – the standard linear evolution $D_+ \propto a$ and $D_- \propto a^{-2/3}$ of CDM is recovered thus allowing density perturbation growth (Hu *et al.*, 2000).

The presence of an oscillating regime gives rise to a cutoff of the small-scale density power spectrum similarly to what happens for Warm Dark Matter particle

candidates (Bode *et al.*, 2001b). However, the mechanisms generating such effects in the two cases have a completely different origin – i.e. in FDM perturbations are not washed out by free streaming, but are not allowed to grow in the first place –, resulting in a different shape of the respective transfer functions.

Since the quantum Jeans wavenumber $k_Q(a) \propto a^{1/4}$ increases with time as from Eq. 3.9, we expect oscillating modes to start growing eventually, each at a different redshift, as the quantum Jeans scale passes them. While, in the linear approximation, the fastest possible growth for density perturbation of Eq. 3.10 is the one that characterizes the largest scales $D_+ \propto a$ – making it impossible for the intermediate suppressed scales to catch up with the largest ones – in the non-linear regime we expect a faster growth for the intermediate and small scales at low redshift, allowing such restoring effect.

Therefore, it is necessary to resort on numerical techniques to investigate the detailed integrated effects of these scenarios, and to develop suitable codes to perform N-Body hydrodynamical simulations that could follow their evolution deep into the fully non-linear regime.

3.2 Simulation approach in the literature

FDM non-linear cosmological simulations have been performed over the years either with highly numerically intensive high-resolution Adaptive Mesh Refinement (AMR) algorithms able to solve the Schrödinger-Poisson equations over a grid (see e.g. Schive *et al.*, 2010, 2017) or with standard N-Body codes. However, these include the (linear) suppression only in the initial conditions but neglect the integrated effect of the FDM interaction during the subsequent dynamical evolution, basically treating FDM as standard dark matter with a suppressed primordial power spectrum (see e.g. Schive *et al.*, 2016; Iršič *et al.*, 2017c; Armengaud *et al.*, 2017), similarly to what is routinely done in Warm Dark Matter simulations (Bode *et al.*, 2001b).

The former approach led to impressive results in terms of resolution (Woo and Chiueh, 2009; Schive *et al.*, 2014) but required high computational resources that hindered the possibility of adding a full hydrodynamical description of gas and star formation for cosmologically representative simulation domains. On the other

hand, the latter allows for such possibility because of its reduced computational cost which is, however, gained at the price of the substantial approximation of neglecting QP effects during the simulation (see e.g. [Schive *et al.*, 2014](#)).

In these models the dynamics of FDM particles is influenced – besides gravity – by an additional *Quantum Potential* that we are able to compute exploiting the Smoothed Particle Hydrodynamic routines (as suggested by e.g. [Mocz and Succi, 2015](#); [Marsh, 2015](#)) already implemented in P-GADGET3 for standard hydrodynamical simulations.

Our implementation is flexible enough to easily include models with dark matter self-interaction and allows multiple dark matter species, either fuzzy or not. However, in the present work we focus on the case of a single FDM component accounting for the total dark matter budget. We discuss and compare the results of our algorithm to analytical solutions and the recent results of other similar codes, in order to point out the reliability of our algorithm, its overall performance, as well as the predicted effect of the Quantum Potential on the statistical and structural properties of cosmic structures.

4

AX-Gadget

In this chapter, we present the AX-GADGET code (Nori and Baldi, 2018) we devised following the approach first proposed in Mocz and Succi (2015). AX-GADGET is a modified version of the N-body hydrodynamical cosmological code P-GADGET3 (Springel *et al.*, 2005) that includes the dynamical effect of QP through SPH numerical methods. The explicit approximation of the dependence on neighbouring particles results in a less numerically demanding code with respect to full-wave adaptive grid-based solvers, without compromising cosmological results, with the additional ability to exploit the gas and star physics already implemented in P-GADGET3, along with its more advanced and exotic beyond- Λ CDM extensions such as Modified Gravity (Puchwein *et al.*, 2013) or Coupled Dark Energy models (Baldi *et al.*, 2010).

4.1 The algorithm

The AX-GADGET code (Nori and Baldi, 2018) we developed relies on SPH techniques – already partly implemented in P-GADGET3 – to solve for the QP of Eq. 3.6, computed for each fluid particle through local summation algorithms using Eq. 3.6, and adopt it as an additional source of acceleration in the Euler equation, as suggested by Mocz and Succi (2015); Marsh (2015). To this end, we have equipped dark matter particles in AX-GADGET with an additional data structure to store the necessary quantities that are relevant for the fluid representation of the FDM and similar to the one already in place for gas particles. As for the native SPH implementation of P-GADGET3, the exchange between CPUs of such additional layer of data for local particles is optimised to guarantee high memory efficiency in the domain decomposition.

As described in Section 2.3, SPH provides us with a numerical strategy to approximate continuous fields with sums over neighbouring particles. In such approximations, the deviation of numerical results from the exact solution depends on several factors, related in particular to the intrinsic limitations of a Lagrangian particle description of fluids, where shocks and strong interface interactions tend to be smoothed out or underestimated. However, the flexibility of the method allows rearranging the specific form of the SPH machinery such that equivalent analytical problems can be implemented into flavours of the basic algorithms with different levels of numerical accuracy, as detailed below.

The basic concept behind the SPH approach resides in expressing the value of a given observable O at the position of particle i as the sums of its value over $\text{NN}(i)$ neighbouring particles

$$O_i = \sum_{j \in \text{NN}(i)} m_j \frac{O_j}{\rho_j} W_{ij} \quad (4.1)$$

weighted on mass m_j , density ρ_j and a window function W_{ij} – sometimes referred as the *kernel* function –, which can take many possible functional forms. Consequently, in the standard SPH implementation of P-GADGET3, the derivative of the

observable can be applied to the window function as

$$\vec{\nabla} O_i = \sum_{j \in \text{NN}(i)} m_j \frac{O_j}{\rho_j} \vec{\nabla} W_{ij} \quad (4.2)$$

which, however, does not guarantee that $\vec{\nabla} O$ vanishes for constant values of O .

Therefore, to overcome this problem and to ensure that the overall derivative vanishes in the case of $O_j \rightarrow O_i \forall j \in \text{NN}(i)$, in our implementation we consider a differentiable function Θ such that

$$\vec{\nabla} O = \frac{1}{\Theta} \left[\vec{\nabla} (\Theta O) - O \vec{\nabla} \Theta \right] \quad (4.3)$$

that is translated in the SPH algorithm as

$$\vec{\nabla} O_i = \sum_{j \in \text{NN}(i)} m_j \frac{O_j - O_i}{\rho_j} \frac{\Theta_j}{\Theta_i} \vec{\nabla} W_{ij} \quad (4.4)$$

where the difference of Eq. 4.4 with respect to Eq. 4.2 fulfills the condition of null derivative in the case of a constant field, regardless the form of the function Θ . In the literature, $\Theta = 1$, $\Theta = \rho$ and $\Theta = \sqrt{\rho}$ are the most common choices (see e.g. [Monaghan, 2005](#)). For the different forms of Θ , the derivative of the density field then takes the form

$$\vec{\nabla} \rho_i = \sum_{j \in \text{NN}(i)} m_j \vec{\nabla} W_{ij} (\rho_j - \rho_i) \begin{cases} 1/\rho_i & \text{for } \Theta = 1 \\ 1/\rho_j & \text{for } \Theta = \rho \\ 1/\sqrt{\rho_i \rho_j} & \text{for } \Theta = \sqrt{\rho} \end{cases} \quad (4.5)$$

We noticed that $\Theta = \sqrt{\rho}$ performs better with respect to the other two possibilities in cosmological simulations of FDM, where it is not uncommon to find fluid particles with neighbours with quite different density, for example in collapsing regions. Indeed, $\Theta = 1$ or $\Theta = \rho$ may lead to high and non-symmetrical $i \rightleftharpoons j$ correction factors that are more sensitive to noise and less likely to disappear in the sum, while $\Theta = \sqrt{\rho}$ translates in a more stable algorithm, which makes it

our preferred choice. Nevertheless, the Θ functional forms can be selected upon compilation in our code, so that the final choice is left open.

Even if the first derivative in the form of Eq. 4.2 is quite common in the literature, there is no consensus about the SPH form of the Laplacian.

A straightforward and standard approach consists in applying directly the operator to the window function

$$\nabla^2 O_i = \sum_{j \in \text{NN}(i)} m_j \frac{O_j}{\rho_j} \nabla^2 W_{ij}, \quad (4.6)$$

but, in general, such simple implementation leads to unstable results that are very sensitive to irregularities in the particle distribution, mainly due to the steepness of the second derivative of the kernel function.

For the cases under investigation in the present work, results obtained with this implementation for the computation of the QP led us to unsatisfactory results. In fact, without resorting to any functional correction, the contribution of the Laplacian term $\nabla^2 \rho / \rho$ to the QP in Eq. 3.6 was negligible compared to $|\vec{\nabla} \log \rho|^2$ and thus positive contributions to the QP were underestimated.

A solution to this problem can be derived employing the same approach described above for the first derivative to improve Eq. 4.6, expanding through product derivatives the Laplacian operator as

$$\nabla^2 O = \frac{1}{\Theta} \left[\nabla^2 (\Theta O) - O \nabla^2 \Theta - 2 \vec{\nabla} O \cdot \vec{\nabla} \Theta \right] \quad (4.7)$$

thereby obtaining the correction

$$\nabla^2 O_i = \sum_{j \in \text{NN}(i)} m_j \frac{O_j - O_i}{\rho_j} \frac{\Theta_j}{\Theta_i} \nabla^2 W_{ij} - \frac{2}{\Theta_i} \vec{\nabla} O_i \cdot \vec{\nabla} \Theta_i \quad (4.8)$$

where Θ was chosen coherently with the density correction – i.e. $\Theta = \sqrt{\rho}$ – (for a comparison between different algorithms see [Colin *et al.*, 2006](#)).

A widely used alternative to approximate the Laplacian relies on the symmetry

properties of the window function and was first described in Brookshaw (1985)

$$\nabla^2 O_i = -2 \sum_{j \in \text{NN}(i)} m_j \frac{O_j - O_i}{\rho_j} \frac{\vec{r}_{ij} \cdot \vec{\nabla} W_{ij}}{|r_{ij}|^2} \quad (4.9)$$

being one of the most common strategy due to its computational efficiency deriving from the direct dependence on the first derivative of the kernel (see e.g. Cleary and Monaghan, 1999; Jubelgas *et al.*, 2004; Szewc *et al.*, 2012). It is easy to see that, using Eq. 4.7, an improved version of such scheme reads

$$\nabla^2 O_i = -2 \sum_{j \in \text{NN}(i)} m_j \frac{O_j - O_i}{\rho_j} \frac{\Theta_j}{\Theta_i} \frac{\vec{r}_{ij} \cdot \vec{\nabla} W_{ij}}{|r_{ij}|^2} - \frac{2}{\Theta_i} \vec{\nabla} O_i \cdot \vec{\nabla} \Theta_i \quad (4.10)$$

that, apart from the window function dependence, shares a similar structure and the same computational cost with Eq. 4.8.

The numerical errors of each specific algorithm are linked to the numerical instabilities that may arise from the consecutive derivatives of the window function and the compensation of derivative residuals. To determine which scheme was the most suitable for our work, we investigated different representations of the density gradient and Laplacian.

In Fig. 4.1 we show the QP residuals with respect to the analytical results obtained for a 3D Gaussian density distribution – described in detail in Section 4.2.2 below – using different schemes. Both the standard and corrected version of the Laplacian implementation (*LSPH* and in the Figure) of Eq. 4.6–4.8 and of *à la* Brookshaw implementation (*BSPH* in the Figure) of Eq. 4.9–4.10 are shown. The improvement provided by the correction of the derivatives appears clearly for both methods. Once corrected, the two approaches produce a similar result – due to their analogous structure – that follow well the analytic result, in particular the Laplacian algorithm approaches it from below while the other tends to overestimate it.

We hereafter adopt as our preferred algorithm the corrected Laplacian version of Eq. 4.8 as it statistically performs better and, as for the Θ function, the other scheme

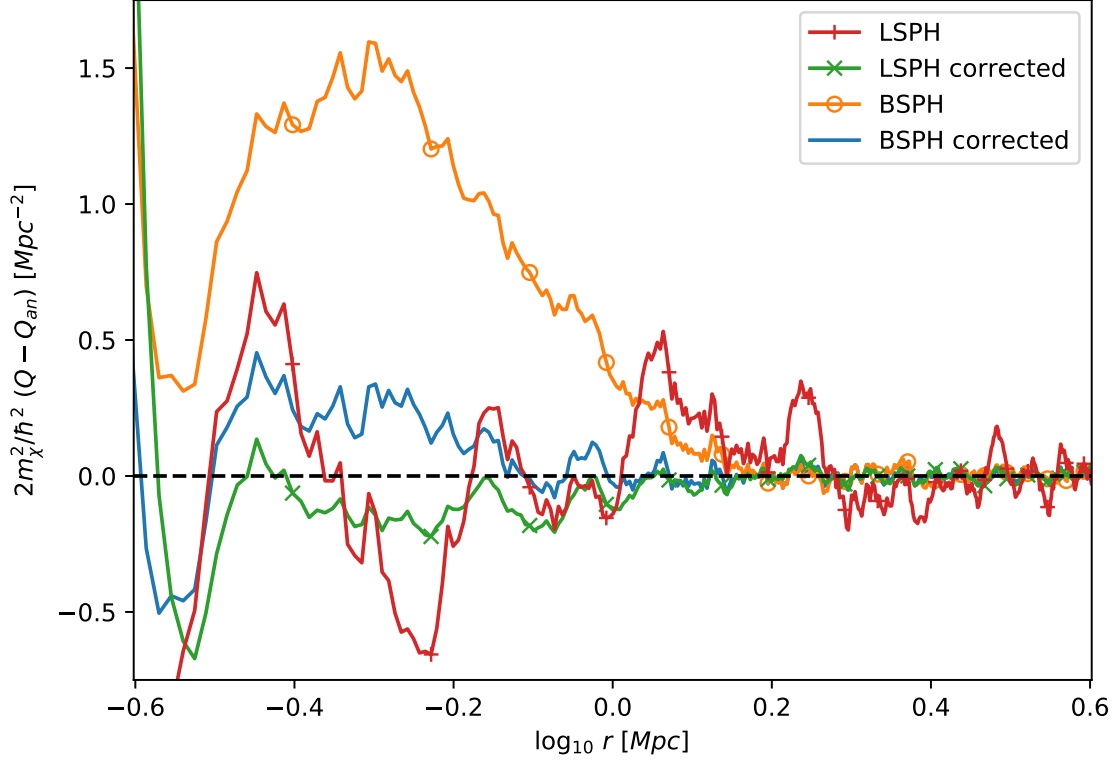


Figure 4.1: Quantum Potential residuals obtained with different algorithms for a 3D Gaussian density distribution. The results displayed are derived with the Laplacian scheme (LSPH) of Eq. 4.6–4.8 and with the *à la* Brookshaw (BSPH) scheme of Eq. 4.9–4.10, both presented with and without derivative corrections.

can be selected upon compilation of the code. We further discuss and motivate our choices, providing some comparisons and analytical tests, in Section 4.2.

The window function used in the code is the cubic B-Spline routinely employed in P-GADGET3 SPH simulations:

$$W(r, h) = \frac{8}{\pi h^3} \begin{cases} 1 - 6(r/h)^2 + 6(r/h)^3 & \text{if } 0 < r/h \leq 1/2 \\ 2(1 - r/h)^3 & \text{if } 1/2 < r/h < 1 \\ 0 & \text{otherwise} \end{cases} \quad (4.11)$$

with r and h being the distance between particles and the smoothing length, respectively. We denote $W_{ij} = W(r_{ij} = |\vec{r}_j - \vec{r}_i|, h_i)$. Other higher order functionals are

implemented in P-GADGET3 as the quintic B-Splines, or the C4 and C6 Wendland functions (Wendland, 1995) which, however, require a higher number of neighbours to be taken into account (see e.g. Dehnen and Aly, 2012, for comparison between window functions). We find no critical variation in accuracy for the calculation of the QP and its derivative when different window functions are used.

Following the standard SPH approach, the value of the single particle smoothing length h_i is varied at each timestep to satisfy the condition

$$\frac{4}{3}\pi h_i^3 \rho_i = \sum_{j \in \text{NN}(i)} m_j = M \quad (4.12)$$

such that its corresponding sphere encloses enough neighbours $\text{NN}(i)$ to match a given amount of mass M . With h free to vary, the condition above can be enforced through a Lagrangian multiplier and h -derivatives enter the equations.

In order to preserve energy and entropy conservation of the algorithms – at least in the appropriate limits –, it is imperative to take into account the terms arising from the variation of the smoothing length h required to satisfy Eq. 4.12. To do so, we follow the approach described in Springel and Hernquist (2002), where Lagrangian multipliers are introduced to keep track of h -derivative terms.

Let us consider a generic Lagrangian for a FDM N-body ensemble with the form

$$\begin{aligned} \mathcal{L}(\vec{q}, \dot{\vec{q}}) = & \sum_{i=0}^N \frac{1}{2} m_i |\dot{\vec{r}}_i|^2 - m_i \frac{P_i}{\rho_i^2} \\ & + \frac{\hbar^2}{2m_\chi^2} m_i \frac{\nabla^2 \sqrt{\rho_i}}{\sqrt{\rho_i}} + \lambda_i (V_i \rho_i - M) \end{aligned} \quad (4.13)$$

expressed in terms of the variables $\vec{q}_i = (\vec{r}_i, h_i)$ and where the different terms represent the kinetic energy, the self-interaction between particles – described through a pressure function P – and the QP contribution. The last term enforces Eq. 4.12 through N Lagrangian multipliers λ .

The set of equations of motion linked to the multipliers, one for every j particle

in the ensemble, results in

$$\lambda_j = \left(1 - \frac{1}{f_j}\right) \frac{m_j}{V_j} \left[\frac{P_j}{\rho_j^2} - \frac{\hbar^2}{m_\chi^2} \partial_{\rho_j} \left(\frac{\nabla^2 \sqrt{\rho_j}}{\sqrt{\rho_j}} \right) \right] \quad (4.14)$$

where we defined the parameters f as

$$f_j = \left(1 + \frac{\hbar}{3\rho_j} \partial_h \rho_j\right) \quad (4.15)$$

that we use in the text (notice that our definition of f the inverse with respect to the one in [Springel and Hernquist, 2002](#)). Substituting the Lagrangian multipliers, the set of equations of motion related to the positions \vec{r} can be expressed as

$$m_i \ddot{\vec{r}}_i = - \sum_{j=0}^N \left[\frac{m_j}{f_j} \frac{P_j}{\rho_j^2} \vec{\nabla} \rho_j + \frac{\hbar^2}{2m_\chi^2} \frac{m_j}{f_j} \vec{\nabla} \left(\frac{\nabla^2 \sqrt{\rho_j}}{\sqrt{\rho_j}} \right) \right] \quad (4.16)$$

which then can be implemented through SPH algorithms. To summarise, the adaptive adjustment of the smoothing lengths of every single particle contributes to particle accelerations through terms involving h -derivatives that can be expressed as f factors in the SPH neighbours summation.

Given that the quantum acceleration $\vec{\nabla} Q$ is proportional to a third order derivative of the density field, it is impossible to build an iterative SPH algorithm with less than three cycles over all particles. Therefore, our implementation can be schematically summarised by three cycles of computation. The first one for the density:

$$\rho_i = \sum_{j \in \text{NN}(i)} m_j W_{ij}, \quad (4.17)$$

the second one for its gradient and Laplacian:

$$\vec{\nabla}\rho_i = \sum_{j \in \text{NN}(i)} m_j \vec{\nabla}W_{ij} \frac{\rho_j - \rho_i}{\sqrt{\rho_i \rho_j}} \quad (4.18)$$

$$\nabla^2 \rho_i = \sum_{j \in \text{NN}(i)} m_j \nabla^2 W_{ij} \frac{\rho_j - \rho_i}{\sqrt{\rho_i \rho_j}} - \frac{|\vec{\nabla}\rho_i|^2}{\rho_i}, \quad (4.19)$$

and the third one to build, using Eq. 3.6, the QP contribution to acceleration:

$$\vec{\nabla}Q_i = \frac{\hbar^2}{2m\chi} \sum_{j \in \text{NN}(i)} \frac{m_j}{f_j \rho_j} \vec{\nabla}W_{ij} \left(\frac{\nabla^2 \rho_j}{2\rho_j} - \frac{|\vec{\nabla}\rho_j|^2}{4\rho_j^2} \right). \quad (4.20)$$

It would be legitimate, however, to choose different ways to break down the derivatives into lower order sums on neighbouring particles following the SPH prescriptions. Regardless of the specific formulation chosen, the algorithm should always be tested against known analytical solutions, in order not to trade better performance off for less accurate results. In the next Section, we present a series of basic tests of our FDM implementation showing that the original SPH formulation results in a very poor accuracy of the numerical solution for the QP, while our improved strategy provides much better results.

4.2 Analytical tests

In this Section, we test the accuracy of the algorithm described in the previous Section by comparing, for some particular density distributions, the solution of the QP obtained from our implementation to the analytic one. We also compare our improved SPH scheme for spatial derivatives with the results obtained through the standard SPH implementation of P-GADGET3.

To this end, we have tailored the matter density distribution in our tests – through inverse transformation sampling –, both in one and three dimensions, to match some specific analytical forms by rearranging the spatial distribution of particles while keeping their individual mass constant. This implies a local variation of the SPH smoothing length from particle to particle as it usually happens in standard

astrophysical and cosmological application of the SPH method. The spatial degrees of freedom not relevant for the test distributions are uniformly randomised in order to average out their contribution to Q . In Fig. 4.2 we display four maps representing the matter density distribution and the QP spatial distribution for the first two analytical test considered – a 1D hyperbolic tangent front and a 3D Gaussian matter distribution – which are described in detail in the following Subsections.

The results obtained using a standard SPH algorithm through the original formulation of Eq. 4.6 and our modified implementation of Eq. 4.8 are presented to emphasise the importance of derivative corrections in the algorithm.

To be thorough, and to assess the impact of variable smoothing length on the accuracy of the solution, we also show a comparison with results obtained from a homogeneous distribution of particles with spatially variable mass that reproduce the same overall density distribution.

The test simulations feature 256^3 particles in a $L = 10$ Mpc non-periodic box. Initial conditions, built accordingly to each test, are read by the code, and a snapshot with QP information is instantly produced.

Finally, our last test focuses on the dynamical evolution of a self-gravitating system, in which the balance between the opposite effects of the gravitational and quantum potentials lead to a stable solution and the formation of a solitonic core.

4.2.1 1D Density Front

As a first analytical test, we consider the case of a 1D density front described by a hyperbolic tangent in the form of

$$\rho(x, \sigma, c) = \rho_0 \left(c + 1 - \tanh \frac{x}{\sigma} \right) \quad (4.21)$$

where σ defines the sharpness of the front while c is used to parametrize the the density contrast at the left of the front with respect to a background density on its right.

For such density profile, the QP has the analytical form

$$Q(x, \sigma, c) = -\frac{\hbar^2}{8m^2\sigma^2} \frac{1-t^2}{(c+1-t)^2} [1-4t(c+1)+3t^2] \quad (4.22)$$

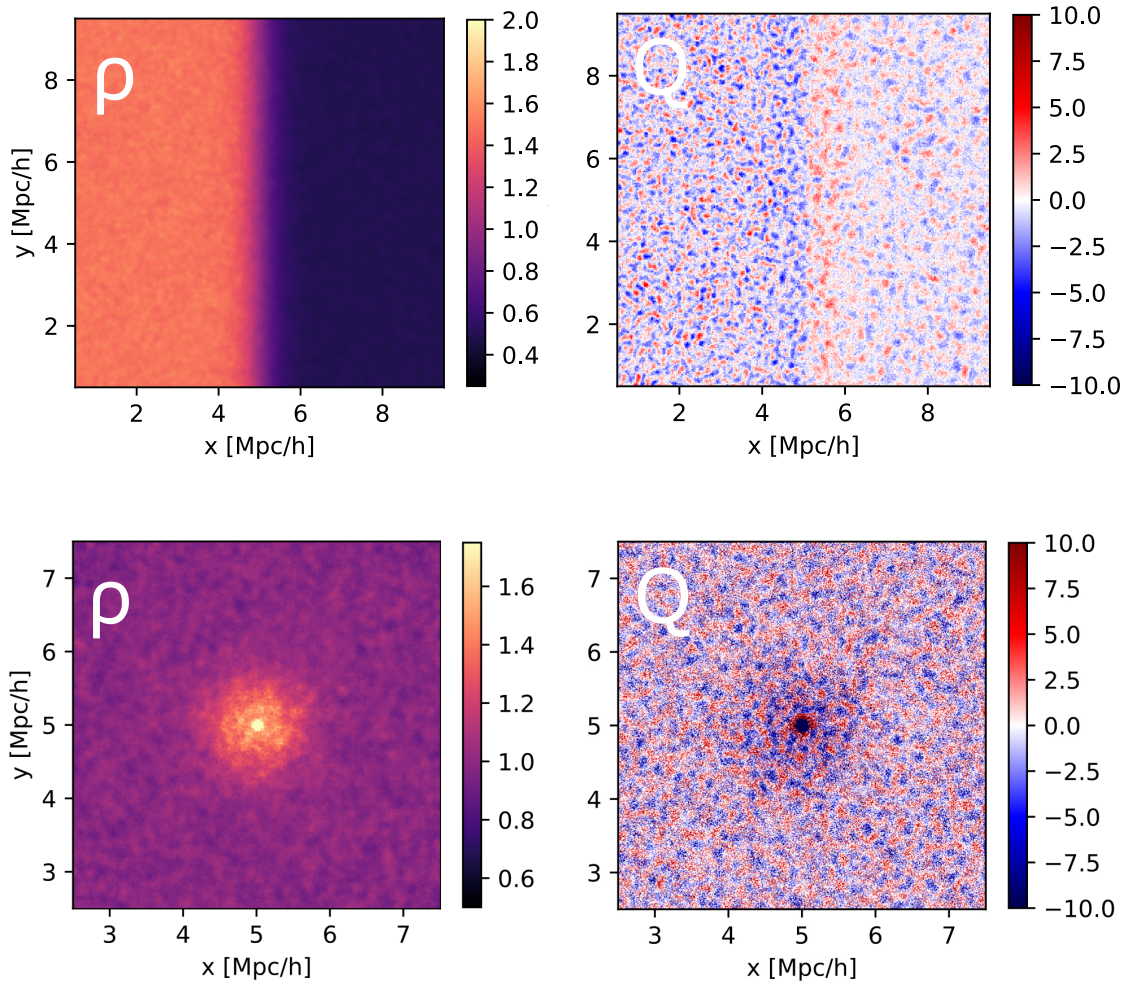


Figure 4.2: Matter density and Quantum Potential maps obtained for the two analytical density distributions considered for code validation: a 1D hyperbolic tangent front along the x -axis (*top panels*) and a 3D Gaussian (*bottom panels*) distribution.

expressed in terms of $t(x, \sigma) = \tanh \frac{x}{\sigma}$.

In Fig. 4.3 we show the profile for the density, its gradient, and the QP as computed for such density distribution in different setups: a regular grid configuration of particles with variable mass (*left panels*) and a spatial rearrangement of constant mass particles, the latter analysed with and without the derivative corrections (*centre* and *right* panels, respectively). In particular, the distribution used has the form of Eq. 4.21 centered at 5 Mpc, with $\sigma = 500$ kpc and a background parameter $c = 1$.

First of all, we notice how the idealised setup with a regular grid of particles with variable mass provides the most accurate solution for all quantities. This is not surprising and reflects an intrinsic limitation of the SPH algorithm in the computation of spatial derivatives for situations where the density distribution features steep gradients and consequently neighbouring particles have significantly different smoothing lengths. By keeping particles on a fixed grid and changing their mass – still basing the computation of the SPH smoothing length on the desired number of neighbour particles – we obtained identical smoothing lengths for all particles.

Secondly, it is easy to see that our correction of the derivative scheme significantly improves the QP computation whose accuracy gets closer to the idealised variable mass case.

As one can see in the plots, the QP resulting from a 1D hyperbolic tangent front features a negative peak on the densest side and a positive one towards the less dense region. This corresponds to positive and negative accelerations on the two sides, respectively, implying that the QP tends to push matter towards the region of steep density variation. Such behaviour has interesting consequences, in particular for cosmological structure formation. More specifically, this modulation of the QP may show up in cosmic walls and filaments, where a 1D density front – Cartesian or radial, respectively – can represent the local matter distribution. In order to provide a direct evidence of such effect, we show in Fig. 4.4 a map of the QP contrast – i.e. the relative difference of the QP to the average QP – at redshift $z = 1$ from a cosmological simulation of Axion Dark Matter performed with AX-GADGET for an FDM mass of $m_\chi = 10^{-22}$ eV/ c^2 , where negative and positive regions for the QP are marked in blue and red, respectively. As one can see from the Figure, the QP fol-

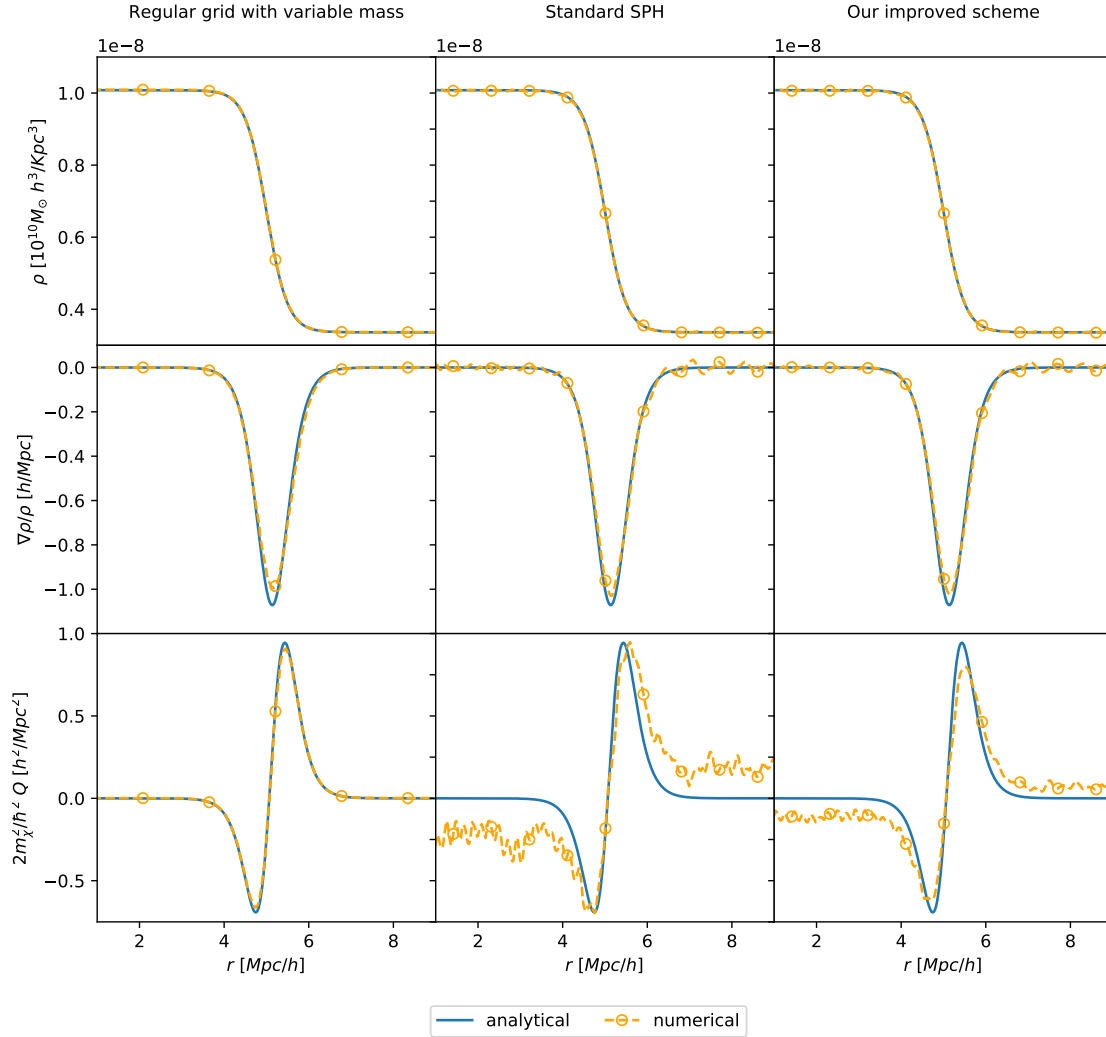


Figure 4.3: Density profile (*top row*), Density gradient (*mid row*), and Quantum Potential (*bottom row*) obtained for the same hyperbolic tangent front density distribution along the x axis. On the *left* column we show results obtained when the density distribution is built by changing the mass of particles set on a regular grid, while in the *center* and *right* columns we show the case of keeping the mass constant and rearranging the spatial distribution of particles, using either the original P-GADGET3 SPH scheme or our improved implementation, respectively.

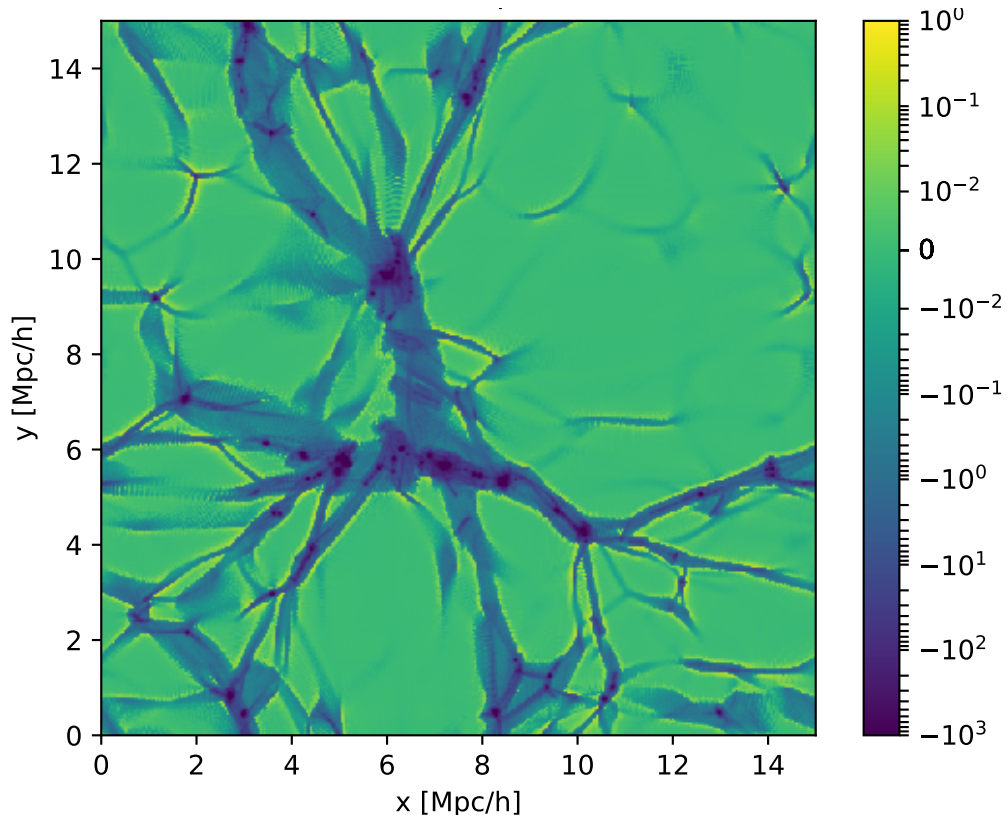


Figure 4.4: Quantum Potential map at $z = 1$ of a FDM cosmological simulation with $m_\chi = 10^{-22}$ eV/ c^2 in 750 kpc/ h slice of a 15 Mpc/ h side box. The potential is contrasted with its mean value to emphasize spatial distribution, therefore expressed in dimensionless units.

lows the underlying cosmic web of collapsed structures, and shows negative wells corresponding to the densest regions while approaches zero in voids, as expected. It is also clearly visible how positive regions surround structures – filaments and walls in particular – that separate voids, confirming the analytical result obtained above.

4.2.2 3D Gaussian distribution

To idealize a spherical collapsed system we used as pivotal test a 3D Gaussian overdensity, that we parametrized as

$$\rho(r, \sigma, c) = \rho_0 \left(c + e^{-r^2/2\sigma^2} \right) \quad (4.23)$$

where σ is the standard deviation of the distribution and c is linked to the relative density of the Gaussian perturbation with respect to the background average.

For $c \rightarrow 0$, representing the Gaussian density distribution in vacuum space, $Q(x, \sigma, 0)$ collapses into a parabolic function that diverges at infinite distance. This implies an unphysical limit in which distant particles have infinite acceleration (proportional to $\vec{\nabla}Q$).

In fact, using Eq. 3.6 the QP functional form is

$$Q(r, \sigma, c) = \frac{\hbar^2}{4m^2\sigma^2} \chi \left[-3 + \frac{r^2}{2\sigma^2} (2 - \chi) \right] \quad (4.24)$$

where we introduced the dimensionless variable $\chi(r, \sigma) = (1 + c \exp(r^2/2\sigma^2))^{-1}$.

As soon as c becomes different from zero, the divergence of the QP is cured and a positive peak appears outside the central negative well, similarly to the previous case, before the function decays to zero at larger distances. The resulting acceleration

$$\vec{\nabla}Q(r, \sigma, c) = \frac{\hbar^2}{4m^2\sigma^3} \chi \left[5 - 4\chi - \frac{r^2}{\sigma^2} (1 - \chi)^2 \right] \frac{\vec{r}}{\sigma} \quad (4.25)$$

is therefore pointing outwards in the central overdensity region and inwards in a small spherical shell in the outskirts of the overdensity.

This non-linear behaviour in a simple Gaussian distribution is emblematic of how the QP is hardly representable with other effective functionals such, for exam-

ple, a polytropic function $Q \propto \rho^\gamma$ typical of pressure-like components that would feature a monotonic behaviour (i.e. with an acceleration with fixed sign) whatever its specific form.

In Fig. 4.5 we display the density profile, its gradient, and the resulting QP for the 3D Gaussian distribution of Eq. 4.23 around the center of a 10 Mpc non-periodic box, with $\sigma = 500$ kpc and a background parameter $c = 1$.

As the Figure shows, the role of our derivative correction is relevant, since the standard SPH approach results in an overestimation of the depth of the central well lacking positive peaks surrounding it. From the numerical point of view, our analysis suggests that the primary source of error comes from a substantial underestimation of the Laplacian since it is the only term bearing a positive contribution.

4.2.3 Solitonic core

The last test we present features the dynamical evolution of an analytical distribution, in order to test the correctness of our implementation of FDM dynamics over time. The starting point is again a 3D Gaussian distribution

$$\rho(r, \sigma) = \rho_0 e^{-r^2/2\sigma^2} \quad (4.26)$$

which is left free to evolve under the influence of both gravitational and quantum potential, in static space set-up.

The stable solution of the density distribution for this system – representing a *solitonic* solution – has no analytical form but can be expressed in an approximated form as

$$\rho(r, \sigma) \xrightarrow{t \rightarrow \infty} \rho(r, r_c) = \rho_c [1 + \alpha r^2/r_c^2]^{-8} \quad (4.27)$$

where the parameter $\alpha = \sqrt[8]{2} - 1$ is defined such that the the radius r_c is the radius at which the density is halved with respect to the central peak ρ_c satisfying $\rho(r = r_c) = \rho_c/2$ (see e.g. [Guzman and Urena-Lopez, 2006](#); [Schive *et al.*, 2014](#); [Marsh and Pop, 2015](#)).

We choose a non-periodic box of 10 Mpc side length, with a Gaussian distribution with $\sigma = 500$ kpc and a mass $m_\chi = 10^{-26}$ eV/ c^2 for the FDM bosonic field.

In Fig. 4.6 is shown the relaxed radial density distribution obtained for such

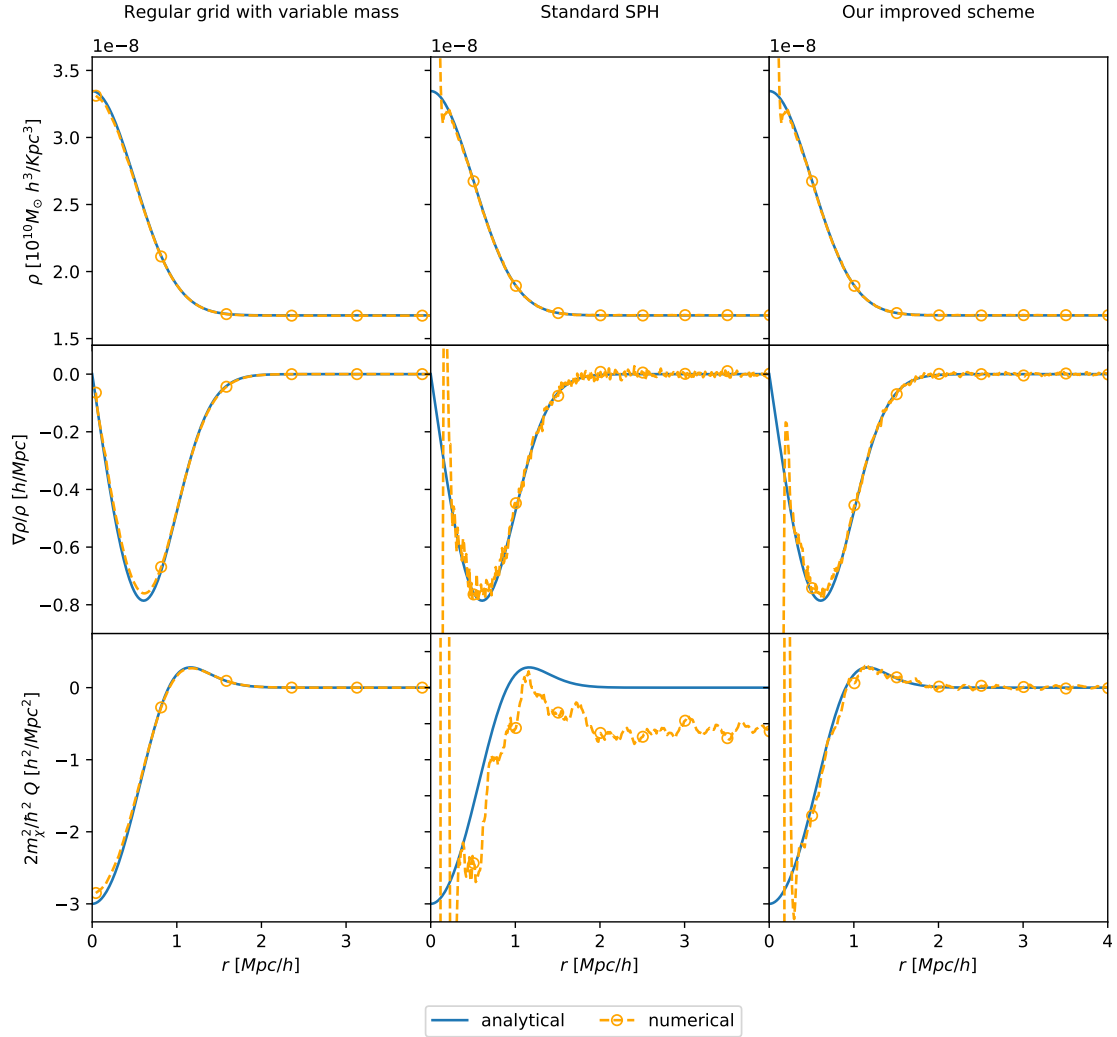


Figure 4.5: Density profile (*top row*), Density gradient (*mid row*), and Quantum Potential (*bottom row*) obtained for the same 3D Gaussian density distribution. On the *left* column we show results obtained when the density distribution is built by changing the mass of particles set on a regular grid, while in the *center* and *right* columns we show the case of keeping the mass constant and rearranging the spatial distribution of particles, using either the original P-GADGET3 SPH scheme or our improved implementation, respectively.

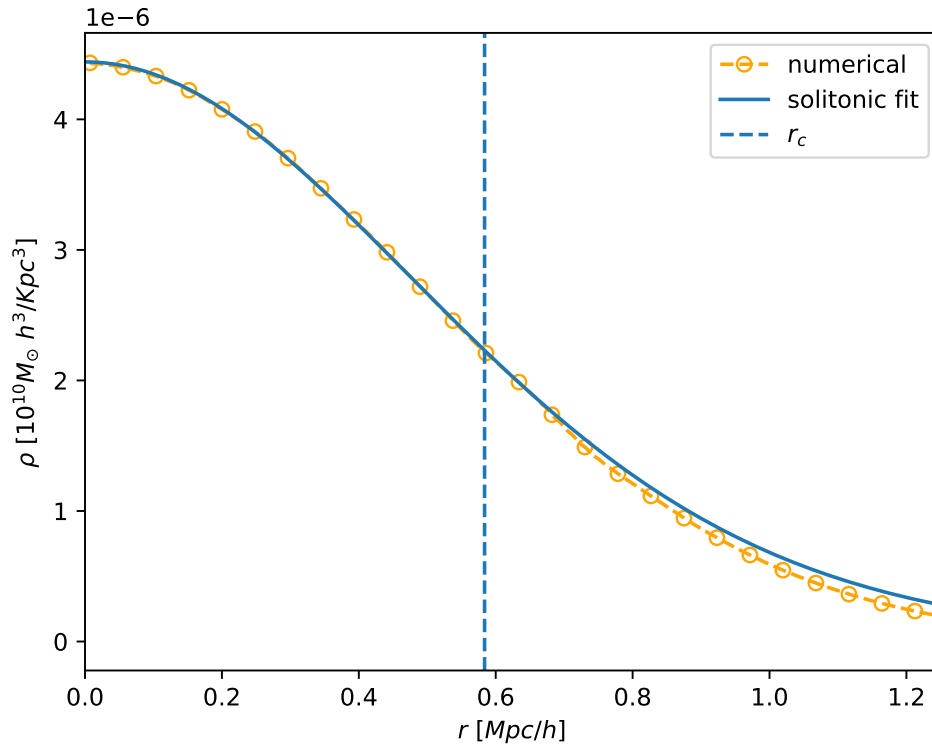


Figure 4.6: Stable density distribution obtained by letting a 3D Gaussian distribution relax over time under the combined effect of gravitational and quantum potentials. The numerical result matches the solitonic core functional form of Eq. 4.27, which parameter r_c is represented by the vertical dashed line.

setup, which is consistent with the approximated solitonic functional form of Eq. 4.27 with r_c represented by the vertical dashed line. In this idealised test, we added an artificial velocity-dependent friction – i.e. a $\gamma \vec{v}$ term with $\gamma < 0$ – in the Euler equation in order to let the system settle in its ground state more gracefully and achieve stability.

This last test is in line with the theoretical predictions and numerical results in the literature, assessing that the QP can indeed support the formation of stable and cored structures (Schive *et al.*, 2014; Marsh and Pop, 2015) and that our implementation is capable of capturing such relaxation process. In a cosmological setup, since the scale of equivalence between the two potentials λ_Q evolves in time, such solitonic cores are expected to be found only at the centre of small and dense dark matter haloes which had enough time to relax dynamically.

Therefore, by comparing our results with both analytical predictions and numerical results in the literature (see e.g. Woo and Chiueh, 2009; Mocz *et al.*, 2018) for static and evolving systems, we feel confident that the algorithm implemented in AX-GADGET can be considered accurate and robust, and we now move on to test the effects of FDM with our modified code on more realistic cosmological setups.

4.3 Cosmological tests

In this Section, we discuss the results of a series of cosmological test simulations, to understand the effects of the QP on the overall dynamics of FDM and its role in the evolution of the large-scale structures of the universe.

Even though AX-GADGET allows for any possible mixture of CDM and FDM particles sharing the overall matter budget of the universe, as well as for different possible self-interaction mechanisms, we restrict our tests to the effects of the QP alone for a single FDM component accounting for the total dark matter density and leave the exploration of more complex models for future work.

The dynamical effect induced by the QP during cosmic evolution is investigated and compared to the result of the widely-adopted approximation (see e.g. Schive *et al.*, 2016; Kobayashi *et al.*, 2017; Iršič *et al.*, 2017c) consisting in imposing the predicted suppression of small-scale perturbations – as computed by linear codes such as e.g. axion-CAMB (Hlozek *et al.*, 2015) – in the initial conditions only. The details

Table 4.1: Summary of the simulations presented in this work and their properties.

Model	IC	QP	m_χ	N_{part}	Boxsize [Mpc ³]	M_{part} [10 ⁶ M_\odot]	$z_{start} - z_{end}$	Time [h on 1024 CPU]
CIC1000	standard	×	-	256 ³	10	5.110	999 – 0.5	-
CIC+QP1000	standard	✓	1/√2	256 ³	10	5.110	999 – 0.5	-
CIC	standard	×	-	512 ³	15	2.156	99 – 3	6.98
CIC+QP	standard	✓	1	512 ³	15	2.156	99 – 3	38.09
FIC	suppressed	×	-	512 ³	15	2.156	99 – 3	7.29
FIC+QP	suppressed	✓	1	512 ³	15	2.156	99 – 3	38.27

regarding each simulation are listed in Table 5.1. The cosmological parameters used are the one of [Ade et al. \(2016\)](#).

In order to highlight the effects of the QP on structure formation and – more importantly – the ability of AX-Gadget to correctly follow FDM dynamics, we choose a mass of the FDM boson field $m_\chi \leq 10^{-22}$ eV/ c^2 . A single FDM component with such low mass is disfavoured by linear studies [Hlozek et al. \(2015\)](#) and by numerical simulations based on a suppressed initial density power ([Iršič et al., 2017c](#)). However, in the present work we are mostly interested in testing our code in the case of a strong QP effect in order to emphasise observable consequences of FDM on cosmological evolution and numerically stress the code.

In these simulations, we are not able to see the formation of interference patterns or solitonic cores – as in Section 4.2.3 – since we are not able to probe such high-resolution effects. With much higher resolution future simulations we plan to investigate the ability of our SPH scheme to capture such small-scales characteristic FDM footprints and large-scale structures at the same time, as has been done with other grid-based codes in the literature ([Schive et al., 2014](#); [Mocz et al., 2018](#)).

4.3.1 Quantum Potential effects on dynamics

To isolate the impact of the QP on the dynamics and on the evolution of large-scale structures, we first performed two simulations – termed CIC1000 and CIC+QP1000 in Table 5.1 – evolved with CDM and FDM dynamics – i.e. with

standard P-GADGET3 and AX-GADGET, respectively – but starting from the same initial conditions. Therefore, any difference in the dynamical evolution between the two runs is the result of the QP acceleration contribution exclusively. The power spectrum used for the initial particle configuration is that of Λ CDM, specifically the Eisenstein and Hu spectrum (Eisenstein and Hu, 1998), in order to avoid additional effects arising from the suppression that a light non-thermal boson field would imply (Hu *et al.*, 2000).

Since the initial conditions that we adopt feature a higher amplitude of density perturbations at small scales than FDM would allow, we set the starting time of the simulation at a very high redshift $z = 999$ in order to allow sufficient time for the system to adjust. Such approach has been already employed to quantify the QP effects on structure formation for full-wave solver codes (see e.g. Woo and Chiueh, 2009), and our tests, therefore, allow for a direct comparison with these previous works.

In Fig. 4.7 we display maps of the density field (*left column*), the QP (*central column*) and the gravitational potential (*right column*) of the CIC+QP1000 simulation at different redshifts. At high redshift, the density contrast is still smaller, and the QP is strongly affecting scales $k \lesssim 1 h/\text{Mpc}$ throughout the simulation box – thereby counteracting gravitational instability at these scales – while the gravitational potential wells start to induce matter collapse on larger scales. As the system evolves, dark matter starts to accrete on seed overdensities under the effect of gravity and eventually collapses into structures while drifting away from low-density regions, thus inducing the QP to intensify in the infalling regions – actively counteracting matter accretion – and to weaken its action elsewhere. At lower redshifts, the scale at which the QP is still able to contrast the gravitational potential reduces – because of the redshift dependence of the associated Jeans scale of Eq. 3.9 – and its distribution follows the dark matter structures shaped by the gravitational potential.

In Fig. 4.8 we show the matter power spectra of both simulations (in the *upper panel*) and their ratio (in the *lower panel*). It appears clear from the evolution of the power spectra that the QP dynamically suppresses the power at small scales, as expected. Both the intensity and the scale of this suppression are redshift dependent, and the evolution of the system can be split into three main phases. In the

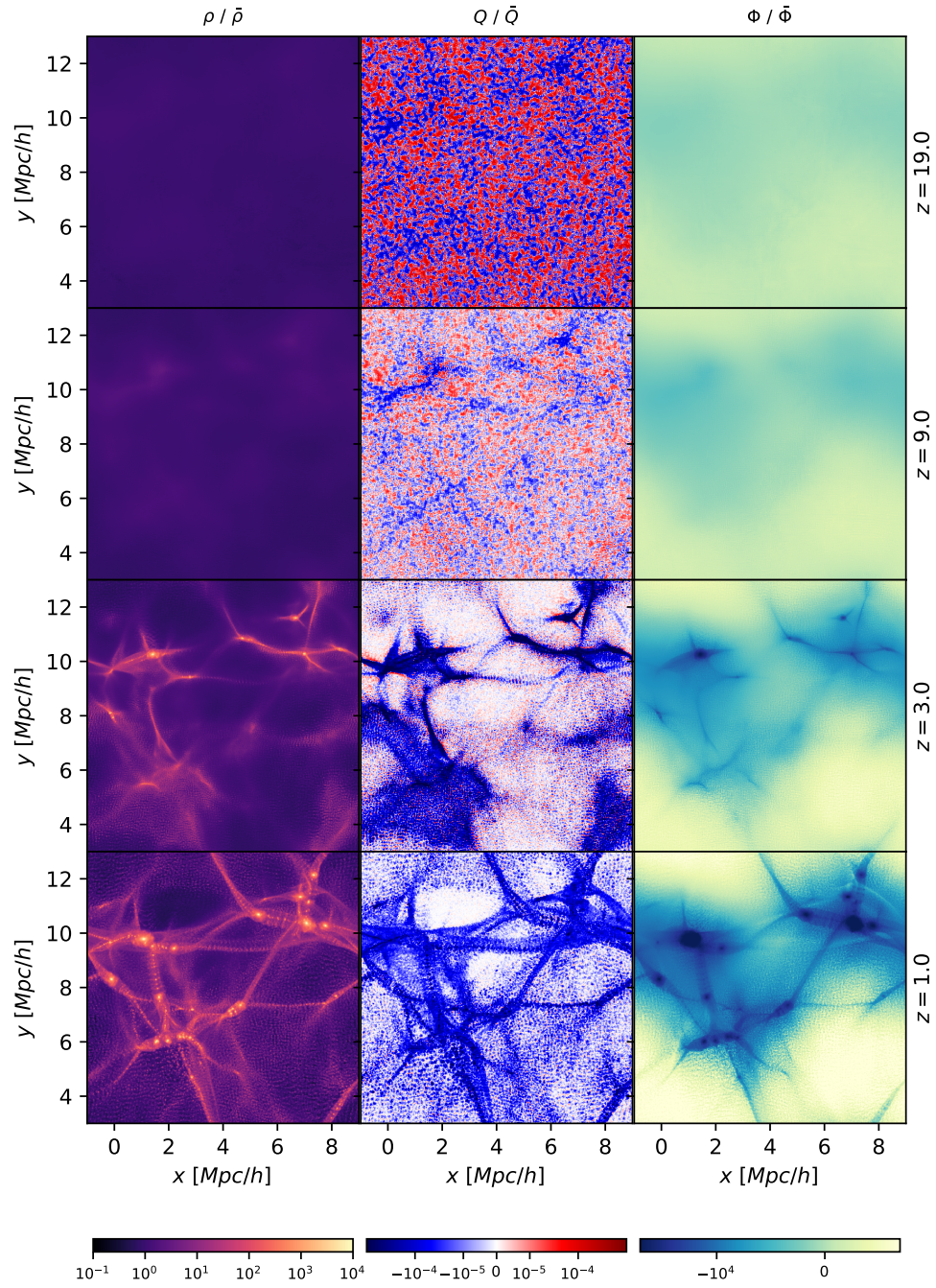


Figure 4.7: Maps of a 500 kpc/h slice of the density field (*left column*), the Quantum Potential (*center column*) and the gravitational potential (*right column*) of the FDM simulation, at different redshifts. Observables are contrasted with mean values to emphasize spatial distribution, therefore expressed in dimensionless units.

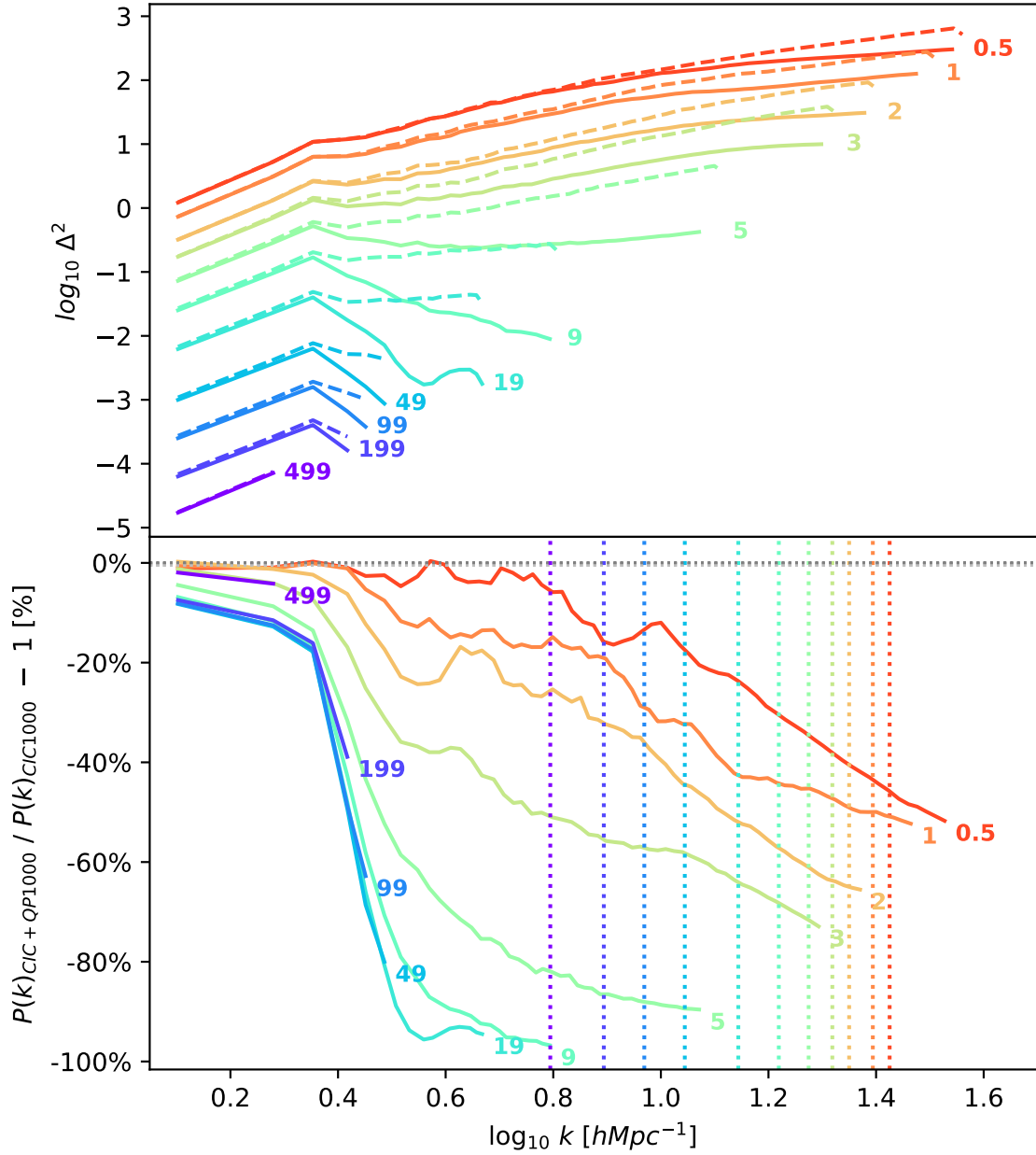


Figure 4.8: *Top:* Dimensionless matter power spectra of simulations with QP (solid) and without QP (dashed), both evolved from $z = 999$ CDM initial condition, labelled redshift-wise. *Bottom:* Relative difference of matter power spectra between the simulations. The vertical dashed lines represents the $k_{1/2}$ coming from linear theory defined as the scale at which the predicted power spectrum suppression is 50%.

first phase, at high redshifts – up to $z \sim 19$ –, the QP fluctuations dominate over the gravitational potential at small scales, resulting in a strong suppression of the initial power spectrum.

As the system evolves, it enters a second phase (from $z \sim 19$ to $z \sim 3$ in our plots) where the action range of the QP gets smaller and smaller (as described by its characteristic length k_Q in Eq. 3.9) and it is no longer able to counteract the gravitational potential on larger scales. Structures begin to form at scales larger than k_Q as the gravitational instability induces matter collapse, thereby increasing density gradients in the collapsing regions and consequently intensifying the repulsive action of the QP in the central parts of the forming halos.

Such first dramatic rearrangement of the initial conditions followed by a smoother evolution, in line with what is found in [Woo and Chiueh \(2009\)](#), is due to the fact that the CDM initial conditions are not an equilibrium solution in the presence of QP, so that the system suddenly rearranges to recover an equilibrium setup. Unfortunately, the significant difference in resolution between our runs and those of [Woo and Chiueh](#) prevents a detailed quantitative comparison of this sharp transition between the two studies.

Finally, at even lower redshifts (from $z \sim 3$ onward) gravity has shaped the large-scale structures and both potentials - effectively acting one against the other - follow the matter distribution and relax to an equilibrium state.

The suppression of the power spectrum – displayed in Fig. 4.8 – shows no dramatic change in slope while it shifts towards lower and lower scales, suggesting that the evolution of perturbations is mostly due to the dynamical balance at all scales of the two potentials as the universe expands and the quantum Jeans length shrinks.

As a test of the dynamical evolution of the system in the N-body simulation, we can compare our results with the linear prediction for $k_{1/2}$, which is defined as the scale satisfying $P_{\text{FDM}}(k_{1/2})/P_{\text{CDM}}(k_{1/2}) - 1 = -0.5$ (see e.g. [Hu et al., 2000](#)). In the bottom panel of Fig. 4.8 the vertical dashed lines represent $k_{1/2}$ for each redshift.

In the first phases of the simulation – when the system quickly shocks from the non-equilibrium configuration of the initial conditions – the linear prediction is far from being realised, while in the last phase, when sufficient time has been allowed

for the system to settle to the new equilibrium configuration, we progressively approach the linear result as the universe evolves to the present epoch. Such asymptotic recovery of the linear predictions at low redshifts represents a successful test for our QP implementation: given enough time, the QP is able to prevent structure formation at small scales – even when CDM initial conditions are used – effectively suppressing the matter power spectrum as we would expect from theory. Nonetheless, we stress here that we do not expect to recover precisely the predicted value of $k_{1/2}$ at low redshift as the latter was computed within a linear approximation while our implementation is able to follow the evolution of structures under the joint effects of gravity and the QP down to the fully non-linear regime.

4.3.2 *Quantum Potential and initial conditions*

As we showed in the previous Subsection, comparing the evolution of CDM initial conditions with and without accounting for the QP in the dynamics provides a clear example of the QP effect on structure formation and evolution, namely a repulsive contribution to acceleration within collapsed structures that counteracts the attractive pull of gravity. However, such setup is not a realistic representation of structure formation within the FDM framework, for which a suppression of the density perturbations power at small scales would already be in place at arbitrarily high redshifts, and therefore should be already accounted for in the initial conditions setup (see again [Hu *et al.*, 2000](#)).

A lower small-scale power translates automatically into a late-time shortage of low-mass structures, so different works (see e.g. [Schive *et al.*, 2016](#); [Armengaud *et al.*, 2017](#); [Iršič *et al.*, 2017c](#)) have been suggesting that it might be appropriate – under some circumstances – to completely neglect the effects of the QP in the dynamics of the simulations and simply account for the FDM phenomenology through a cutoff in the initial conditions power spectrum, similarly to what happens for the case of Warm Dark Matter scenarios (see e.g. [Bode *et al.*, 2001b](#)). However, proper validation of such approach has not yet been performed in sufficient detail, and a quantitative assessment of the impact of the QP in the dynamics of structure formation on top of a cutoff in the primordial power spectrum has to be made in order to allow fully accurate predictions of the non-linear FDM footprints.

To this end, in order to investigate the relative impact on structure formation of the two approaches, we performed a second set of four simulations – termed CIC, CIC+QP, FIC, FIC+QP – representing four combinations obtained from both suppressed (FIC) and non-suppressed (CIC) initial conditions evolved either with (+QP) or without the QP in the dynamics, as listed in Tab. 5.1.

Obviously, the CIC run corresponds to a standard Λ CDM simulation while FIC+QP represents the closest setup to the real FDM model, including the effects of the QP both in the initial conditions and in the subsequent dynamical evolution of structures.

As already pointed out in Section 3.1, the matter power spectrum to be taken into account in building the initial conditions for FDM simulations features a mass- and redshift-dependent cutoff, at a scale given by Eq. 3.9. In order to set up the FIC initial conditions, we resorted on the publicly available and widely used code axion-CAMB (Hlozek *et al.*, 2015), a modified version of the public code CAMB (Lewis *et al.*, 2000), to compute the suppressed power spectrum at the starting redshift of our simulations, $z = 99$.

In Fig. 4.9 we display the relative difference of the matter power spectrum in the four simulations with respect to the reference CIC run. As one can see from the plots, the four simulations are paired at the starting time in the two different initial conditions FIC and CIC (*top-left pane*), and immediately decouple under the effect of the QP (*top-right panel*). The small-scale overdensities are either disrupted (for the CIC+QP case) or frozen (for the FIC+QP case) by the QP, and this results in a drop of the power spectrum compared to the corresponding runs without QP. At lower redshifts, the maximum suppression with respect to the reference CIC run is obtained for the FIC+QP simulation, which features an additional $\approx 5 - 10\%$ suppression (depending on the redshifts) at small scales compared to the FIC case where the suppression is only imprinted in the initial conditions. This result seems to suggest that the approximate treatment of neglecting the QP in the dynamical evolution of a suppressed primordial matter power spectrum – that has been widely employed in the literature (see e.g. Schive *et al.*, 2016; Armengaud *et al.*, 2017; Iršič *et al.*, 2017c) – may not be sufficient for precise quantitative assessments of the observational features of FDM and generalised Axion Dark Matter models.

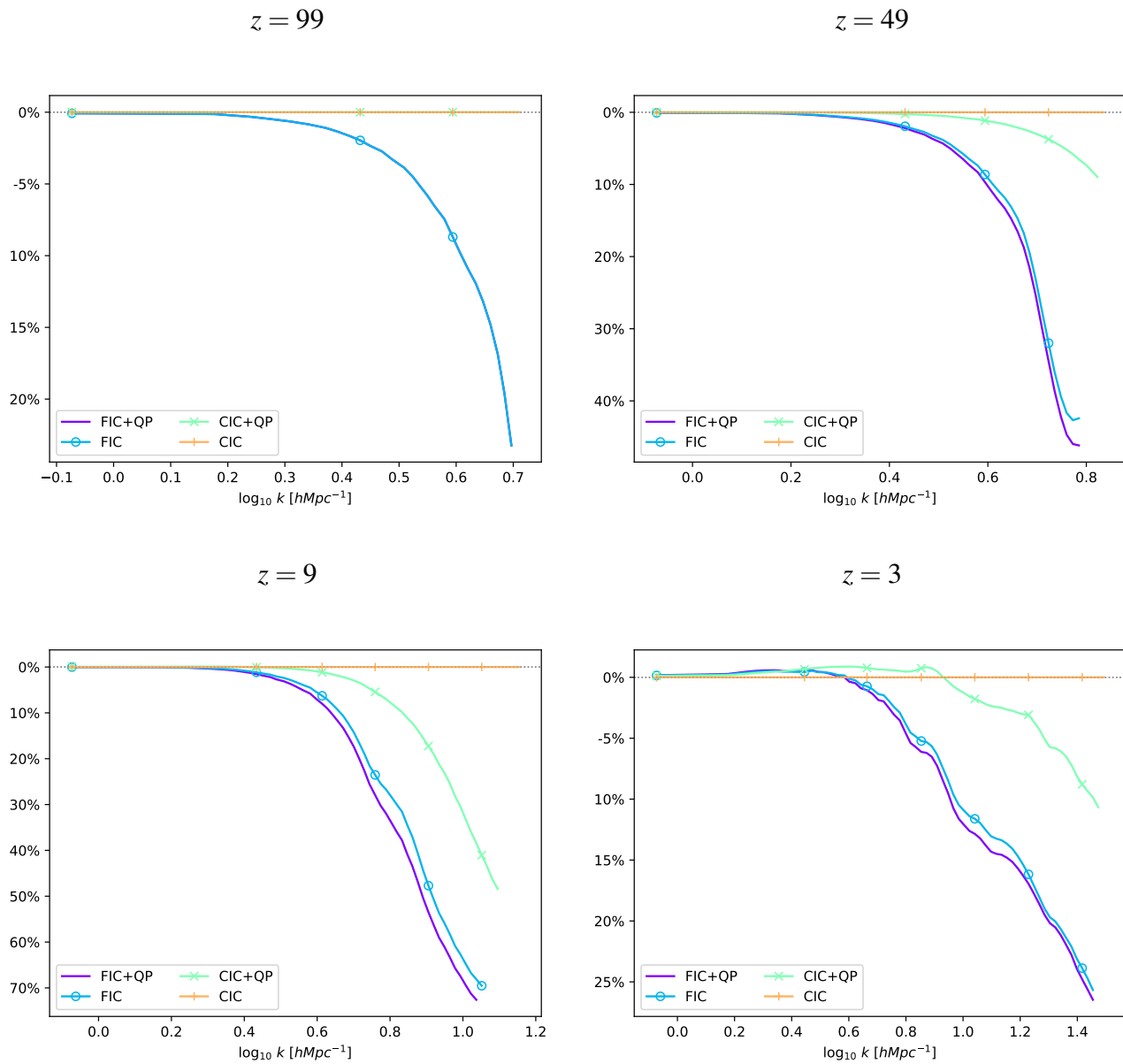


Figure 4.9: Relative difference between matter power spectra between CIC, CIC+QP, FIC and FIC+QP simulations and the reference CIC setup, corresponding to standard Λ CDM.

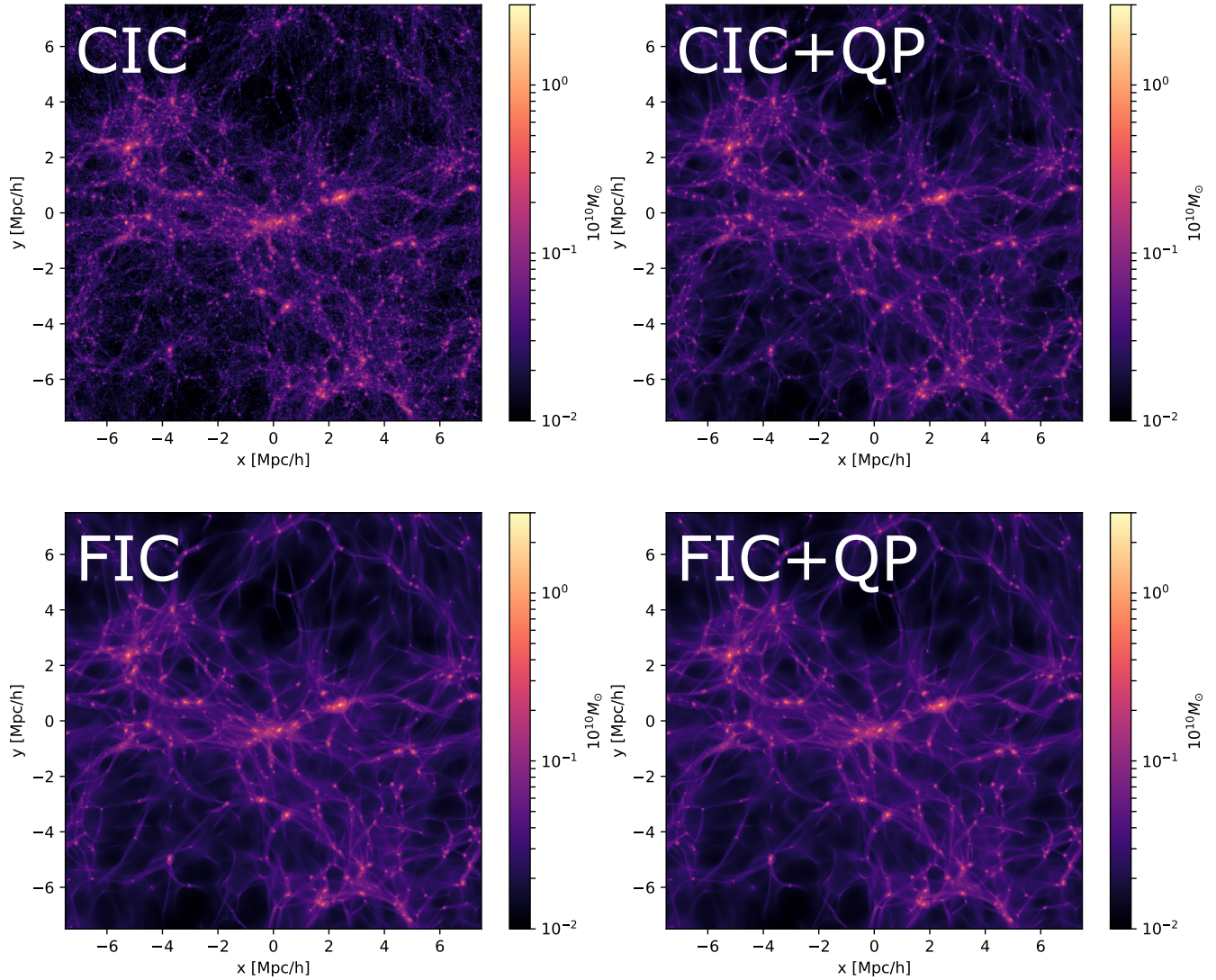


Figure 4.10: Density distribution of four simulations starting from standard initial conditions (*top*) or suppressed with AxionCAMB (*bottom*) and evolved with (*right*) or without (*left*) Quantum Potential effects.

Since the range of action of the QP is characterised by a typical scale $k_Q(z, m)$ (see Eq. 3.9), we do expect that for some range of redshifts and masses the overall linear effect of QP can indeed be accurately encoded in the initial conditions. However, our results suggest that the QP induce a suppression at redshift-dependent scales whose integrated effect cannot be overlooked, at least for scales $\lesssim 1 \text{ Mpc}/h$. Neglecting the QP action in the dynamics may result in an overestimation of power as large as 10% at scales $\approx 300 \text{ kpc}$ at $z = 3$. Therefore, we do conclude that accurate simulations consistently including the QP in the dynamical evolution of cosmic structures are necessary to place fully reliable constraints on the parameter space of FDM and Axion Dark Matter models.

Our results are in stark contrast with the previous findings of [Veltmaat and Niemeyer \(2016\)](#), who found that the matter power spectrum obtained from simulations with suppressed initial conditions (performed with an adaptive mesh refinement code for FDM cosmology) is enhanced at small scales by the action of the QP rather than being further suppressed. Even if the QP can indeed be attractive in small regions of space around overdensities – as discussed in Section 4.2 – we find that the overall integrated effect on the density field is always opposite to gravity – therefore to matter gravitational collapse – thus resulting in a suppression of small-scale power whose intensity may be amplified by using already suppressed initial conditions rather than being overturned by it.

In Fig. 4.10 we provide a visual comparison of the large-scale matter distribution in our four test simulations by showing maps of the density field at redshift $z = 3$ for the four runs. It is evident how most of the low-mass structures that appear in the CIC setup are absent in the other simulations. Both the suppression imprinted in the initial conditions and the one resulting from the QP effect alone are able to wipe out inhomogeneities and prevent dark matter from accrete on small-scale structures, the former being more effective than the latter in this regard. However, the combined effect of suppressed initial conditions and of QP acting on the dynamics of dark matter particles in the simulation FIC+QP – which corresponds to the most realistic and self-consistent setup for FDM – is found to provide the most substantial impact on the abundance of low-mass objects.

4.3.3 Performance

In this Section, we briefly describe the overall performance of AX-GADGET for the cosmological runs described above, and we compare it to a standard CDM simulation performed with the unmodified version of P-GADGET3.

The SPH implementation that computes the QP and its contribution to particle acceleration with three cycles on all the FDM particles has been built analogously to the extremely optimised baryonic one, in order to spread the computation and memory load across the CPUs. Therefore, AX-GADGET should perform in a similar way to a hydrodynamical simulation with no CDM particles. As a consequence, the overhead compared to a collisionless CDM-only simulation is still significant, but definitely much weaker compared to grid-based FDM full-wave solvers (such as e.g. [Schive *et al.*, 2010](#)).

In Fig. 4.11 we show the CPU time and the overhead for the CIC, CIC+QP, FIC and FIC+QP simulations, paired with respect to initial conditions to highlight the additional computational load of the QP computation. Contributions of the routines of gravity solver are presented, along with SPH routines devoted to the bare computation of the density derivatives, the QP acceleration acting on particles and the respective imbalance between CPUs.

As we can see, starting from CDM initial conditions (*top panel*) results in an overhead of a factor of ~ 3 right from the beginning of the simulation in the case when the QP is included. This is due to extra work –needed to compute the QP– arising from the reaction to the non-equilibrium configuration provided in the initial conditions. As one can see from the Figure, this overhead only weakly grows during the remainder of the simulation up to a total factor of ~ 5 at $z = 3$. When FDM initial conditions are used (*bottom panel*), the overburden is indeed less pronounced in the early phases of the evolution whereas the final computational time is a factor ~ 5 larger than the case without QP also in this case.

We find that the major contribution to CPU time is the one associated to the imbalance between CPUs in the SPH calculation –namely *SPH density imbalance* and *SPH acceleration imbalance*–, while the time spent for the bare SPH calculation – *SPH density* and *SPH acceleration* – make up for less than 20% of the total time of the simulation.

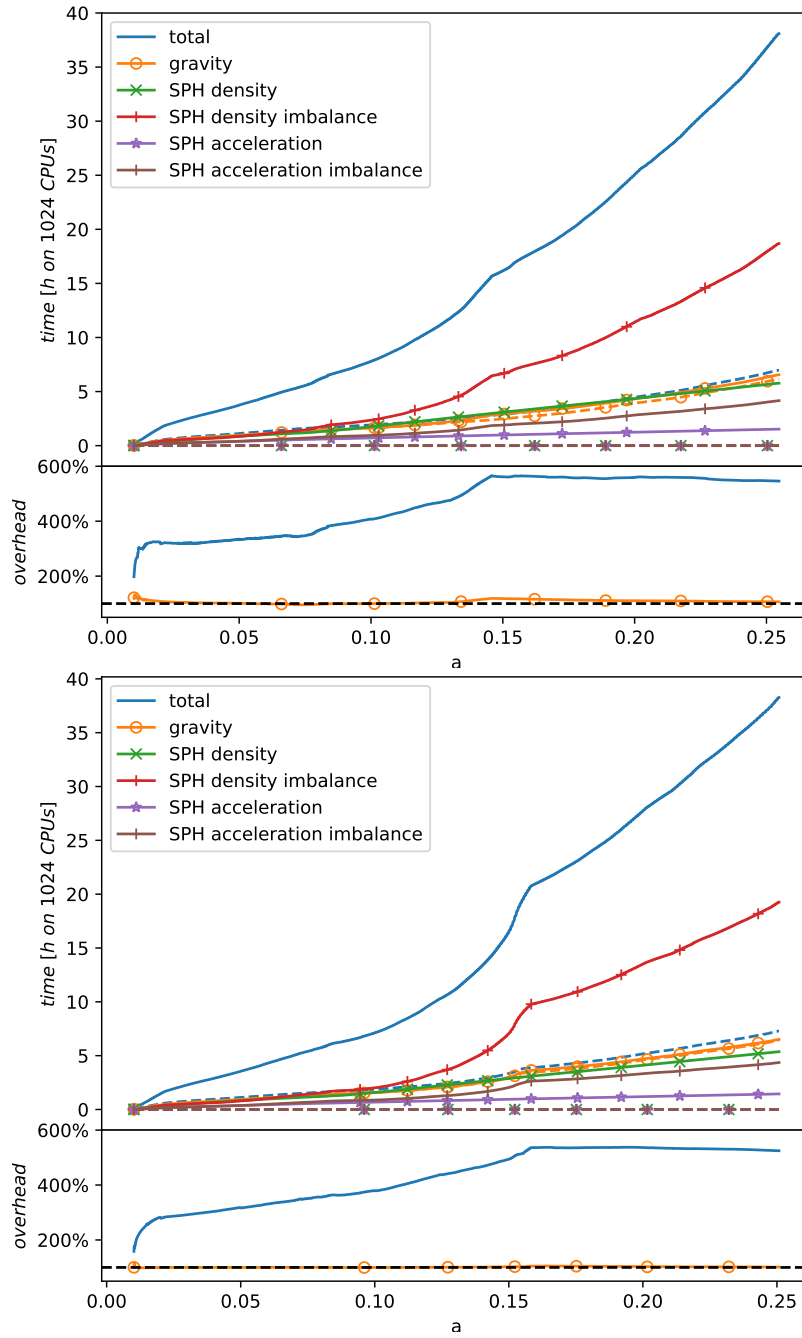


Figure 4.11: CPU time spent as a function of the scale factor a for the simulation with QP (*solid lines*) and without it (*dashed lines*) starting from CDM (*top*) and FDM (*bottom*) initial conditions. The total CPU time is plotted together with the tree-gravity and SPH routines for density and QP acceleration contributions –and relative imbalance between CPUs–. The bottom panels show the overhead for each contribution, as defined by $\text{time}_{\text{solid}}/\text{time}_{\text{dashed}}$.

Therefore, we conclude that given the relatively low overhead obtained for simulations starting from suppressed initial conditions, the inclusion of the QP in the dynamics implemented in AX-GADGET– as would be required from theory – does not affect the performance and the feasibility of large cosmological simulations dramatically while contributing with important physical information.

4.4 Summary of the AX-GADGET implementation

We have presented an extension of the massively parallel N-body code P-GADGET3 for non-linear simulations of Fuzzy and Axion dark matter cosmologies based on the solution of the dynamic Schrödinger equation in the Madelung formulation through Smoothed Particle Hydrodynamics techniques. Our code, that we called AX-GADGET, shares the same general structure of P-GADGET3 thereby inheriting its scalability and load-balance efficiency, as well as the wealth of additional implementations – ranging from sophisticated algorithms for gas physics to Dark Energy (see e.g. Baldi *et al.*, 2010) and Modified Gravity (see e.g. Puchwein *et al.*, 2013) modules – that have been included in P-GADGET3 over the past years.

More specifically, our implementation of Fuzzy Dark Matter is based on the solution of the associated Quantum Potential (see Eq. 3.6) via a series of spatial derivatives of the density field computed from each simulation particle through the standard SPH kernel. Nonetheless, the higher order of spatial derivatives compared to standard SPH simulations that is required to compute the Quantum Potential acceleration (third order derivatives of the density field compared to the first order derivatives required for standard hydrodynamical forces) results in a very poor accuracy of the solver if the standard approach of P-GADGET3 for the computation of spatial gradients is recursively employed. To overcome this problem, we have explored alternative methods to compute higher-order derivatives based on a regularisation of each first-order derivative in regions of constant density (Eq. 4.4).

This improved scheme provides much more accurate and stable results for the computation of the Quantum Potential and its associated acceleration, as we demonstrated through a series of tests for density distributions with a known Quantum Potential analytical solution.

First of all, we investigated a one-dimensional density front described by a hyperbolic tangent shape in a three-dimensional box, realised either by changing the mass of tracer particles set on a regular Cartesian grid or by moving particles of constant mass to reproduce the desired density distribution. In both cases, the standard SPH approach recovers with excellent accuracy the input density, but for the latter it fails in capturing the shape of the associated Quantum Potential faithfully. On the contrary, our improved scheme provides a much more accurate solution thereby giving rise to a better representation of the resulting acceleration.

Secondly, we tested the code on a density distribution that more closely resembles the situation of a collapsing dark matter halo in cosmological simulations, namely a three-dimensional Gaussian density profile, placed at the center of a non-periodic box, again realised both by an individual mass change for a regular grid of particles and by moving around particles of equal mass. Also in this case, the standard SPH approach correctly recovers the input density but fails to reproduce the Quantum Potential accurately for an inhomogeneous distribution of equal mass particles. Again, our improved scheme shows much better convergence to the expected analytical solution. The evolution of a three-dimensional Gaussian density profile in time reveals that our approach is correct also from the dynamical point of view, accurately recovering the formation of the characteristic solitonic core sustained by the QP.

Based on the success of these analytical tests, we moved to apply our algorithm to more realistic cosmological setups. As a first test, we investigated the impact of the Quantum Potential by running two simulations with identical initial conditions, generated for a standard Cold Dark Matter power spectrum, at very high redshift ($z_i = 999$), with and without the contribution of the Quantum Potential. This test showed a sudden re-arrangement of particles right at the start of the simulation when the Quantum Potential is included, resulting in a strong suppression of the density power spectrum at the smallest scales probed by our box compared to the standard case. This is due to having set the system – in the case with Quantum Potential – out of its equilibrium configuration by using a Cold Dark Matter power spectrum to generate the initial conditions. After this first phase of dramatic evolution, however, the system finds its new equilibrium configuration and starts

evolving in a more relaxed way, slowly restoring small-scale perturbations during the cosmological evolution. Most importantly, the evolution is found to recover the theoretically expected linear suppression of the matter power spectrum at intermediate and low redshifts, thereby providing a positive test for the stability and the accuracy of our algorithm.

Then, we moved to compare the impact of the Quantum Potential to the effect of introducing its associated small-scale power suppression in the initial conditions, which has been claimed in the literature to be a sufficient and much cheaper approach to structure formation in Fuzzy Dark Matter cosmologies. To this end, we ran four cosmological simulations starting from a lower initial redshift $z_i = 99$, two of which starting from standard Cold Dark Matter initial conditions, while the other two starting from a random realisation of a suppressed matter power spectrum according to the linear predictions for a given Fuzzy Dark Matter particle mass. For each of these two initial setups, we then evolved the simulations either with or without including the Quantum Potential.

This further test showed that indeed including the Quantum Potential in the dynamics provides a qualitatively similar suppression of the matter power spectrum as one would get from just evolving linearly suppressed initial conditions. However, when both are included in the same simulation – which represents the most consistent setup for the evolution of the system – the resulting matter power spectrum at low redshifts shows an additional suppression of about 5 – 10% compared to the case with no Quantum Potential. This result demonstrates that a proper implementation of the Quantum Potential in the dynamics can be relevant for precision cosmology, and in particular concerning to the more pronounced effects at the level of the structural properties of dark matter halos. Furthermore, one can expect that such additional suppression would result in tighter constraints on the Fuzzy Dark Matter particle mass, that will be discussed in the next Chapter.

Finally, we have shown that the overall performance of AX-GADGET does not make high-resolution cosmological simulations prohibitive, with an overhead compared to standard collisionless simulations of a factor of 5 – 6, thereby having a moderate increase of the computational cost compared to standard SPH simulations.

5

Lyman- α forest constraint and structure characterisation

The Lyman- α forest is the main manifestation of the intergalactic medium (IGM), the diffuse filamentary matter filling the space between galaxies, and it constitutes a very powerful method for constraining the properties of DM in the small-scale $-0.5 \text{ Mpc}/h, \lesssim \lambda \lesssim 20 \text{ Mpc}/h$ – and high redshift $-2 \lesssim z \lesssim 5$ – regime (see e.g. [Viel *et al.*, 2005, 2013a](#)). The physical observable for Lyman- α experiments is the flux power spectrum $P_{\text{F}}(k, z)$ of the photons emitted by Lyman- α bright distant sources as quasars. Constraints on the matter power spectrum from Lyman- α forest data at small cosmological scales are only limited by the thermal cut-off in the flux power spectrum, introduced by pressure and thermal motions of baryons in the photo-ionised IGM. This is why this astrophysical observable has provided some of the tightest constraints to date on DM scenarios featuring a small-scale power suppression ([Boyarisky *et al.*, 2009](#); [Iršič *et al.*, 2017a](#); [Viel *et al.*, 2013b](#); [Iršič *et al.*, 2017b](#);

Murgia *et al.*, 2018), including FDM models, both in the case where they constitute the entire DM (Iršič *et al.*, 2017c; Armengaud *et al.*, 2017), and in the case in which they are a fraction of the total DM amount (Kobayashi *et al.*, 2017).

Ultra-light scalar DM candidates are indeed expected to behave differently with respect to standard CDM on scales of the order of their de Broglie wavelength, where they induce a suppression of the structure formation, due to their wave-like nature. In particular, for FDM particles with masses $\sim 10^{-22}$ eV/ c^2 , such suppression occurs on (sub)galactic scales, being thereby the ideal target for Lyman- α forest observations. Moreover, Lyman- α forest observations probe a redshift and scales range in which the difference between Λ CDM and FDM models – for the masses considered – is highly significant.

All the limits on the properties of FDM presented in Iršič *et al.* (2017c); Armengaud *et al.* (2017); Kobayashi *et al.* (2017) have been computed by assuming that ultra-light scalars behave as standard pressure-less CDM, i.e. by comparing Lyman- α data with flux power spectra obtained from standard SPH cosmological simulations, which completely neglect the QP effects during the non-linear structure evolution. In other words, the non-standard nature of the DM candidate was simply encoded in the suppressed initial conditions used as inputs for performing the hydrodynamical simulations.

One of the main goals of this thesis work is to use AX-GADGET in order to provide the first fully accurate constraints on the FDM mass, by going beyond the standard dynamical approximation of ignoring the time-integrated QP effect. Including such effect in our numerical simulations is thereby expected to tighten the limits published so far in the literature, since it introduces a repulsive effect at small scales throughout the simulation evolution that contributes to the matter power spectrum suppression. Besides presenting the new constraints, we will also carry out a meticulous comparison with the bounds determined under the approximation mentioned above, in order to exactly quantify its validity.

5.1 Simulation suite

In this work, we performed two sets of simulations, for a total number of fourteen cosmological runs. The first set consists in DM-only simulations used to character-

ize the small-scale structures at low redshift – i.e. down to $z = 0 -$, while the second one is evolved to $z = 2$ and includes gas particles and a simplified hydrodynamical treatment, as described in Section 4.1, specifically developed for Lyman- α forest analyses (the so-called *QLYA*, or *Quick-Lyman-alpha* method, see Viel *et al.*, 2004). Both sets consist in three pairs of simulations, one pair for each considered FDM mass, evolved either including or neglecting the effect of the QP in the dynamics – labelling these two cases as *FDM* and *FDMnoQP*, respectively –, in order to assess and quantify the entity of such approximation often employed in the literature. In addition, there is a standard Λ CDM simulation as reference.

Both sets of simulations follow the evolution of 512^3 dark matter particles in a comoving periodic box with side length of 15 Mpc/ h , using 1 kpc/ h as gravitational softening. The mass resolution for the dark-matter-only simulations is $2.2124 \times 10^6 M_\odot$. In all cases we generate initial conditions at $z = 99$ using the 2LPTic code (Crocce *et al.*, 2006), which provides initial conditions for cosmological simulations by displacing particles from a cubic Cartesian grid following a second-order Lagrangian Perturbation Theory based approach, according to a random realisation of the suppressed linear power spectrum as calculated by axionCAMB (Hlozek *et al.*, 2015) for the different FDM masses under investigation. To ensure a consistent comparison between simulations, we used the same random phases to set up the initial conditions. In particular, the FDM masses m_χ considered here are 2.5×10^{-22} , 5×10^{-22} and 2.5×10^{-21} eV/ c^2 , in order to sample the mass range preferred by the first Lyman- α constraints in the literature (see in particular Iršič *et al.*, 2017c; Armengaud *et al.*, 2017; Kobayashi *et al.*, 2017), obtained through N-body simulations with approximated dynamics.

Cosmological parameter used are $\Omega_m = 0.317$, $\Omega_\Lambda = 0.683$, $\Omega_b = 0.0492$ and $H_0 = 67.27$ km/s/Mpc, $A_s = 2.20652 \times 10^{-9}$ and $n_s = 0.9645$. A summary of the simulation specifications can be found in Tab. 5.1.

5.1.1 Lyman- α forest simulations

The Lyman- α flux power spectrum $P_F(k, z)$ is affected both by astrophysical and cosmological parameters. It is, therefore, crucial to accurately quantify their impact in any investigation involving the flux power as a cosmological observable. To this

Table 5.1: Summary of the properties of the simulations set used for structure characterization.

Model	QP in dynamics	m_{22}	N haloes	N genuine haloes	$M_{\text{cut}} [10^{10}M_{\odot}]$
LCDM	×	-	57666	56842	-
FDM-25	✓	25	25051	13387	0.04056
FDM-5	✓	5	10058	2736	0.1645
FDM-2.5	✓	2.5	8504	1301	0.3151
FDMnoQP-25	×	25	25432	13571	0.04056
FDMnoQP-5	×	5	10376	2856	0.1645
FDMnoQP-2.5	×	2.5	8819	1374	0.3151

end, our analysis is based on a set of full hydrodynamical simulations which provide a reliable template of mock flux power spectra to be compared with observations. In particular, the observation performed with the Keck High Resolution Echelle Spectrometer (HIRES) (Vogt *et al.*, 1994), the Magellan Inamori Kyocera Echelle (MIKE) (Bernstein *et al.*, 2002) and the VLT/XSHOOTER (XQ100) (López, S. *et al.*, 2016) are considered.

To take into account the mean Lyman- α forest flux variation, $\bar{F}(z)$, we have explored models up to 20% different than the mean evolution given by Viel *et al.* (2013a). We have varied the thermal history of the IGM in the form of the amplitude T_0 and the slope γ of its temperature-density relation, generally parameterized as $T = T_0(1 + \delta)^{\gamma-1}$, with δ being the IGM over-density (Hui and Gnedin, 1997). We have then considered a set of three different temperatures at mean density, $T_0(z = 4.2) = 7200, 11000, 14800$ K, which evolve with redshift, as well as a set of three values for the slope of the temperature-density relation, $\gamma(z = 4.2) = 1.0, 1.3, 1.5$. The reference thermal history has been chosen to be defined by $T_0(z = 4.2) = 11000$ and $\gamma(z = 4.2) = 1.5$, providing a good fit to observations (Bolton *et al.*, 2017). Following the conservative approach of Iršič *et al.* (2017c), we have modelled the redshift evolution of γ as a power law

$$\gamma(z) = \gamma^A [(1+z)/(1+z_p)]^{\gamma^S} \quad (5.1)$$

where γ^A and γ^S are free parameters describing the amplitude and exponent of the power law, respectively. The pivot redshift z_p is the one at which most of the Lyman- α forest pixels are coming from – i.e. at $z_p = 4.2$ for MIKE/HIRES+XQ-100 –. However, in order to be agnostic about the thermal history evolution, we let the amplitude $T_0(z)$ free to vary in each redshift bin, only forbidding differences greater than 5000 K between adjacent bins (Iršič *et al.*, 2017a).

Furthermore, we have also explored several values for the cosmological parameters σ_8 , i.e. the normalisation of the matter power spectrum, and n_{eff} , namely the slope of the matter power spectrum at the scale of Lyman- α forest (0.009 s/km), in order to account for the effect on the matter power spectrum due to changes in its initial slope and amplitude (Seljak *et al.*, 2006; McDonald *et al.*, 2006; Arinyo-i Prats *et al.*, 2015). We have therefore considered five different values for σ_8 (in the interval [0.754, 0.904]) and n_{eff} (in the range [−2.3474, −2.2674]).

We have also varied the re-ionization redshift z_{rei} , for which we have considered the three different values $z_{\text{rei}} = 7, 9, 15$, with $z_{\text{rei}} = 9$ being the reference value and, finally, we have considered ultraviolet (UV) fluctuations of the ionizing background, that may have non-negligible effects at high redshift. The amplitude of this phenomenon is parameterised by the parameter f_{UV} : the corresponding template is built from a set of three models with $f_{\text{UV}} = 0, 0.5, 1$, where $f_{\text{UV}} = 0$ is associated with a spatially uniform UV background.

Based on such grid of simulations, we have performed a linear interpolation between the grid points in such multidimensional parameter space, to obtain predictions of flux power for the desired models.

We have to note that the thermal history implementation of the grid of simulations presented in Iršič *et al.* (2017c) are slightly different from the one used in the simulations described in the previous Section. For this reason, since those simulations were performed without the introduction of the QP in the dynamics, we mapped our results into the grid of simulations of Iršič *et al.* (2017c) using the ratio between FDM and FDMnoQP simulations. This is, of course, not an exact procedure but we assume that the ratio of flux power spectrum with and without quantum potential is relatively insensitive to the thermal history (Murgia *et al.*, 2018).

In order to constrain the various parameters, we have used a dataset given by

the combination of intermediate and high-resolution Lyman- α forest data from the XQ-100 and the HIRES/MIKE samples of QSO spectra, respectively. The XQ-100 data are constituted by a sample of medium resolution and intermediate signal-to-noise QSO spectra, obtained by the XQ-100 survey, with emission redshifts $3.5 \leq z \leq 4.5$ (López, S. *et al.*, 2016). The spectral resolution of the X-shooter spectrograph is $30 - 50 \text{ km/s}$, depending on the wavelength. The flux power spectrum $P_F(k, z)$ has been calculated for a total of 133 (k, z) data points in the ranges $z = 3, 3.2, 3.4, 3.6, 3.8, 4, 4.2$ and 19 bins in k -space in the range $0.003 - 0.057 \text{ s/km}$ (see Iršič *et al.*, 2017b, for a more detailed description). MIKE/HIRES data are instead obtained with the HIRES/KECK and the MIKE/Magellan spectrographs, at redshift bins $z = 4.2, 4.6, 5.0, 5.4$ and in 10 k -bins in the interval $0.001 - 0.08 \text{ s/km}$, with spectral resolution of 13.6 and 6.7 km/s, for HIRES and MIKE, respectively (Viel *et al.*, 2013a). As in the analyses by Viel *et al.* (2013a) and Iršič *et al.* (2017a), we have imposed a conservative cut on the flux power spectra obtained from MIKE/HIRES data, and only the measurements with $k > 0.005 \text{ s/km}$ have been used, in order to avoid possible systematic uncertainties on large scales due to continuum fitting. Furthermore, we do not consider the highest redshift bin for MIKE data, for which the error bars on the flux power spectra are very large (see Viel *et al.*, 2013a, for more details). We have thus used a total of 182 (k, z) data points. Parameter constraints are finally obtained with a Monte Carlo Markov Chain (MCMC) sampler which samples the likelihood space until convergence is reached.

5.2 Matter and Lyman- α power spectrum

In this Section, we present the results obtained from our simulations in decreasing order of scale involved, starting from the matter power spectrum, to the simulated Lyman- α forest observations, to the statistical characterisation of halo properties and their density profiles.

5.2.1 Matter Power spectrum

The relative difference of the matter power spectrum of the various FDM models with respect to Λ CDM at four different redshifts is displayed in Fig. 5.1.

As already found in the literature (see e.g. Marsh, 2016b; Nori and Baldi, 2018),

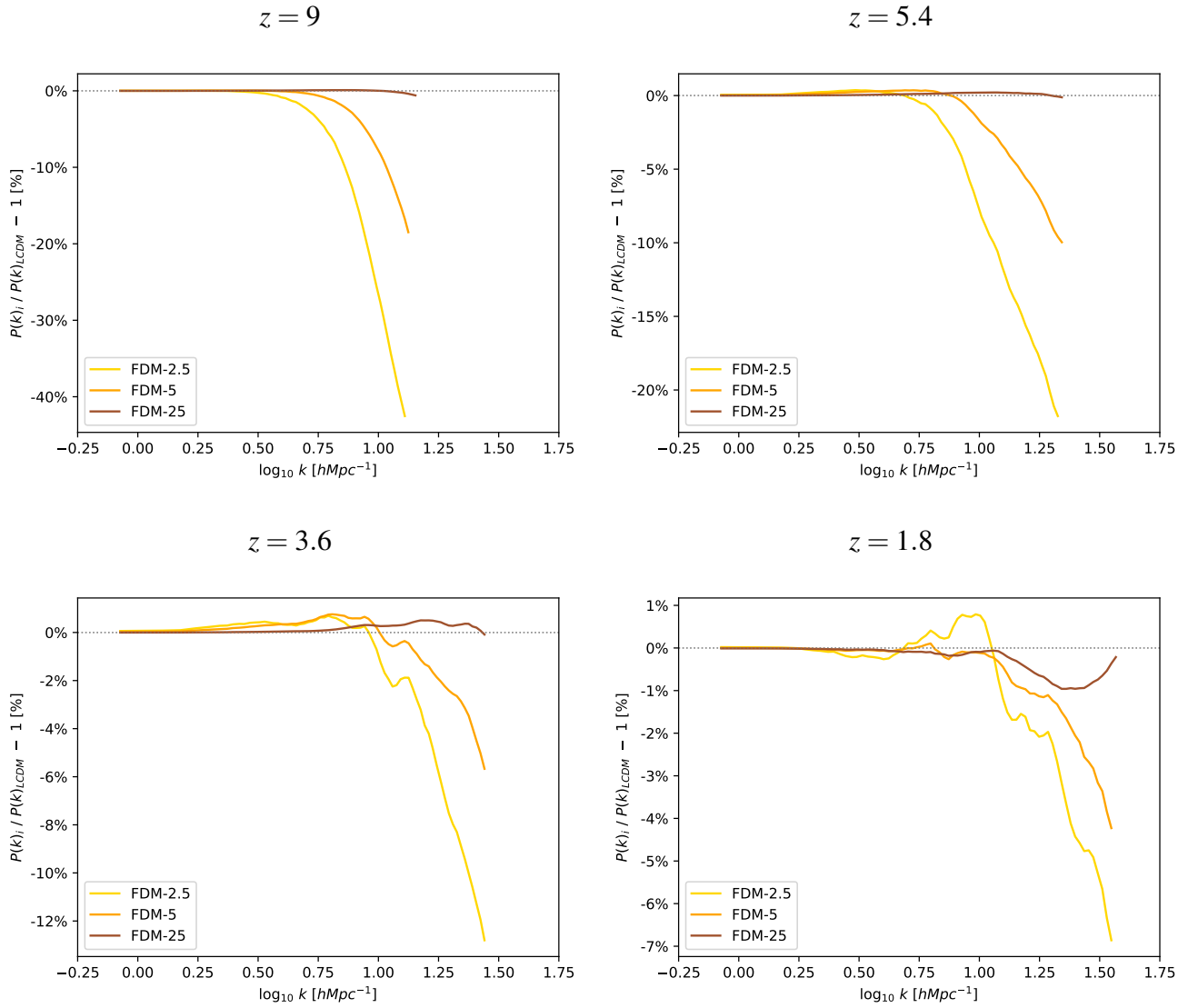


Figure 5.1: Matter power spectrum of FDM models contrasted with Λ CDM at different redshifts.

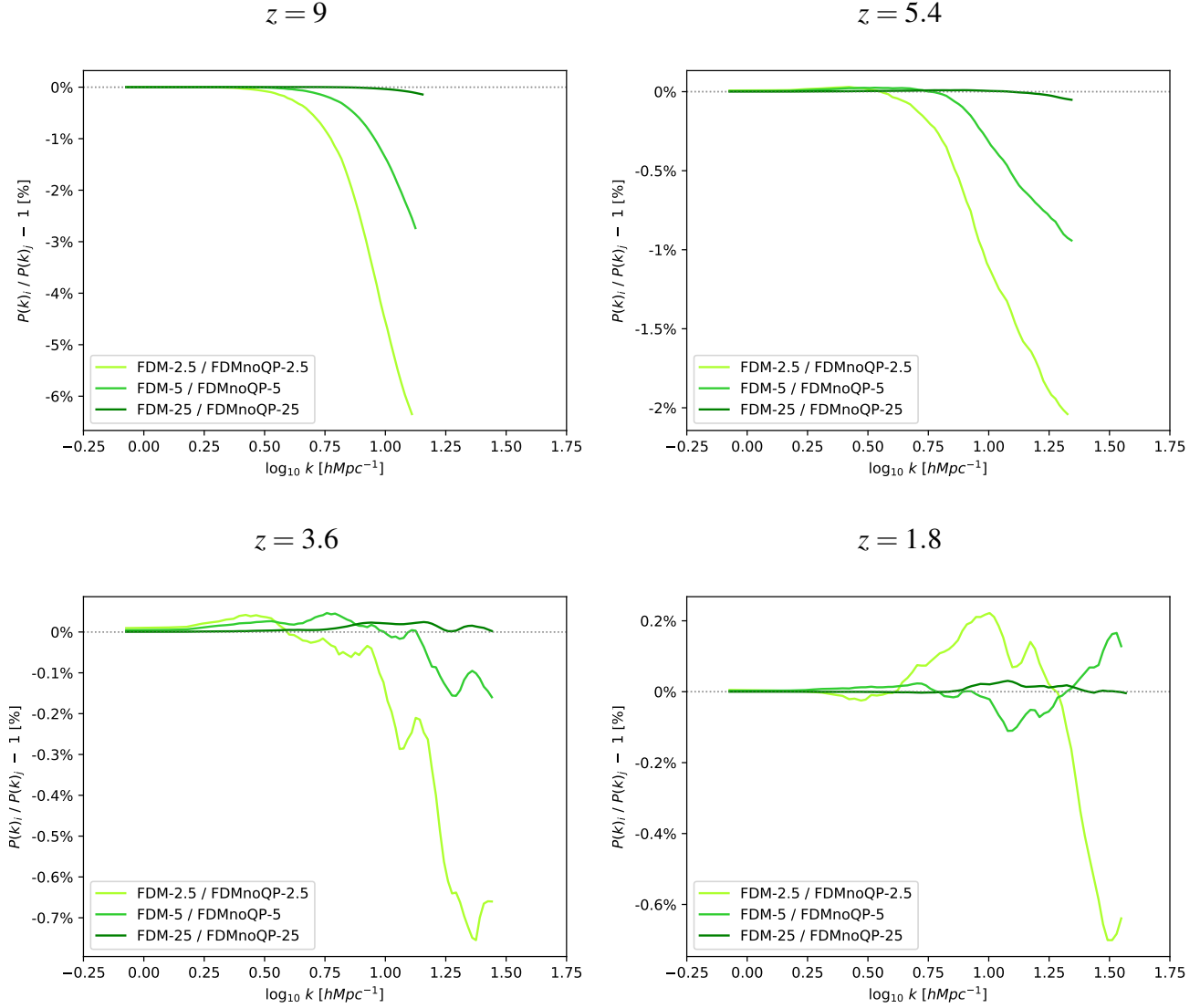


Figure 5.2: Matter power spectrum percentage differences between FDM simulation and their FDMnoQP counterpart at different redshifts. The difference in power spectrum suppression of having the QP in the dynamics result in a multiplication of $\sim 115\%$ factor of the suppression with respect to LCDM of Fig. 5.1 at scales $k \sim 10 h\text{Mpc}^{-1}$.

the evolution of the matter power spectrum shows that the initial suppression – encoded in the transfer functions used to build up the initial conditions – is restored at intermediate scales to the unsuppressed level, eventually, by the non-linear gravitational evolution.

At the redshifts and scales that are relevant for Lyman- α forest observations, however, the relative suppression with respect to Λ CDM is still important and ranges from 5 – 20% for the lowest FDM mass considered.

The relative difference of the matter power spectrum, displayed in Fig. 5.2, shows an additional suppression with respect Λ CDM – by a factor ≈ 1.15 – when the QP is included in the dynamical evolution (i.e. in the comparison between the FDM and the FDMnoQP simulations). This is consistent with the QP full dynamical treatment contributing as an integrated smoothing force that contrasts the gravitational collapse of the otherwise purely collisionless dynamics.

5.2.2 Lyman- α forest flux statistics

In order to build our simulated Lyman- α observations, we extracted 5000 mock forest spectra from random line-of-sights within the simulated volume. The spectra are extracted according to SPH interpolation, and the ingredients necessary to build up the transmitted flux are the HI-weighted peculiar velocity, temperature and neutral fraction. Among the different flux statistics that can be considered, we focus on the flux probability distribution function (PDF) and flux power spectrum. Unless otherwise stated we normalise the extracted flux arrays in order to have the same observed mean flux over the whole sample considered and for all the simulations. In any case, we do find that the scaling factor for the optical depth arrays over the whole simulated volume is 1.6, 1.4 and 1.1 times higher than in the Λ CDM case in order to achieve the same mean flux for the $m_{22} = 2.5, 5$ and 25 FDM cases with negligible – between 1 – 2% – differences between the FDMs and FDMnoQP cases.

In Fig. 5.3 we show the flux (*left panel*) and gas (*right panel*) PDF ratios between the simulations that include the QP and those that do not include it – FDM and FDMnoQP, respectively – at $z = 5.4$, one of the highest redshift bins in which Lyman- α data are available.

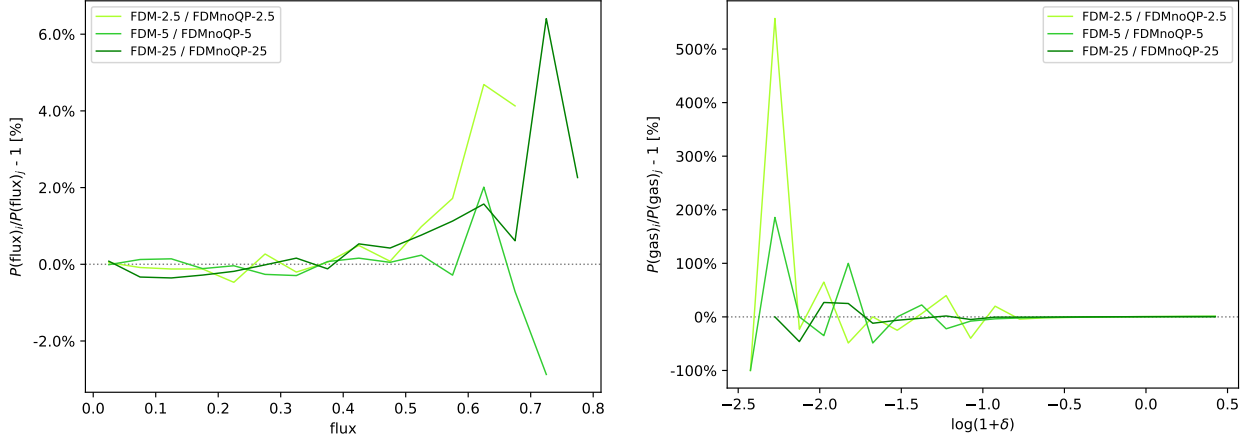
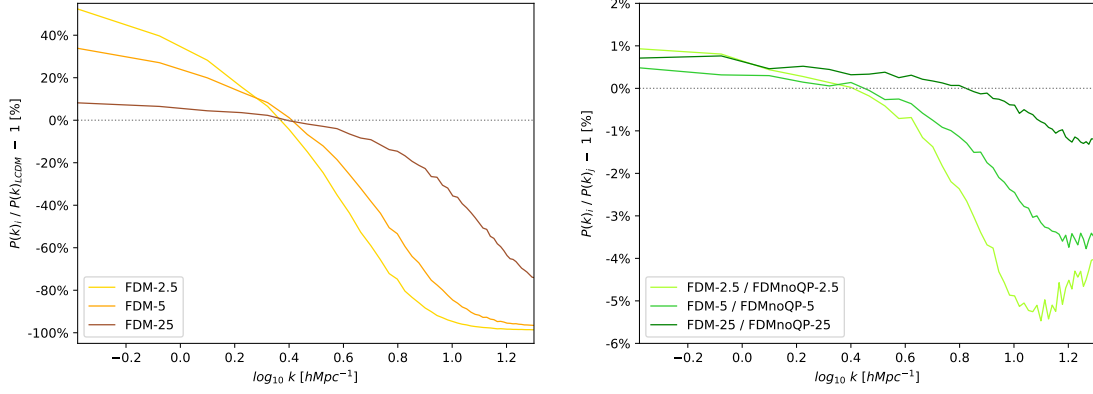


Figure 5.3: Relative differences of the flux PDF (*left panel*) and gas PDF (*right panel*) for FDM models with respect to their corresponding FDMnoQP counterparts, at redshift $z = 5.4$.

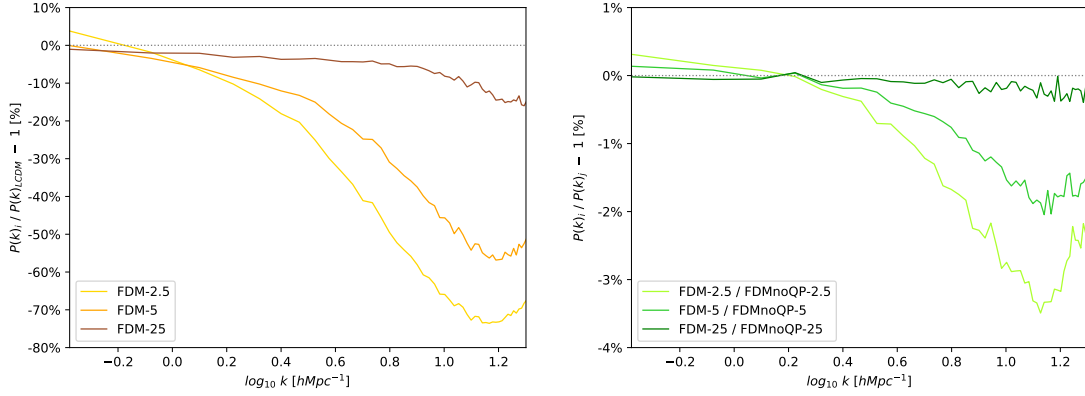
It is possible to see that there is a 2 – 6% peak at flux $\sim 0.6 – 0.8$, i.e. in regions of low transmissivity that are expected to trace voids. The fact that FDM simulations display a more peaked PDF compared to FDMnoQP ones for this range of fluxes means that in those models, on average, it is more likely to sample such void environments. In fact, the different PDFs should reflect the underlying different gas PDFs at the same redshifts and along the same lines-of-sight. In the bottom panel of Fig. 5.3, showing the corresponding gas PDF, it is indeed apparent that in models with FDMs the gas PDF is more skewed towards less dense regions, that are typically associated to high transmission. The effect due to the QP is thus to increase the volume filling factor of regions below the mean density with respect to the corresponding FDMnoQP case.

In Fig. 5.4 we plot the percentage difference in terms of flux power spectrum at three different redshifts and for the three FDM models, both compared to Λ CDM (*right panels*) and to the corresponding FDMnoQP case (*left panels*). The increase of power at $z = 5.4$ in the largest scales – compared to the Λ CDM case – is due to the imposed normalisation at the same mean flux, while the evident suppression at small scales is related to the lack of structures at those scales. The comparison with the FDMnoQP set-ups, instead, reveals an additional suppression which is always

$z = 5.4$



$z = 4.0$



$z = 3.0$

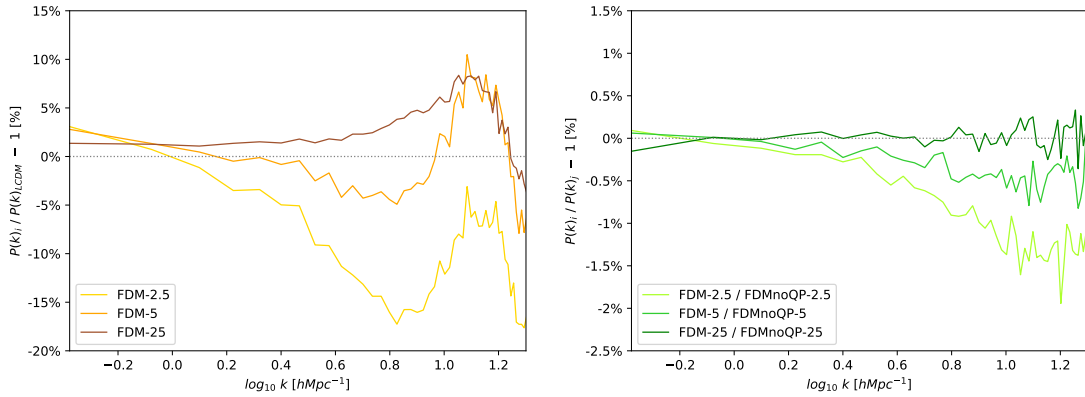


Figure 5.4: Flux power spectrum comparison between all simulations and LCDM (*left panels*), and between FDM simulation and their FDMnoQP counterparts (*right panels*) at different redshifts.

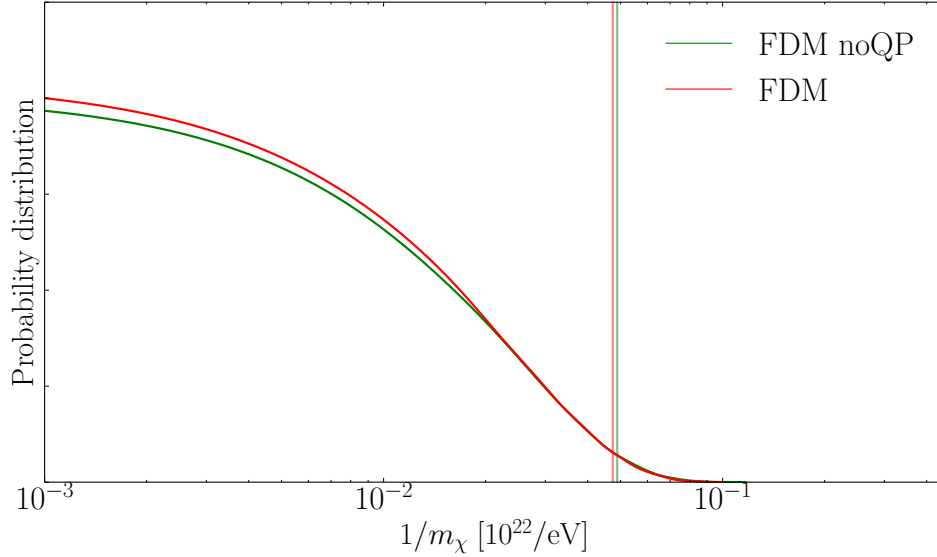


Figure 5.5: Here we plot the marginalised posterior distribution of $1/m_\chi$ from both the analyses performed by [Iršič *et al.* \(2017c\)](#) (green lines, without QP) and ours (red lines, with QP). The vertical lines stand for the 2σ C.L. limits.

below the 5% level for all the masses considered. Since the flux power spectrum is an exponentially suppressed proxy of the underlying density field, these results are consistent with the matter power spectrum results previously shown in Fig. 5.1 and Fig. 5.2.

Since the Lyman- α constraints are calculated by weighting the contribution from all the scales, we expect the bound on m_{22} found in [Iršič *et al.* \(2017c\)](#) to change accordingly to the additional suppression introduced, that in our case is 2 – 3%.

This is exactly what can be seen in Fig. 5.5, where the marginalised posterior distribution of m_χ obtained in the present work is plotted and compared with the results presented in [Iršič *et al.* \(2017c\)](#). The red line refers to our MCMC analysis, whereas the green line corresponds to the results obtained by [Iršič *et al.* \(2017c\)](#). The corresponding vertical lines show the 2σ bounds on the FDM mass. The 2σ bound on the FDM mass changes from $20.45 \times 10^{-22} \text{eV}/c^2$ to $21.08 \times 10^{-22} \text{eV}/c^2$, which matches with our expectation and confirm that the approximation of neglecting the QP dynamical effects in [Iršič *et al.* \(2017c\)](#) was legitimate to investigate

the Lyman- α typical scales. The agreement between the sets of results obtained with and without the dynamical QP implementation is evident and is not sensibly affected by varying the assumptions on the IGM thermal history.

This result represents – to our knowledge – the first FDM mass constraint derived from Lyman- α forest observations that accounts for the full non-linear treatment of the QP, which introduces an additional – albeit not big – suppression of the matter power spectrum in the redshift range and comoving scales probed by the Lyman- α forest. The agreement with previous results implies that the non-linear evolution of the large-scale structure and the non-linear mapping between flux and density effectively make up for the additional suppression introduced.

5.3 Structure characterization

For cosmological models whose LSS properties depart sensibly from Λ CDM only at small scales – as FDM models – , the thorough analysis of the overall statistical properties and the specific inner structures of haloes represents the most relevant and often largely unexploited source of information. In N-body simulations, this implies the use of a suitable clustering algorithm to build a halo catalogue in order to identify gravitationally bound structures that can then be studied in their inner structural properties.

In this work, we rely on the SUBFIND routine already implemented in P-GADGET3, a two-step halo-finder which combines a Friends-Of-Friends (FoF) algorithm (Davis *et al.*, 1985) to find particle clusters – that defines the primary structures of our halo sample – with an unbinding procedure to identify gravitationally bound substructures within the primary haloes (Springel *et al.*, 2001). Hereafter, we use the terms *primary structures* to identify the substructures of each FoF group containing the most gravitationally bound particle, *subhaloes* for the non-primary structures and *haloes* when we generally consider the whole collection of structures found – i.e. including both primary structures and subhaloes –.

5.3.1 Numerical Fragmentation

A long-standing problem that affects N-body simulations, when characterised by a sharp and resolved cut-off of the matter power spectrum, has to be taken into

account in the process of building a reliable halo sample. This is the so-called *numerical fragmentation*, i.e. the formation of artificial small-mass spurious clumps within filaments (see e.g. Wang and White, 2007; Schneider *et al.*, 2012; Lovell *et al.*, 2014; Angulo *et al.*, 2013; Schive *et al.*, 2016).

While it has been initially debated whether the nature of such fragmentation was to be considered physical or numerical, the detailed analysis by Wang and White (2007) showed that in Warm and Hot Dark Matter simulations (as e.g. Bode *et al.*, 2001b) – which are characterised by a highly suppressed matter power spectrum – the formation of small mass subhaloes was resolution dependent and related to the significant difference between force resolution and mean particle separation (as already suggested by Melott and Shandarin, 1989).

To identify spurious haloes in simulations and select a clean sample to study and characterize the structures of FDM haloes in each simulation, we take cue from the procedure outlined in Lovell *et al.* (2014): in particular, we use the mass at low redshift and the spatial distribution of particles as traced back in the initial conditions as proxies for the artificial nature of haloes as described below.

In fact, the more the initial power spectrum is suppressed at small scales, the more neighbouring particles are coherently homogeneously distributed, thus facilitating the onset of artificially bounded and small ensembles that eventually outnumber the physical ones. As already shown by Wang and White (2007), the dimensionless power spectrum peak scale k_{peak} and the resolution of the simulation – i.e. described through the mean inter-particle distance d – can be related together to get the empirical estimate

$$M_{lim} = 10.1 \rho_b d / k_{peak}^2 \quad (5.2)$$

describing the mass at which most of the haloes have a numerical rather than a physical origin. In Lovell *et al.* (2014), this mass is used as a pivotal value for the mass M_{CUT} used to discriminate genuine and spurious haloes – lying above and below such threshold, respectively – which is set as $M_{CUT} = 0.5M_{lim}$.

In addition to the mass discriminating criterion, Lovell *et al.* (2014) showed that particles that generate spurious haloes belong to degenerate regions in the initial

conditions and are more likely to lie within filaments, stating that the reconstructed shape of the halo particles ensemble in the initial conditions can be used to identify spurious structures. N-Body initial conditions are generally designed as regularly distributed particles on a grid from which are displaced in order to match the desired initial power spectrum. Hence, numerical fragmentation originates mostly from particles lying in small planar configurations, belonging to the same row/column domain or a few adjacent ones.

Therefore, we need a method to quantitatively describe the shape of subhaloes and the distribution of their member particles once traced back to the initial conditions of the simulation. To this end, we resort to the inertia tensor of the particle ensemble

$$I_{ij} = \sum_{particles} m (\hat{e}_i \cdot \hat{e}_j) |r|^2 - (\vec{r} \cdot \hat{e}_i) (\vec{r} \cdot \hat{e}_j) \quad (5.3)$$

where m and \vec{r} are the particle mass and position respectively, and \hat{e} are the unit vectors of the reference orthonormal base. The eigenvalues and the eigenvectors of the inertia tensor represent the square moduli and unitary vectors of the three axes of the equivalent triaxial ellipsoid with uniform mass distribution. We define $a \geq b \geq c$ the moduli of the three axes and the sphericity $s = c/a$ as the ratio between the minor and the major ones: a very low sphericity will characterise the typical degenerate domains of numerical fragmentation.

For these reasons, we use the combined information carried by the mass and the sphericity in the initial condition to clean the halo catalogues from spurious ones by applying independent cuts on both quantities as will be detailed below.

In Fig. 5.6 the mass-sphericity distributions of the different simulations are plotted at $z = 0$ (*upper left panel*) and at $z = 99$ (*upper right panel*) where each point represents a halo identified by SUBFIND, without applying any selection. Solid and dash-dotted lines denote the median and the 99th percentile of the distribution; in the side panels, we display the cumulative distributions, where the contribution of spurious haloes – identified with the procedure that we detail below – is highlighted in black.

By looking at the two panels, it is possible to notice that the total cumulative sphericity distribution at low redshift is fairly model independent, so that distin-

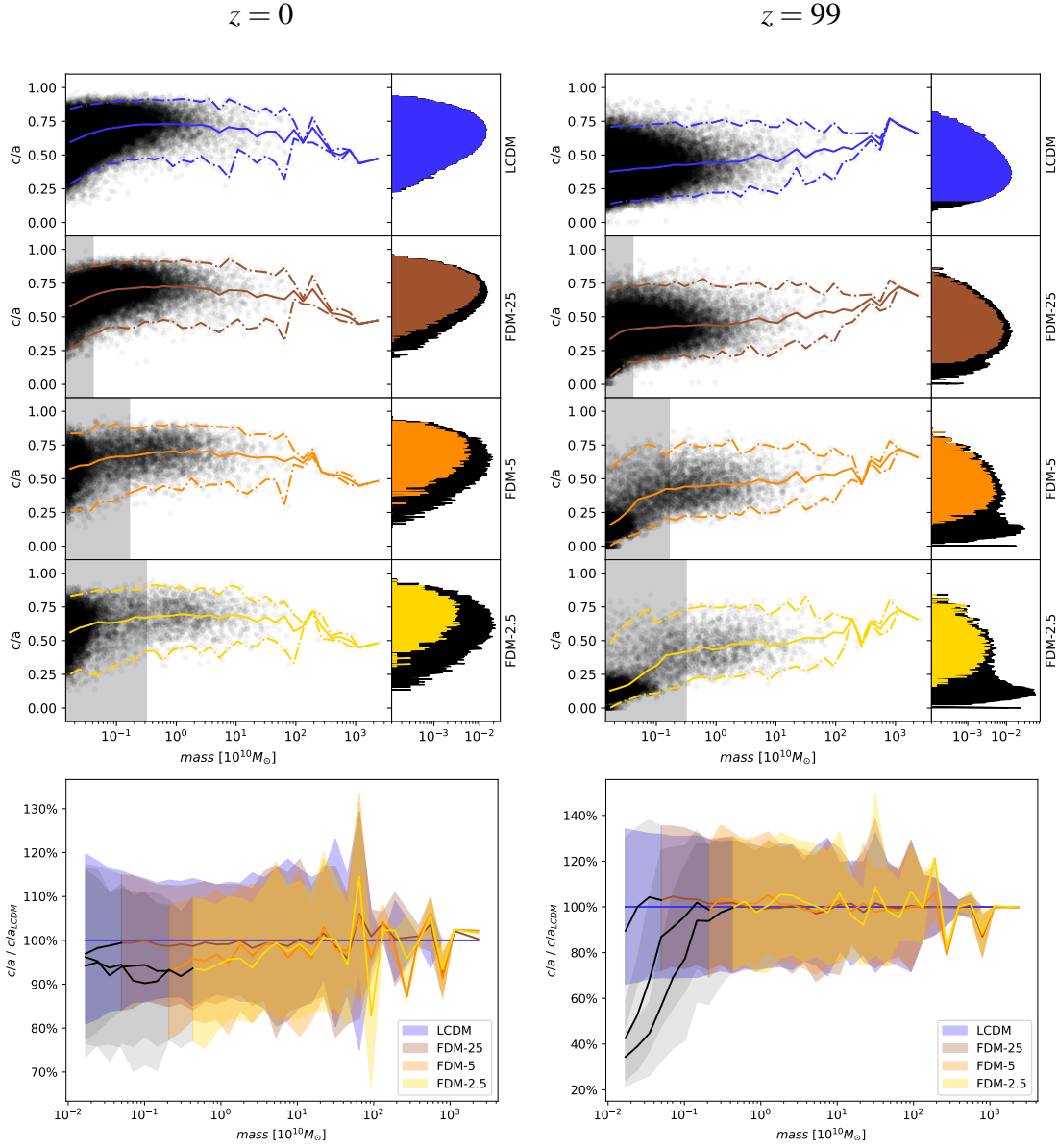


Figure 5.6: Sphericities of haloes (black-dots) found by SUBFIND as function of their mass (*upper panels*) at redshifts $z = 0$ and $z = 99$ (*left and right panels*, respectively). The grey-shaded areas represent the discarded region below the specific mass cut M_{CUT} of each model. The solid (dot-dashed) lines describe the median (99th percentile) of the total distribution, which are all gathered and contrasted with Λ CDM in the lower panels. The total sphericity distribution integrated in mass is represented in the side panels with the discarded sample contribution portrayed in black. *Lower panels* feature the median of the mass-sphericity distributions contrasted with Λ CDM. The shaded areas, corresponding to the $\pm 1\sigma$ of the distribution, are colour-coded as in the upper panels. The blackened median and grey-shaded areas represent the excluded portion below M_{CUT} .

guishing spurious haloes from genuine ones is impossible. However, if we trace the particle ensembles of each halo found at $z = 0$ back to the initial conditions at redshift $z = 99$, using particles ID, and we study the resulting reconstructed mass-sphericity relation, the anomalous component of the distribution associated with spurious haloes clearly emerges as a low-sphericity peak, which is more pronounced for smaller values of the FDM particle mass.

In fact, when the mass m_χ decreases, the smoothing action of the QP becomes more efficient, inducing homogeneity at larger and larger scales in the initial conditions and increasing, consequently, the contamination of numerical fragmentation. It clearly appears that the population of haloes in the initial conditions is homogeneously distributed in Λ CDM while a bimodal structure emerges at lower and lower FDM mass. In particular, an increasing number of haloes are located in a small region characterized by low mass ($M \lesssim 10^9 M_\odot$) and low sphericity ($s \lesssim 0.20$).

As there is no theoretical reason why the QP should favour the collapse of ensembles with very low sphericities in the initial conditions with respect to the Λ CDM case, we consider this second population as the result of numerical fragmentation.

As in Lovell *et al.* (2014), we choose to compute $M_{CUT} = 0.5M_{lim}$ using Eq. 5.2 – one M_{CUT} for each value of the FDM mass, as reported in Tab. 5.1 –, that define the upper bound of the discarded mass regions, i.e. the grey-shaded areas in all panels of Fig. 5.6.

It is interesting to notice that the masses M_{CUT} appear to be very close to the values at which the sphericity medians of the simulation sample – in the initial conditions – depart from the ones of Λ CDM, as can be seen in the *lower-right* panel of Fig. 5.6. As the M_{CUT} values we obtain are slightly larger compared to these departing values, we confirm the choice of the former over the latter, as a more conservative option for the mass thresholds dividing spurious from genuine haloes.

In Lovell *et al.* (2014), the selection in terms of initial sphericity was operationally performed discarding every halo with sphericity lower than $s_{CUT} = 0.16$, equal to the 99th percentile of the distribution of haloes with more than 100 particles in the Λ CDM simulation. In our set of simulations, a similar value denotes the 99th percentile as measured at the M_{CUT} mass in each simulation, so we adopt it as our own threshold in sphericity. Let us stress that the haloes that are discarded through

Table 5.2: The total and genuine number of haloes, presented as the ratio between the simulations neglecting and considering the QP dynamical effects.

m_{22}	N haloes	N genuine haloes
25	101.6%	101.4%
5	103.5%	104.4%
2.5	103.1%	105.6%

sphericity selection in the initial conditions have sphericities at $z = 0$ that are statistically consistent with the genuine sample, making their numerical origin impossible to notice based only on the sphericity distribution at $z = 0$. However, the mass constraint is far more rigid than the sphericity one in all models but Λ CDM, where no mass limit is imposed.

Finally, in Tab. 5.2 we have summarised the comparison of the number of haloes in the FDMnoQP set-up with respect to the corresponding FDM set-up, presented as the ratio of the total number of haloes found by SUBFIND and the number of genuine haloes remaining after the exclusion of spurious ones. It is possible to see that in the FDMnoQP simulations, for the three FDM masses considered, the total number of haloes is overestimated by a factor $\sim 2.5\%$ on average while the genuine haloes excess becomes more important as the FDM mass decreases, up to 5.6% for $m_{22} = 2.5$. This means that neglecting the effects of the QP during the simulation leads to the formation of haloes which are not present when the full QP dynamics is taken into account and that, using our *à la* Lovell *et al.* (2014) spurious detection selection, such haloes pass the numerical fragmentation test and contaminate any halo statistical property characterization.

5.3.2 Inter-simulations halo matching

In FDM models, as we said in the previous Sections, not only the initial power spectrum of matter perturbation is suppressed at small scales, thereby preventing the formation of small mass structures, but the dynamical evolution of density perturbations changes due to the effect of the QP, intimately affecting the development of structures during the whole cosmological evolution by opposing gravitational col-

lapse. The implementation of such effect in AX-GADGET breaks the one-to-one correspondence of the spatial position of collapsed structures in simulations with different FDM masses – especially for smaller objects –, despite the same random phases used to set up the initial conditions.

We indeed expect bigger haloes not to change their position dramatically at low redshift across different simulation, while this is not the case for lighter subhaloes which are more affected by the evolving local non-linear balance between gravity and the QP of the environment.

This makes it more difficult to identify matching collapsed objects of common origin across the simulations, to study how FDM models affect the inner structure of haloes on a halo-to-halo basis.

To this end, we devise an iterative matching procedure, to be repeated until no more couples are found, as the following: given a halo i at position \vec{r}_i and total mass m_i in simulation A ,

- i. select all haloes j belonging to simulation B as potential counterparts if

$$|\vec{r}_i - \vec{r}_j| / (a_i + a_j) < \tilde{R} \quad (5.4)$$

where a_i and a_j are the major axes of the haloes computed through the inertia tensor of all their member particles.

- ii. within the ensemble selected at the previous point, retain only the haloes $k \subseteq j$ whose masses satisfy the condition

$$|m_i - m_k| / (m_i + m_k) < \tilde{M} \quad (5.5)$$

- iii. if more than one halo $l \subseteq k$ is left, then choose the one for which

$$|\vec{r}_i - \vec{r}_l| / (a_i + a_l) \quad (5.6)$$

is minimum.

- iv. after having considered all the haloes in A , if more than one are linked to the

same halo l belonging to B , choose the couple (i, l) that minimizes

$$[|\vec{r}_i - \vec{r}_l|/(a_i + a_l)]^2 + [|m_i - m_l|/(m_i + m_l)]^2 \quad (5.7)$$

in order give the same weight to the two criteria.

This method is flexible enough to account for the shift in mass and position we expect from simulations with different FDM mass models, but conservative enough to ensure the common origin of the subhalo couples. Moreover, using the combination of position and mass filters, we are able to discriminate couples in all mass ranges: position filtering is a weaker constraint in the case of bigger haloes – since they occupy a large volume – while the mass filter is very strict; vice-versa, the former criterion is more powerful for smaller haloes for which the mass filter select a large number of candidates.

Operatively, we use the previous procedure to match haloes in each simulation with the Λ CDM one, and we refer to the subset of haloes that share the same Λ CDM companion across all the simulations as the *common* sample.

For geometrical reasons, we set the limit value for \tilde{R} to be 0.5: this represents the case in which two haloes with the same major axis a have centres separated exactly by the same amount a . The configurations that are selected by point (i) are the ones for which the distance between the halo centres is less or equal the smallest major axis between the two. A higher value for \tilde{R} would include genuine small haloes that have been more subject to dynamical QP drifting but would also result in a spurious match of bigger haloes. For these reasons, we adopt $\tilde{R} = 0.5$, checking that the selected sample gains or loses $\sim 5\%$ of components if values 0.45 and 0.55 are used, without modifying the overall statistical properties of the sample itself.

With respect to \tilde{M} at point (ii) , instead, we applied the matching algorithm using several values, each denoting a specific threshold of the minimum value allowed for the mass ratio of halo couples in order to be considered as a match. As reported in Tab. 5.3, more than 60% of all the matching haloes across LCDM and FDMs simulations without mass selection – $\tilde{M} = 1$ case – have a mass ratio in the 100 – 85% ratio range and almost 80% in the 100 – 75% range. In order not to spoil our

Table 5.3: Number of common matches across LCDM and FDMs simulations, using different values of the parameter \tilde{M} representing the minimum allowed ratio between the minimum and maximum masses of each candidate couple.

\tilde{M}	m_{min}/m_{max}	N matches
1/39	95%	53
1/19	90%	162
3/37	85%	234
1/9	80%	279
1/7	75%	304
1/3	50%	346
3/5	25%	361
1	0%	389

matching catalogue, especially with very close but highly different in mass halo couples, we choose the limiting value of $\tilde{M} = 1/7$.

The statistical properties of the genuine haloes belonging to each simulation are summarised in Fig. 5.7, where we display the cumulative halo mass function (top right panel), the halo mass outside R_{200} (top left panel) – where R_{200} identifies the distance from the halo centre where the density is 200 times the critical density of the Universe and M_{200} the mass contained within a R_{200} radius sphere –, the subhalo mass function (bottom left panel), and the subhalo radial distribution (bottom right panel). In order to highlight the impact of numerical fragmentation and simplify the comparison of the different models to Λ CDM, relative ratios are displayed in the bottom panels and shaded lines represent the distribution of the full halo sample – i.e. including also spurious haloes –.

The analytical fit used by [Schive *et al.* \(2016\)](#) to parameterize the cumulative HMF drop of the FDM models with respect to Λ CDM

$$N(> M)_{\text{FDM}} = \int_M^{+\infty} \partial_M N_{\text{CDM}} \left[1 + \left(\frac{M}{M_0} \right)^{-1.1} \right]^{-2.2} dM \quad (5.8)$$

with $M_0 = 1.6 \times 10^{10} m_{22}^{-4/3} M_{\odot}$, are plotted as reference – one for each FDM mass –

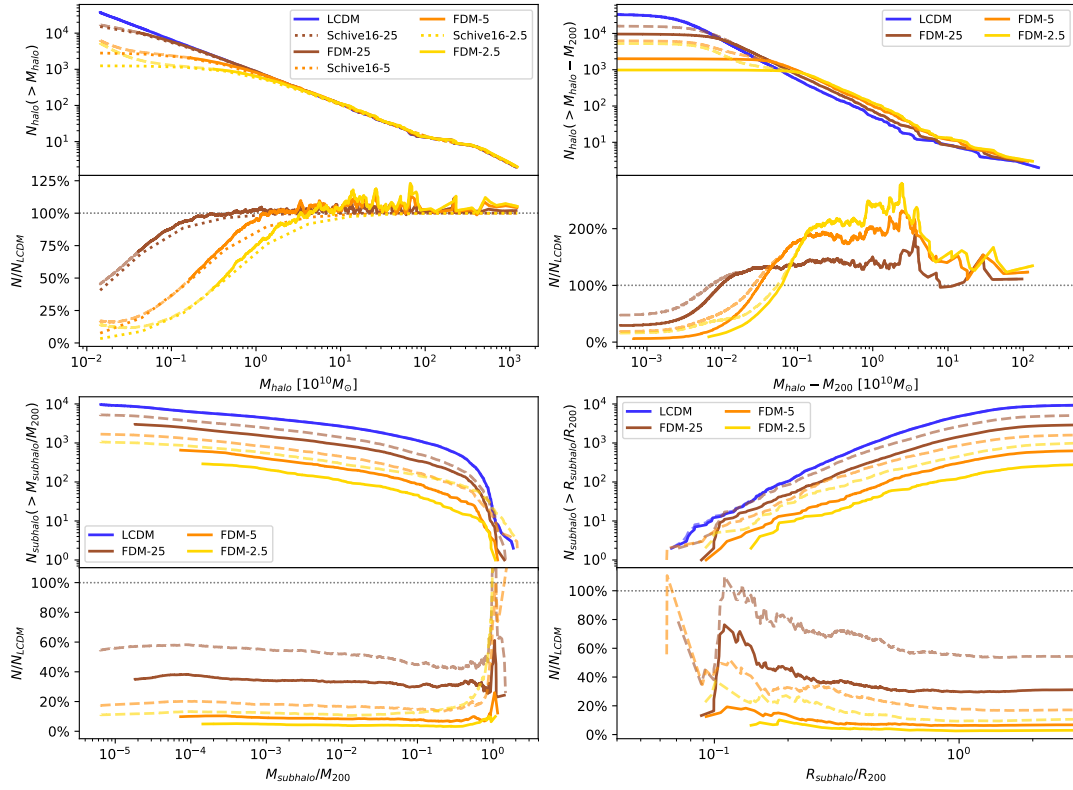


Figure 5.7: Properties of the halo and subhalo samples at $z = 0$, with (*dashed lines*) and without (*solid lines*) including the haloes marked as spurious as described in Sec. 5.3.1. In particular, the cumulative distributions of halo mass (*top left panel*), the halo mass outside R_{200} (*top right panel*), the subhalo-halo relative mass (*bottom left panel*) and the subhalo-halo distance (*bottom right panel*) are displayed. The fitting functions of the cumulative halo mass distribution of (Schive *et al.*, 2016) of Eq. 5.8 are plotted for reference – *dotted line in the top left panel* –.

in the top left panel of Fig. 5.7 (dotted lines).

As expected, we find that the number of small mass subhaloes is drastically reduced in the FDM models and the cumulative distributions depart from Λ CDM at higher and higher masses as the m_χ mass decreases. The values at which the drop occurs are approximately $5 \times 10^{10} M_\odot$, $2.5 \times 10^{10} M_\odot$ and $5 \times 10^9 M_\odot$ for values of m_{22} of 2.5, 5 and 25, respectively: this suggests a linear trend of the *threshold* mass

$$M_t \simeq 5 \times 10^{10} M_\odot \left(\frac{2.5}{m_{22}} \right) \quad (5.9)$$

describing the approximate mass below which the number of haloes starts decreasing with respect to Λ CDM.

Looking at the distribution of subhaloes masses as compared to their associated primary halo M_{200} and the radial distribution to R_{200} , it is evident how the numerous small subhaloes in Λ CDM, far from the gravitational centre of the main halo, are the ones that were not able to form in an FDM universe.

The haloes that have masses above M_t not only have been able to survive the disrupting QP action up to redshift $z = 0$, but the cumulative distribution shows how they also gained extra mass, at the smallest (sub)halo expenses. This is confirmed by the cumulative distribution of the primary structures $N(> M_{tot} - M_{200})$, representing the mass accumulated outside the R_{200} radius, which is systematically higher with respect to Λ CDM case as the FDM mass lowers – up to peaks of 200% ratio for the lowest m_{22} –: this is consistent with the picture of bigger primary haloes accreting the mass of un-collapsed smaller subhaloes that did not form.

The fitting function of Eq. 5.8 is consistent with the scale of the drop of the HFM, which is indeed expected to be almost redshift independent since it is predominantly given by the initial PS cut-off (Hu *et al.*, 2000). However, it fails to reproduce the data on two levels: on the one hand it does not recover the slope of the cumulative distribution – especially in the mass range close to M_t where the Halo Mass Function (HMF) departs from Λ CDM – and, on the other hand, does not account for the mass transfer from smaller haloes to bigger ones, that accrete the more abundant available matter from their surroundings. The discrepancies between the Schive *et al.* (2016) fitting function and our results are probably due to

the fact that the former is based on simulations with approximated FDM dynamics and evolved only to redshifts $z = 4$, thus representing a different collection of haloes that are, moreover, in an earlier stage of evolution.

Therefore, the analysis of the aggregated data of cumulative distributions of genuine haloes in each simulation leads us to conclude that the formation, the evolution and the properties of an FDM halo subject to the real effect of the QP – as compared to the FDMnoQP approximation – can follow three general paths depending on its own mass and on the mass of the FDM boson: if the halo mass is $M \ll M_t$, there is a high chance that the halo does not form at all since gravitational collapse is prevented by the QP; if $M \gtrsim M_t$, the halo can be massive enough to form but its properties will be affected by the QP – especially on its internal structure, as we will see below –, while for $M \gg M_t$ the halo is not severely affected by the QP, and will simply accrete more easily un-collapsed mass available in its surroundings.

In order to study in more detail the impact of FDM on the halo properties and structures, we divided our common sample, that by construction collects the haloes across all the simulations that share the same Λ CDM match (as described in detail in Section 5.3.2), in three contiguous mass ranges. Let us remind that matching haloes have similar but not necessarily equal mass, so mass intervals are to be referred to the Λ CDM halo mass; the other matching haloes belonging to the FDM simulations are free to have lower and higher mass, in accordance with the limit imposed by the \tilde{M} parameter of the common sample selection procedure. The common sample low mass end is clearly limited by the FDM-2.5 model, since it is the one with higher M_t , below which haloes have statistically lower chance to form. The three mass ranges are $[0.5 - 4]$, $[4 - 100]$, $[100 - 4000] \times 10^{10} M_\odot$, in order to be compatible with the three halo categories described in the previous paragraph for the FDM-2.5 model, being $M_t(m_{22} = 2.5) \sim 5 \times 10^{10} M_\odot$.

For all the matching haloes considered, we have tested the sphericity distribution, the halo volume and the total halo mass with respect to Λ CDM, as well as the radial density profiles.

Properties of inter-simulation matching haloes are gathered in Fig. 5.8, where the total sample is divided column-wise in the three mass ranges. The sphericity,

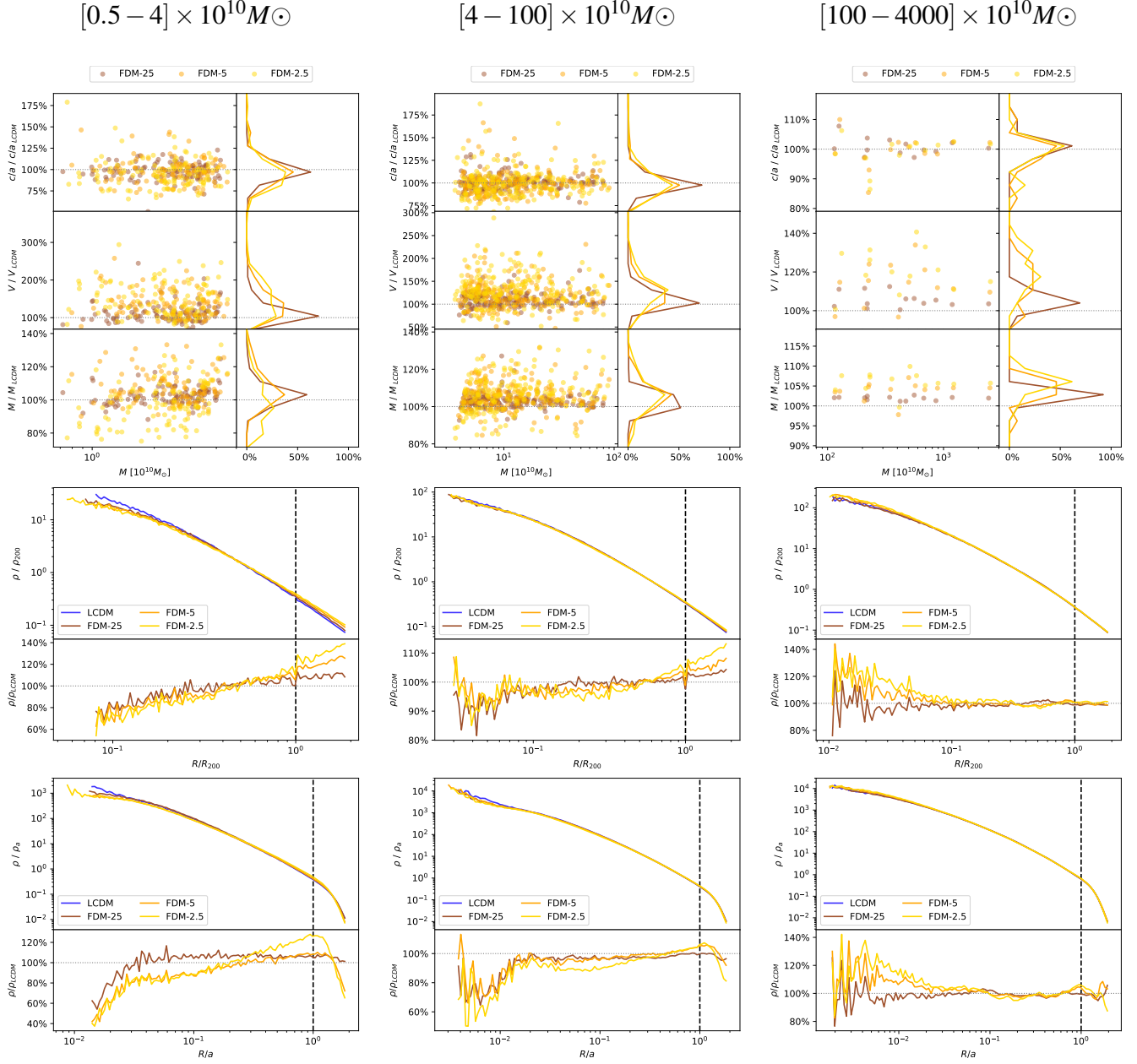


Figure 5.8: Properties of inter-simulation matching haloes, divided column-wise in three mass ranges. The sphericity, the volume occupied and the total mass of FDM haloes contrasted with their Λ CDM match are shown in the first row (*left panels*), together with related distribution functions (*right panels*). The second and the third row represent the density profiles, stacked in fractional spherical shells of R_{200} and ellipsoidal shells of the major axis a (*vertical dashed lines*), respectively. Densities are divided by its value calculated within R_{200} and a , respectively, and are shown both in absolute value (*top panels*) and relatively to Λ CDM. (*bottom panels*)

the volume occupied and the total mass of the haloes – contrasted with the corresponding Λ CDM match – are shown in the first row (*left panels*), together with related distribution functions (*right panels*). The second and the third row represent the overall density profiles, stacked in fractional spherical shells of R_{200} and ellipsoidal shells of the major axis a – identified with the vertical dashed lines –, respectively. Density profiles are divided by the value of the density calculated within the R_{200} and a shells and are shown both in absolute value (*top panels*) and relatively to Λ CDM (*bottom panels*).

In the mass range considered, the sphericity distributions confirm that there is no statistical deviation from Λ CDM, except for a mild deviation towards less spherical configurations of the less massive haloes, especially in the $m_{22} = 2.5$ model. This is consistent with the analysis of the sphericity distributions of the genuine samples (see *lower panels* in Fig. 5.6) that reveals that haloes appear to be statistically less spherical with respect to Λ CDM at $z = 0$ when lower FDM masses are considered, down to a maximum of $\sim 10\%$ decrease in sphericity for $m_{22} = 2.5$ and halo mass of $\sim 5 \times 10^9 M_{\odot}$.

For all the FDM models the volume occupied by the haloes is systematically larger, consistently with a *delayed* dynamical collapse of the haloes. All mass ranges show such property and it is emphasized by lower m_{22} mass – i.e. stronger QP force –; however, while bigger haloes occupy almost systematically 20% more volume for $m_{22} = 2.5$, smaller haloes can reach even twice the volume occupied by their Λ CDM counterparts when the same model is considered.

Comparing the mass of the haloes in the various models with the one in Λ CDM, it is possible to see that small haloes are less massive and big ones, on the contrary, become even more massive, confirming our hypothesis of mass transfer from substructures towards main structures.

The stacked density profiles provide even more insight on the different underlying behaviour between the chosen mass ranges. Starting from the less massive one, the stacked profiles look very differently if plotted using the spherical R_{200} -based or the ellipsoidal a -based binning. This is due to two concurrent reasons related to the properties of this mass range: first of all, as we said before, the sphericity is m_{χ} dependent and thus it is not constant with respect to Λ CDM, so the geometrical

difference in the bin shape becomes important when different models are considered; secondly, since the FDM haloes have lower mass but occupy larger volumes, the two lengths are different from each other – being R_{200} related to density and a purely to geometry – so that the actual volume sampled is different. Nevertheless, it is possible to see that in FDM models there is an excess of mass in the outskirts of the halo – seemingly peaking exactly at distance a – and less mass in the inner part.

The intermediate mass range shows also a suppression in the innermost regions but a less pronounced over-density around a as expected, since the effectiveness of the repulsive force induced by the QP in tilting the density distribution decreases as its typical scale becomes a smaller fraction of the size of the considered objects. In fact, stacked density profiles of the most massive haloes are very similar in the two binning strategies, being $R_{200} \sim a$ and sphericity constant among the various models, and consistent with no major deviation from Λ CDM, except for a central over-density. It is our opinion, however, that such feature in the very centre of most massive haloes could be a numerical artefact since its extension is comparable with the spatial resolution achievable in our simulation.

The results presented in this Section have been obtained through the detailed analysis of the statistical properties of haloes found at $z = 0$ in the FDM simulations. The same analysis, repeated at $z = 0$, of the FDMnoQP simulations, shows very similar results which are, therefore, not shown in the present work. Such consistency suggests that the properties of haloes at low redshift are – at the investigated scales – not sensible to modifications induced by the dynamical QP repulsive effect, which are expected to appear more prominently at scales of ~ 1 kpc with the formation solitonic cores.

5.4 Summary on Lyman- α and structure characterisation

In this Chapter, we have presented the results obtained from two sets of numerical simulations performed with the AX-GADGET, described in Section 4.1, for various FDM particle masses regarding Lyman- α forest observations and the detailed statistical characterisation of the haloes.

More specifically, our main aim was to design a set of simulations covering the typical scales and redshifts involved in Lyman- α forest analyses, in order to extract synthetic observations, compare them with available Lyman- α data, and finally to place a constraint on the mass of the FDM particle. In the literature, Lyman- α forest was already used for this purpose but only in approximated set-ups, in which the quantum dynamical evolution of FDM was only encoded in the initial conditions transfer function, and neglected during the simulation (Iršič *et al.*, 2017c; Armengaud *et al.*, 2017; Kobayashi *et al.*, 2017), while the AX-GADGET code allows us to drop such approximation and take into account the non-linear effects of full FDM dynamics.

The constraint we find on the FDM particle mass is $m_\chi \geq 21.08 \times 10^{-22} \text{ eV}/c^2$, which is 3% higher with respect to what was found in Iršič *et al.* (2017c) adopting the approximated simulation approach. The fact that these two bounds are similar, despite the different dynamical evolution considered in these different works, implies that the additional suppression deriving from the Quantum Potential dynamical contribution, at the scales and redshifts probed by Lyman- α , is compensated by the gravitational growth of perturbations when these enter the non-linear regime, implying also that – even if the QP does play a role in the Large Scale Structure evolution – the approximation of Iršič *et al.* (2017c) (also adopted by Armengaud *et al.*, 2017; Kobayashi *et al.*, 2017) is valid and sufficient at these scales.

Secondly, we studied in detail the statistical properties of the Large Scale Structures through the analysis of the aggregated data on haloes regarding their mass, volumes and shapes, as well as their individual inner structure.

The main results regarding the effects of FDM on LSS that we found can be summarised as follows:

- the FDM particle mass m_{22} defines a typical mass scale $M_t \simeq 1.25 \times 10^{11}/m_{22} M_\odot$ characterising the halo distribution of different FDM models; all halo properties can be interpreted within the framework of having two families of haloes: the small ones with $M \lesssim M_t$, and the big ones with $M \gg M_t$ (since the very small ones $M \ll M_t$ do not form at all);

- small haloes, according to the above definition, show outward tilted profiles and a lower total mass, are less spherical and more voluminous, so less dense overall;
- big haloes instead are almost unaffected in their internal structure – apart from the expected solitonic inner cores that we cannot resolve with our simulations –, they occupy a larger volume and they also have higher total mass, mostly accreted outside R_{200} , compatible with the collection of the mass of subhaloes that were not able to form

Part III

Generalised Strongly Coupled models

6

Coupled Dark Energy and Modified Gravity

In this chapter, we are going to present a separate project as part of my PhD work concerning the simulation of generalised dark energy and dark matter models that is still in progress. The project consists in the implementation of strongly coupled models into the P-GADGET3 code in a generalized approach, exploiting the tree representation as an adaptive mesh to solve the dark energy non-linear perturbation equation. We will see how various models that involve a modification of Einstein's General Relativity or one or more couplings between dark energy and other species in the Universe can be all described within a single analytical framework, which is the one used in our implementation. Our final goal is to apply such flexible tool that, provided with the particular variables and functions of the model of interest, could probe a vast number of Coupled Dark Energy and Modified Gravity models beyond Λ CDM at scales and regimes unexplored so far, thereby extending,

combining, and optimizing previous independent implementations targeted to specific Coupled Dark Energy (Baldi *et al.*, 2010) or Modified Gravity (Puchwein *et al.*, 2013) models.

6.1 Beyond the Cosmological Constant

The discovery of the accelerated expansion of the Universe played a major role in shaping the field of modern cosmology, supporting the need for some form of *dark energy* able to trigger and sustain the acceleration of cosmic expansion that eventually dominates the energy-matter content of the late-time Universe. In the Λ CDM framework, this contribution is encoded by a cosmological constant, but there are no particular assumptions with respect to its originating mechanism or its fundamental nature.

Given the negative pressure $P = -\rho c^2$ of the cosmological constant, dark energy was thought to be the macroscopic representation of the vacuum energy as described by quantum field theory, which was known to exhibit such peculiar property. However, the dark energy mean density required to comply with the observations is $\rho_{\Lambda,0} \sim 7 \times 10^{-30} \text{g/cm}^3$ that is ~ 120 orders of magnitude smaller than the Planck scale, which could be taken as the natural scale for quantum vacuum energy (for a review on the cosmological constant problem see e.g. Weinberg, 1989; Rugh and Zinkernagel, 2002). Moreover, one may find rather curious that our Universe entered the phase dominated by the cosmological constant quite *recently* – the equivalence $\rho_{\Lambda} = \rho_{mat}$ happened around $z \sim 0.55$ in the Λ CDM picture –, thus raising some additional *coincidence* problems (Zlatev *et al.*, 1999).

For these reasons, the term *dark energy* now generically refers to a physical mechanism that is at the origin of the acceleration of the cosmic expansion, including the simplest concept of the cosmological constant as well as other more elaborate alternatives. These may involve, for example, new interacting fields or fluids in the Universe, scale-dependent deviations from General Relativity, additional fundamental forces or extra-dimensions (for a comprehensive review on the topic, see e.g. Amendola *et al.*, 2018).

In order to generalize the dark energy description, one can assume that the cosmic expansion is driven by a fluid with a generic time-dependent equation of state $P_{DE} = w_{DE} \rho_{DE} c^2$ so that the background evolution of Eq. 1.40 reads

$$\begin{aligned} \left(\frac{H}{H_0}\right)^2 = & \Omega_{\text{rad},0} (1+z)^4 + \Omega_{\text{mat},0} (1+z)^3 + \left(1 - \sum_i \Omega_{i,0}\right) (1+z)^2 \\ & + \Omega_{DE,0} \exp\left(3 \int_0^z dz' \frac{1+w_{DE}(z')}{1+z'}\right) \end{aligned} \quad (6.1)$$

where the dark energy scaling in redshift may vary over cosmic time. In the matter-dominated era, the evolution of matter density perturbations becomes

$$\ddot{\delta} + 2H\dot{\delta} - 4\pi G\rho_b \left(\delta + \frac{\Omega_{DE}}{\Omega_{mat}} \delta_{DE}\right) = 0 \quad (6.2)$$

where δ_{DE} is the density contrast related to the dark energy fluid.

The simplest alternative to a cosmological constant is that of a second epoch of inflation, different in energy scale but driven by a similar mechanism: a scalar field slowly rolling down its self-interaction potential. In the so-called *Quintessence* models (Wetterich, 1988; Ratra and Peebles, 1988), the dark energy fluid is described in terms of a homogeneous scalar field ϕ called the *cosmon*, having

$$\begin{cases} \rho_{DE} c^2 = \dot{\phi}^2/2a^2 + V(\phi) \\ P_{DE} = \dot{\phi}^2/2a^2 - V(\phi) \end{cases} \quad (6.3)$$

so that the continuity equation of the dark energy fluid

$$\dot{\rho}_{DE} + 3H(\rho_{DE} + P_{DE}) = 0 \quad (6.4)$$

is linked to the cosmon dynamical evolution described by the Klein–Gordon (KG) equation

$$\ddot{\phi} + 3H\dot{\phi} + a^2 \partial_\phi V(\phi) = 0 \quad (6.5)$$

where $V(\phi)$ is a generic potential and the field ϕ is expressed in units of the

Planck mass $M_p = \sqrt{\hbar c / 8\pi G}$. Given the fluid–field transformation $\{\rho_{DE}, P_{DE}\} \leftrightarrow \{\dot{\phi}, V(\phi)\}$ the two descriptions are completely equivalent, so it is possible to choose the one that is more suitable to the problem on a case by case basis. The analytic form of the potential $V(\phi)$ affects the evolution of the dark energy density and its equation of state, which behaves consistently with a cosmological constant whenever the *slow-roll* condition

$$\dot{\phi}^2 / 2a^2 \ll V(\phi) \Rightarrow P_{DE} \simeq -\rho_{DE} \quad (6.6)$$

is satisfied. The most used forms of the potential in the literature are parametrized as

$$\begin{cases} V = A\phi^{-\alpha} & \text{Power-law (see e.g. Ratra and Peebles, 1988)} \\ V = Ae^{-\alpha\phi} & \text{Exponential (see e.g. Wetterich, 1988)} \\ V = A\phi^{-\alpha} e^{-\phi^2/2} & \text{Super gravity (see e.g. Brax and Martin, 1999)} \end{cases} \quad (6.7)$$

since they allow for slow-rolling solutions and exhibit scaling relations that make the cosmological evolution almost independent from the initial condition of the field (Ferreira and Joyce, 1998).

If one assumes that the dark energy is homogeneously distributed, the δ_{DE} contribution to the gravitational potential in Eq. 6.1 vanishes. In this case, the dark energy impacts only on the expansion history, and the evolution of matter density perturbations is modified only through the Hubble friction term $2H\dot{\delta}$. Therefore, the formation of large-scale structures is indirectly influenced by the background evolution of the Hubble function $H(z)$ that will set the cosmic time at which matter collapse occurs (see e.g. Wetterich, 1988; Ratra and Peebles, 1988). The homogeneity of the dark energy can be either assumed or arise as a dynamical property if the sound speed of the fluid $c_s^{DE} \sim c$ prevents it from clustering on scales smaller than the size of the cosmic horizon (see e.g. Ma *et al.*, 1999; Bartolo *et al.*, 2004; Alimi *et al.*, 2010).

When the assumption of the homogeneity of the cosmon field is dropped, clus-

tering can occur since the δ_{DE} contribution is restored. For example, in the *Clustering Dark Energy* models (see e.g. [Creminelli et al., 2009](#); [Sefusatti and Vernizzi, 2011](#)), the combination of fluid parameters $w_{DE} = -1$ and $0 < c_s^{DE} < c$ allows dark energy to simultaneously source an additional gravitational potential and promote space-time expansion.

In the case that dark energy is the manifestation of a hidden field, it is legitimate to suppose that this field could also interact through a *Fifth fundamental force* with the other components of the Universe. The potential associated with the new force field Φ_{∇} , characterized by a set of *coupling functions* $\beta_i(\phi)$ regulating the interaction between different species, would obey a non-linear Poisson equation

$$\nabla^2 \Phi_{\nabla} = a^2 F(\phi) + 8\pi G a^2 \sum_i^{\text{interacting}} \beta_i(\phi) \bar{\rho}_i \delta_i \quad (6.8)$$

where $\bar{\rho}_i$ is the background density of the species i and F is a generic function of the cosmon ([Baldi, 2012](#)). Instead, the standard Newtonian potential Φ_N satisfies the usual linear Poisson equation

$$\nabla^2 \Phi_N = 4\pi G a^2 \sum_i^{\text{clustering}} \bar{\rho}_i \delta_i \quad (6.9)$$

and is sourced by all the clustering species.

Therefore, the acceleration of a particle of the species i can be expressed by Eq. 2.3 as

$$\dot{\vec{u}} + 2H\vec{u} = -\frac{\vec{\nabla}\Phi_N}{a^2} - \beta_i(\phi) \frac{\vec{\nabla}\Phi_{\nabla}}{a^2} \quad (6.10)$$

where the fifth force is added to the standard gravitational one ([Baldi, 2012](#)). The introduction of a coupling effectively allows the particle mass of the species to depend on the cosmon field $m_i(\phi)$, often parametrized as

$$m_i(\phi) = \bar{m}_i e^{-\beta_i(\phi)\phi} \quad (6.11)$$

without loss of generality, where \bar{m}_i is the constant bare mass of the particles of

that species (Amendola *et al.*, 2008). The form of Eq. 6.10 and of the potentials of Eq. 6.8 and Eq. 6.9 is rather general and encompasses a wide range of *coupled* dark energy models.

It can be shown that it is possible to describe equivalently the interactions between dark energy and other species in terms of a modification of the standard space-time metric, consistent with assuming a *Modified* version of Einstein's *Gravity* (Pettorino and Baccigalupi, 2008). Therefore, coupled dark energy and Modified Gravity models are generally considered to be a unique class of theoretical extensions of the Λ CDM scenario, involving the variation of both background expansion history and clustering mechanisms of the different species (see e.g. the reviews Tsujikawa, 2011; Amendola *et al.*, 2018).

In the case of a *universal* coupling $\beta_i(\phi) = \beta(\phi) \forall i$, dark energy equally interacts through the fifth force with all the species in the Universe and it is possible to rewrite the total force in the right-hand side of Eq. 6.10 as

$$-\vec{\nabla}(\Phi_N + \Phi_{\mathbb{V}}) = -\vec{\nabla} [a^2 F(\phi) + (1 + 2\beta^2(\phi)) \Phi_N] \quad (6.12)$$

thus translating it into an effective description of a modified theory of gravity – i.e. maximally coupled by nature –. In this class of models, there are the *Extended Quintessence* models (see e.g. Perrotta *et al.*, 1999; Baccigalupi *et al.*, 2000; Pettorino and Baccigalupi, 2008), higher-dimensional theories of gravity as e.g. the *DGP* (Dvali *et al.*, 2000), the *Dilaton* (Gasperini *et al.*, 2001), the *Galileon* (see e.g. Nicolis *et al.*, 2009) or the *Symmetron* (Hinterbichler and Khoury, 2010) and the family of $f(R)$ modified gravity models (see e.g. Hu and Sawicki, 2007; De Felice and Tsujikawa, 2010).

The deviation of these models from Einstein's theory of gravity has to be negligible at small scales, in order to be consistent with solar system constraints on General Relativity (Bertotti *et al.*, 2003; Will, 2006), thus requiring a *screening mechanism* to mask the effects of the fifth force in high-density regions – as e.g. the *Chameleon* (Khoury and Weltman, 2004), the *Veinshtein* (Vainshtein, 1972) or the *Symmetron* (Hinterbichler and Khoury, 2010) mechanisms –.

A screening mechanism is needed to comply with the solar system constraints in the case of a universal coupling, but it is not necessary if we assume that the cosmological coupling with baryons is negligible (Damour *et al.*, 1990). This possibility is allowed in the context of *Coupled Dark Energy* models in which every species is characterised by its own coupling with dark energy. In particular, the single species interaction of dark energy–dark matter (see e.g. Wetterich, 1995; Amendola, 2000, 2004) and dark energy–massive neutrinos (Amendola *et al.*, 2008) have been widely investigated.

Whenever a matter species i interacts with the scalar field, the energy budget is conserved for the two species combined since they can exchange energy. Therefore, the continuity equation of species i and the non-linear Klein–Gordon equation of the field become

$$\begin{cases} \dot{\rho}_i + 3H\rho_i(1 + w_i) = -\dot{\phi} \beta(\phi) \rho_i(1 - 3w_i) \\ \ddot{\phi} + 3H\dot{\phi} + a^2\partial_\phi V(\phi) = a^2\beta(\phi) \rho_i(1 - 3w_i) \end{cases} \quad (6.13)$$

which decouple in the case of a relativistic species characterized by equation of state $w \rightarrow 1/3$ – e.g. as it happens at high redshifts for the relativistic neutrinos in Growing Neutrino Quintessence models –.

In the case of a single coupling, the function F is related to a derivative of the potential $\partial_\phi V$ and, in the slow-rolling approximation required for the cosmic accelerated expansion, is negligible with respect to the fluid interaction, resulting in

$$\nabla^2\Phi_{\mathbb{Y}} \simeq 8\pi G a^2 \beta_i(\phi) \bar{\rho}_i \delta_i = 2\beta_i(\phi) \nabla^2\Phi_{N,i} \quad (6.14)$$

where $\Phi_{N,i}$ is the contribution of the species i to the total gravitational potential. The modified Euler equation of Eq. 6.10 can be then expressed as

$$\dot{\vec{u}}_i + (2H - \dot{\phi}\beta_i(\phi)) \vec{u}_i = -\frac{\vec{\nabla}\Phi_N}{a^2} - 2\beta_i(\phi) \frac{\vec{\nabla}\Phi_{N,i}}{a^2} \quad (6.15)$$

where the additional friction term $\dot{\phi}\beta_i(\phi)$ comes from momentum conservation – in particular, from the time derivative of the mass of Eq. 6.11 – that has to be

imposed when the coupling is not universal (see e.g. [Amendola, 2000](#); [Macció *et al.*, 2004](#); [Baldi *et al.*, 2010](#)). This argument has been also extended to two ([Baldi, 2012](#); [Huey and Wandelt, 2006](#); [Bonometto *et al.*, 2012](#)) or multiple ([Brookfield *et al.*, 2008](#); [Cai *et al.*, 2016](#)) interactions models, in which it is required to separately solve for the gravitational potential of each coupled matter component.

While a coupling β_{bar} between dark energy and baryons is severely constrained by solar system tests ([Bertotti *et al.*, 2003](#)), one between dark energy and dark matter β_{cdm} is not directly affected by the solar system experiments. However, since dark matter is the leading player in structure formation, the CDM coupling is constrained by the combination of CMB and large-scale structures data to be $0 < \beta_{cdm} \leq 0.1$ ([Amendola *et al.*, 2003](#); [Bean *et al.*, 2008](#); [Pettorino *et al.*, 2012](#)).

The species that allows for the most significant coupling with dark energy is massive neutrinos, mainly for two reasons: neutrinos interact exceptionally weakly with standard matter and their contribution Ω_ν is sub-dominant during structure formation – though the exact value of the neutrino masses is not known, [Planck Collaboration \(2018\)](#) sets an upper bound on the sum of neutrino masses $\sum m_\nu < 0.12 \text{ eV}/c^2$ under the assumption of Λ CDM cosmology, thus resulting in $\Omega_{\nu,0} \lesssim 0.002$ today –. As a consequence of these two properties, the coupling β_ν may have values as large as $O(100)$. Since the coupling vanishes for relativistic species, and neutrinos are relativistic at high redshift, such interaction can influence dark energy evolution without violating solar system tests nor impact early structure formation.

The general picture that encompasses the Coupled Dark Energy and Modified Gravity models we are interested in can be summarized in the following set of equations: a global set regarding the sources of the newtonian potential, the fifth

force potential and the scalar field

$$\left\{ \begin{array}{ll}
 \nabla^2 \Phi_N = 4\pi G a^2 \sum_i^{\text{clustering}} (\rho_i - \bar{\rho}_i) & \text{Linear Poisson Eq.} \\
 \nabla^2 \Phi_Y = a^2 F(\phi) + 8\pi G a^2 \sum_i^{\text{interacting}} \beta_i(\phi) (\rho_i - \bar{\rho}_i) & \text{Non-linear Poisson Eq.} \\
 \ddot{\phi} + 3H\dot{\phi} + a^2 \partial_\phi V(\phi) = -a^2 \sum_i^{\text{interacting}} \beta_i(\phi) \rho_i (1 - 3w_i) & \text{Non-linear KG Eq.}
 \end{array} \right. \quad (6.16)$$

and a set for each species i involved in the system

$$\left\{ \begin{array}{ll}
 \ddot{\vec{u}}_i + [2H - \dot{\phi} \beta_i(\phi)] \vec{u}_i = \frac{\vec{\nabla} \Phi_N}{a^2} - \beta_i(\phi) \frac{\vec{\nabla} \Phi_Y}{a^2} & \text{Modified Euler Eq.} \\
 \dot{\rho}_i + 3H\rho_i(1 + w_i) = -\dot{\phi} \beta_i(\phi) \rho_i (1 - 3w_i) & \text{Continuity Equation} \\
 \beta_i(\phi) = -\ln \frac{m_i(\phi)}{\bar{m}_i} & \text{Coupling Equation} \\
 P_i = w_i \rho_i c^2 & \text{Equation of state}
 \end{array} \right. \quad (6.17)$$

concerning its dynamics and interactions with the scalar field. The whole class of models described in this general way features an additional fifth fundamental force that mediates the interaction between a scalar field with one or multiple species in the Universe.

6.2 $f(R)$ -models and the MG-GADGET implementation

In the rest of the chapter, we will discuss two cases that can be interpreted within this framework. The first one is the family of $f(R)$ modified gravity models, since it has been already encoded in the MG-GADGET module of the P-GADGET3 code

(Puchwein *et al.*, 2013) with an *ad hoc* multi-grid field approach that will be the base of our generalised implementation. The second one, instead, is a coupled dark energy model known as the *Growing Neutrino Quintessence* scenario that has been simulated in the past both within a Newtonian approach with P-GADGET3 (Baldi *et al.*, 2011) and within a relativistic one with an independent N-body code (Ayaita *et al.*, 2012). However, the former could not properly follow the system into the relativistic regime at low redshifts, and the fixed PM grid of the latter hindered – both in terms of accuracy and computational cost – the possibility to simulate cosmologically relevant volumes.

In $f(R)$ -models (Buchdahl, 1970), the Einstein equations of Eq. 1.8 are generalised by replacing the Ricci scalar as $R \rightarrow R + f(R)$ thus obtaining

$$R_{\mu\nu} - \frac{1}{2}g_{\mu\nu}R + f_R R_{\mu\nu} - \frac{1}{2}g_{\mu\nu}f(R) + [g_{\mu\nu}\square + \nabla_\mu \nabla_\nu] f_R = \frac{8\pi G}{c^4} T_{\mu\nu} \quad (6.18)$$

where f_R is conventionally defined as the derivative

$$f_R \equiv \partial_R f(R) \quad (6.19)$$

as detailed e.g. by Tsujikawa (2011).

In these models, the introduction of f_R in the Einstein equations is analytically equivalent to the presence of a scalar field $\phi \equiv f_R$ that is universally coupled – with a constant coupling β – with all the matter species of the Universe (Pettorino and Baccigalupi, 2008).

Assuming the peculiar form of the $f(R)$ function as in Hu and Sawicki (2007), the background evolution of the field is

$$\bar{f}_R = f_{R,0} \left(\frac{R_0}{R} \right)^2 = f_{R,0} \left(\frac{4\Omega_\Lambda/\Omega_{mat} + 1}{4\Omega_\Lambda/\Omega_{mat} + a^{-3}} \right)^2 \quad (6.20)$$

whose perturbations source the fifth force potential

$$\nabla^2 \Phi_{\nabla} = \frac{c^2 a^2}{2} \nabla^2 f_R = \frac{a^2 \sqrt{f_{R,0}}}{6} \left(\frac{1}{\sqrt{f_R}} - \frac{1}{\sqrt{\bar{f}_R}} \right) - \frac{4\pi G}{3} (\rho - \bar{\rho}) a^2 \quad (6.21)$$

where we can identify

$$\begin{cases} F(f_R) = \frac{\sqrt{f_{R,0}}}{6} \left(\frac{1}{\sqrt{f_R}} - \frac{1}{\sqrt{f_{R,0}}} \right) \\ \beta = \frac{1}{6} \end{cases} \quad (6.22)$$

as the mapping with the general picture previously described. The equations presented above are related to one specific form among many that the function $f(R)$ can take, but the same mapping argument can be applied in other cases (see e.g. the reviews [Berti *et al.*, 2015](#); [Koyama, 2016](#), on the theoretical models and observational tests of Modified Gravity).

6.2.1 The multi-grid Newton–Gauss–Seidel solver

The standard Fourier–transform based methods, usually applied on a regular lattice to solve the linear Poisson equation as the one valid for the standard gravitational potential, are not suitable to solve the non-linear Poisson equation for $\nabla^2\Phi_{\mathcal{U}}$. In fact, the general combination of the $F(\phi)$ function and the couplings $\beta(\phi)$ contribute to the high non-linearity of the problem, whose solution depends on the complex interplay between matter and the new scalar field of the local environment.

The implementation of a dedicated solver for a non-linear Poisson equation in an N-body code called DGPM was introduced in the three-pronged work by [Oyaizu \(2008\)](#); [Oyaizu *et al.* \(2008\)](#); [Schmidt *et al.* \(2009\)](#) in the specific case of $f(R)$ –gravity – later implemented into the P-GADGET3 code by ([Puchwein *et al.*, 2013](#)) as the MG-GADGET module–.

A similar approach was also applied in the Eulerian code MLAPM ([Li and Zhao, 2009](#); [Zhao *et al.*, 2010](#); [Zhao *et al.*, 2011](#)) that improved the resolution achievable by the previous [Oyaizu \(2008\)](#) implementation. The porting of the MLAPM routines into the ECOSMOG module ([Li *et al.*, 2012](#)) within the N-body code RAMSES featured extensive progress in the parallelisation and the multi-grid refinement that allowed in-depth investigation of the $f(R)$ cosmologies properties (see [Winther *et al.*, 2015](#), for a comparison between different Modified Gravity codes). The fea-

tures of $f(R)$ models have been largely studied and compared with observations (see [Berti *et al.*, 2015](#); [Koyama, 2016](#)) in a wide range of systems and physical processes: these include e.g., Lyman- α forest constraints from large-scale structures (see e.g. [Arnold *et al.*, 2015](#)), simulations of Milky-way like haloes (see e.g. [Arnold *et al.*, 2016](#)) and dwarf galaxies (see e.g. [Jain and VanderPlas, 2011](#)), Halo Mass Functions detailed investigation (see e.g. [Schmidt *et al.*, 2009](#); [Schmidt, 2010](#); [Li and Hu, 2011](#); [Achitouv *et al.*, 2016](#); [von Braun-Bates *et al.*, 2017](#)), lensing (see e.g. [Schmidt, 2008](#); [Peel *et al.*, 2018](#)) and kinematic analysis of galaxy clusters (see e.g. [Cataneo *et al.*, 2015](#); [Pizzuti *et al.*, 2017](#)).

In all the different implementations mentioned above, the scalar field distribution is iteratively solved on a mesh, where at each iteration the value of the field at a given cell is only related to its 2^{dim} neighbours. In this way, the problem can be factorised identifying two domains with antiferromagnetic configuration – i.e. a dim dimensional red–black chessboard – so that, for a single iteration, the cells belonging to one domain are only affected by the cells of the other one. For simplicity, will hereafter restrict to the cosmological 3D case.

For the mesh grid Ω_h characterized by a grid spacing h , it is useful to define the dimensionless field variable identified by the cell indexes $\{i, j, k\} \in \Omega_h$ as

$$u_{i,j,k} = \frac{\phi_{i,j,k}}{\bar{\phi}} \quad (6.23)$$

and the field difference between neighbouring cells as

$$b_{i,i+1} = u_{i+1,j,k} - u_{i,j,k} \quad (6.24)$$

so that the local Laplacian, computed with a second-order finite-difference method, reads

$$\nabla^2 (u_{i,j,k}) = \frac{1}{2h^2} [b_{i,i+1} - b_{i-1,i} + b_{j,j+1} - b_{j-1,j} + b_{k,k+1} - b_{k-1,k}] \quad (6.25)$$

where $b_{j,j+1}$ and $b_{k,k+1}$ are equivalent to $b_{i,i+1}$ in the other dimensions.

Since negative values are expected for the field in order to comply with observa-

tions in $f(R)$ -gravity models, [Oyaizu \(2008\)](#) introduced a temporary new dimensionless field

$$e^{u_{i,j,k}} = \frac{\phi_{i,j,k}}{\bar{\phi}} \quad (6.26)$$

for which the finite-difference reads

$$b_{i,i+1} = (e^{u_{i+1,j,k}} + e^{u_{i,j,k}}) (u_{i+1,j,k} - u_{i,j,k}) \quad (6.27)$$

so that solving for $\nabla^2(e^{u_{i,j,k}})$ does not allow the field to change its sign, resulting in a more stable algorithm for that specific case. Nevertheless, the particular form of the fundamental field variable – i.e. either exponential or not – does not affect the general implementation of the solver.

The total solution for the level Ω_h

$$u_h \equiv \{u_{i,j,k} : \forall \{i,j,k\} \in \Omega_h\} \quad (6.28)$$

is found by iteratively computing the Laplacian for the two domains one after the other – referred as *red* and *black sweeps* – and iterating this process until a stable solution is reached.

The relaxation scheme used for the convergence is the Newton–Gauss–Seidel (NGS) method (see e.g. [Moré, 1971](#)), in which Eq. 6.8 is expressed in the form

$$\mathcal{L}(u_h) = f_h \quad (6.29)$$

where the $\mathcal{L}(u_h)$ function includes all the terms that are field dependent while f_h represents the remainder. The single iteration $n \rightarrow n+1$ updates the field according to

$$u_h^{n+1} = u_h^n - \left(\frac{d \mathcal{L}(u_h^n)}{d u_h^n} \right)^{-1} (\mathcal{L}(u_h^n) - f_h^n) \quad (6.30)$$

and is repeated for both the red and black sweeps until a given level of convergence ε

$$|\mathcal{L}(u_h) - f_h| < \varepsilon \quad (6.31)$$

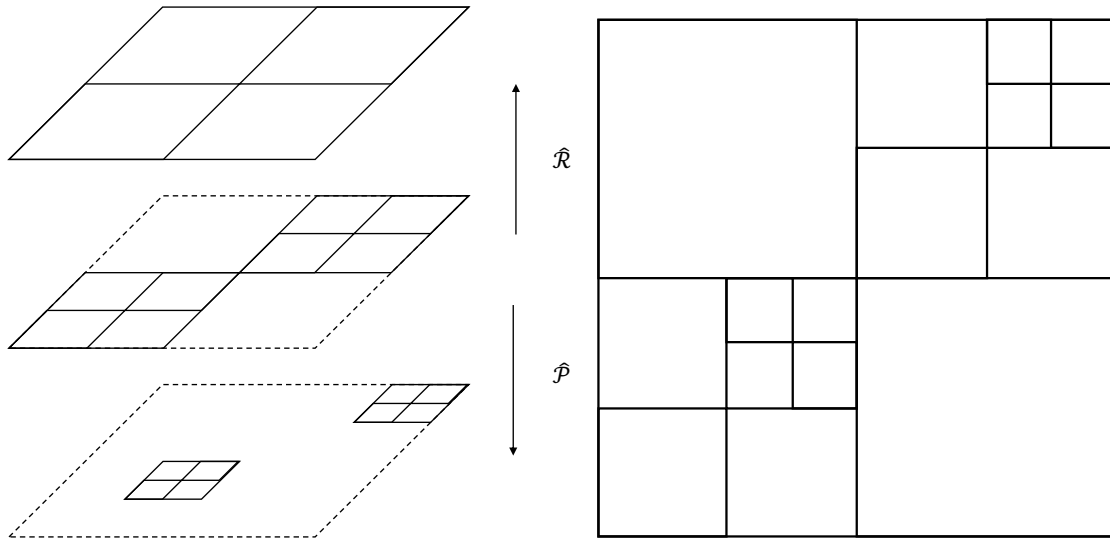


Figure 6.1: Schematic representation projected in 2D of the adaptive mesh levels (*left panel*) with the *Restriction* $\hat{\mathcal{R}}$ and *Prolongation* $\hat{\mathcal{P}}$ operators and the flattened tessellation of the levels (*right panel*).

is reached. The algorithm clearly requires an initial guess u_h^{old} for the first iteration: at the beginning of the simulation this value has to be manually provided while, at subsequent time step, the solution at the previous global time-step is used. For illustrative purposes, we define the solution obtained with such relaxation scheme as

$$u_h = \mathcal{L}^{-1}(f_h, u_h^{old}) \quad (6.32)$$

where we explicit the dependence on the initial guess.

On a regular and space-filling grid, at each red and black iteration of the NGS scheme the effect of the field and the mass at a given cell has propagated only by two cells, requiring *at least* a number of operations of the order of $M^2/2$ to fully correlate a mesh level with M cells. For this reason, solving partial differential equations over the whole domain with relaxation methods is very inefficient and computationally expensive. Nevertheless, the efficiency can be largely improved by the use of multi-grid techniques (see e.g. [Bramble, 1993](#), for a review on the multi-grid class).

Multi-grid methods are a class of optimisation algorithms that boost a grid-based relaxation scheme performance mapping the problem into a hierarchy of coarser grids in order to reduce the number of steps needed to fully correlate the system under investigation. In particular, both Oyaizu (2008) and Puchwein *et al.* (2013) implementations feature the so-called Full Approximation Scheme (Briggs *et al.*, 2000).

The Full Approximation Scheme consists in applying the NGS not on the regular grid with the highest resolution allowed but level by level on a hierarchical grid, mapping the relaxed solutions to the coarser or finer level with the *Prolongation* $\hat{P} : \Omega_{2h} \rightarrow \Omega_h$ and *Restriction* $\hat{R} : \Omega_h \rightarrow \Omega_{2h}$ operators, respectively. The specific form of the two operators may vary, for example, the mapping to a coarser level can be performed assigning the mean value of the daughter nodes to their parent while the value of the latter is assigned back to its daughters in the mapping to a finer level.

In the P-GADGET3 implementation, this hierarchical grid is already embodied by the flexible tree built to compute the gravitational potential whose nodes, adequately selected, serve as a space-filling adaptive mesh, as schematically portrayed in Fig. 6.1. The interpolation of properties from particles to cells – i.e. essentially particle mass, in the $f(R)$ case – is performed through the CIC scheme as described in Section 2.3.

In Fig. 6.2 the iterative Full Approximation Scheme is represented in a flowchart, describing how the NGS relaxation solver is iteratively applied level by level starting from the finest one to the coarsest and back. In these so-called *vertical V-cycles* the information retained by a cell is propagated much more efficiently through the whole box with respect to an *horizontal* neighbour by neighbour propagation within the same level.

Once the non-linear Poisson Equation is solved, the fifth force contribution can be applied to the particles and the simulation proceed normally. The various routines that are involved in the calculation of the fifth force in MG-GADGET (Puchwein *et al.*, 2013) – i.e. the CIC interpolation, the NGS solver, the multi-grid operators – have been implemented specifically for the particular $f(R)$ -gravity case and

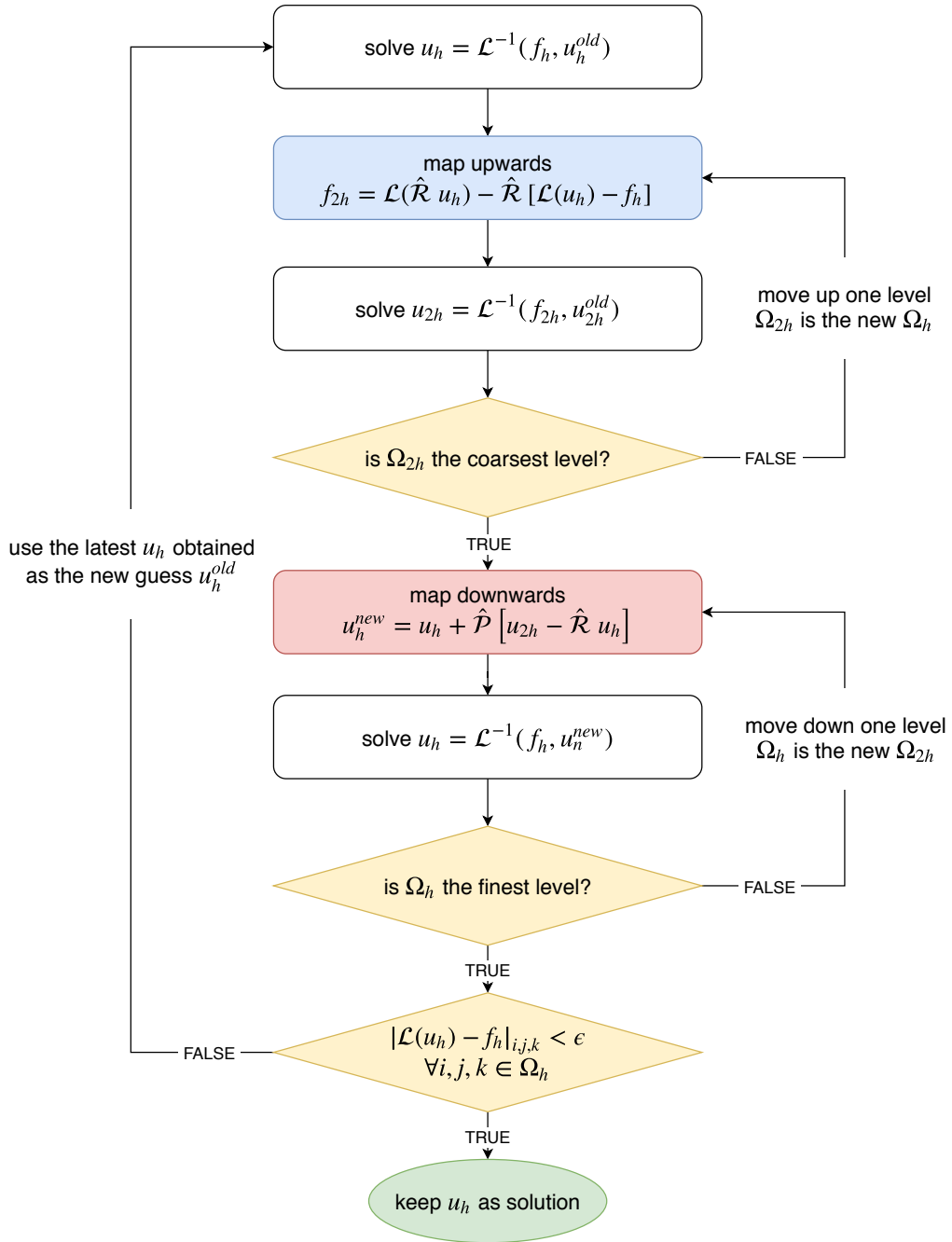


Figure 6.2: Flowchart of multigrid Full Approximation Scheme of the Newton-Gauss-Siedel solver.

its variables and functions were simply *hard-coded*. Our goal is to accommodate a general description of dark energy and modified gravity models in this implementation, in which the user can provide the relevant parameters as well as the main functions that describe the model of interest, namely $V(\phi)$, $F(\phi)$ and the set of couplings $\beta_i(\phi)$.

6.3 Growing Neutrino Quintessence

In Growing Neutrino Quintessence models, neutrinos and dark energy interact throughout the cosmic evolution (Amendola *et al.*, 2008). While the background evolution is influenced by the dark energy at all times, the neutrino dynamics is directly affected by the coupling with dark energy only in the non-relativistic regime, due to their relativistic nature in the early Universe. In fact, we can express the density and the equation of state of neutrinos as

$$\begin{cases} \rho_i = \frac{m_i \gamma_i}{V_i} \\ w_i = P_v / \rho_v c^2 = \frac{1}{3} \left(1 - \frac{1}{\gamma_i^2} \right) \end{cases} \quad (6.33)$$

where $\gamma_i = (1 + |\vec{v}_i|^2/c^2)^{-1/2}$ is the usual *Lorentz factor*. The background solution for the neutrino density $\bar{\rho}_v$ and the cosmon $\bar{\phi}$ satisfy

$$\begin{cases} \dot{\rho}_v + 3H\rho_v(1 + w_v) = -\dot{\phi} \beta(\phi) \rho_v(1 - 3w_v) \\ \ddot{\phi} + 3H\dot{\phi} + \partial_\phi V(\phi) = a^2 \beta(\phi) \rho_v(1 - 3w_v) \end{cases} \quad (6.34)$$

which decouple when the neutrino are in the relativistic regime characterized by equation of state $w_v \rightarrow 1/3$. Therefore, after the decoupling between the radiation and neutrino species – occurring at a redshift z_{NR} that depends on the present neutrino mass and on the coupling $\beta(\phi)$ –, the latter interacts heavily with dark energy with the net effect of losing its kinetic energy in favour of cosmic expansion, thus collapsing in huge and dense neutrino lumps up to 50 – 100 Gpc in size: with this mechanism, the late-time expansion of the Universe is propelled by the energy of neutrinos at the transition to the non-relativistic regime.

The fifth force potential sourced by the dark energy perturbation and the coupling with neutrinos is

$$\nabla^2 \Phi_{\Sigma} = \nabla^2 \phi = a^2 \partial_{\phi}^2 V(\bar{\phi}) + 2\Phi_N \partial_{\phi} V(\bar{\phi}) + a^2 \beta(\phi) \rho_{\nu} (1 - 3w_{\nu}) - a^2 \overline{\beta(\phi) \rho_{\nu} (1 - 3w_{\nu})} (1 - 2\Phi_N) \quad (6.35)$$

which will strongly affect the physical processes within the neutrino lumps. In GNQ, perturbations in the neutrino density become non-linear already at $z \sim 1 - 2$ on very large scales (Mota *et al.*, 2008).

In this sense, the choice of the potential $V(\phi)$ and, even more remarkably, of the coupling $\beta(\phi)$ is of crucial importance in order for the model to be consistent with observations. The case of constant coupling $\beta(\phi) = \beta$ have been largely investigated at the linear level (see e.g. Afshordi *et al.*, 2005; Mota *et al.*, 2008) and in non-linear semi-analytical extrapolations (Wintergerst *et al.*, 2010; Wintergerst and Pettorino, 2010; Brouzakis *et al.*, 2011). The coupling required for dark energy to dominate the late-time Universe is of the order $\beta \gtrsim 50 - 100$, meaning that the additional force between neutrinos will be about of the order of $O(10^3 - 10^4)$ times larger than the gravitational interaction experienced by neutrinos. In turn, the large-scale lumps develop very quickly as soon as neutrinos become non-relativistic. Due to neutrino in-fall in the lump potential and the high value of the cosmon within it, the neutrino mass of Eq. 6.11 inside lumps is substantially smaller than the average mass of the background (homogeneous) solution. As a consequence, neutrinos are effectively accelerated again to relativistic velocities (Baldi *et al.*, 2011). These effects are so powerful, in the constant coupling case, that the evolution of the cosmon gets too weak, making it difficult to obtain a realistic cosmology (see Führer and Wetterich, 2015, for a detailed description of back-reaction effects in GNQ).

More complex coupling functions of the field like the inverse power law

$$\beta(\phi) = -\frac{1}{\phi_c - \phi} \Rightarrow m_{\nu}(\phi) = \frac{\overline{m}_{\nu}}{\phi_c - \phi} \quad (6.36)$$

has proven to be compatible with observations for the case of a present neutrino mass $m_{\nu,0} \sim 0.07 eV/c^2$ (Ayaita *et al.*, 2016; Casas *et al.*, 2016). In this case, the critical

value ϕ_c is introduced only to create a barrier such that the resulting coupling is not large in the early Universe and start growing only in recent times.

In general, lumps with size of 100 Mpc or more could lead to observable effects on the CMB anisotropies in the low multipole tail (Pettorino *et al.*, 2010). At the present stage, the uncertainties of their estimate make it difficult to constrain the parameter space of growing neutrino models, also from a numerical point of view (Watkins *et al.*, 2009; Ayaita *et al.*, 2009). In fact, GNQ numerical implementation has been either based on a Newtonian approach (see Baldi *et al.*, 2011, implementation in P-GADGET3), which was not suitable to investigate the low-redshift relativistic regime, or on a relativistic one (with the independent N-body code Ayaita *et al.*, 2012) that, however, could not probe the relevant cosmological scales for the CMB effects, being a fixed-grid based code without inter-nodes parallelisation strategies.

6.3.1 Our generalised implementation: the GNQ case

As we showed in Section 6.1, GNQ can be ascribed to a more general group of models, as any model involving an interaction between different species and a scalar field or scalar-tensor modified gravity models. Therefore, it represents a perfect target for our generalised implementation.

The massive parallelisation of P-GADGET3 ensures the numerical possibility to simulate larger portions of the Universe. Thanks to our extension of the NGS solver, already implemented in the MG-GADGET module for the $f(R)$ case (Puchwein *et al.*, 2013), the code is now able to solve very efficiently any given scalar field non-linear Poisson Equation in the form of Eq. 6.8. As in the $f(R)$ case of Section 6.2, in our implementation the functions $V(\phi)$, $F(\phi)$, and the cosmoneutrino coupling $\beta(\phi)$ can be provided at compilation time. The mappings between particles and cells of the grid – built adaptively on the tree nodes – lost their explicit *hard-coded* form and were *soft-coded* in *projector* functions that can be provided. In this way, we can use the CIC interpolation to map the neutrino properties to the adaptive mesh.

Moreover, to improve the results obtained with the previous implementation of Baldi *et al.* (2010), the relativistic nature of neutrinos has been taken into account:

as we described, the velocity of each neutrino particle modifies its energy balance, its coupling strength and its mass.

We present the schematic summary of the operations performed at each global step by our general implementation – in addition to the standard steps of a CDM simulation – in the specific case of GNQ models.

- *Neutrino individual and average properties:*

The following quantities are mapped from neutrinos to each grid cells i calculated as

$$\left\{ \begin{array}{l} \rho_i = \sum_{j \in \mathcal{C}(i)} m_j(\phi_i) \gamma_j(\vec{u}_j) \mathcal{W}(\vec{x}_j) \\ w_i = P_i/\rho_i c^2 = \frac{1}{3} \sum_{j \in \mathcal{C}(i)} \left(1 - \frac{1}{\gamma_j(\vec{u}_j)^2} \right) \mathcal{W}(\vec{x}_j) \\ \beta(\phi_i) \rho_i (1 - 3w_i) = -\beta(\phi_i) \sum_{j \in \mathcal{C}(i)} \frac{m_j(\phi_i)}{\gamma_j(\vec{u}_j)} \mathcal{W}(\vec{x}_j) \end{array} \right. \quad (6.37)$$

where $\mathcal{C}(i)$ and $\mathcal{W}(\vec{x}_i)$ represent the particles ensemble and the filter that characterise the interpolation scheme used – e.g. for the NGP case, $\mathcal{C}(i)$ contains only the particle belonging to the cell i and $\mathcal{W}(\vec{x}_i)$ is equal to its volume –. As the standard approach, we use the CIC scheme described in Section 2.3. The background average value of these quantities $\bar{\rho}_\nu$, \bar{w}_ν and $\overline{\beta(\phi) \rho_\nu (1 - 3w_\nu)}$ are stored in the coarsest level since it represents the whole simulation domain.

- *Scalar field background:*

Using the background observables of neutrino species, the homogeneous quantities related to the scalar field $\dot{\phi}$ and $\ddot{\phi}$ are derived from

$$\left\{ \begin{array}{l} \dot{\rho}_\nu + 3H\bar{\rho}_\nu(1 + \bar{w}_\nu) = -\dot{\phi} \overline{\beta(\phi) \rho_\nu (1 - 3w_\nu)} \\ \ddot{\phi} + 3H\dot{\phi} + a^2 \partial_\phi V(\phi) = a^2 \overline{\beta(\phi) \rho_\nu (1 - 3w_\nu)} \end{array} \right. \quad (6.38)$$

where $\vec{\rho}$ is interpolated from the previous $\bar{\rho}$ solution. The derivatives of the homogeneous solution of the field $\bar{\phi}$ are then used to update it.

- *Solve the scalar field perturbations:*

The previous homogeneous quantities are used to compute the solution of the field $u_{i,j,k} \equiv \phi_{i,j,k}$ of Eq. 6.35 through the multi-grid NGS solver described in Section 6.2. The exponential form of the field $u_{i,j,k} \equiv e^{\phi_{i,j,k}}$ can be chosen as well.

- *Mesh to particle mapping:*

Once the values of the scalar field ϕ are found for each adaptive mesh cell, they are used to update particle masses $m(\phi)$ as in Eq. 6.11 and its spatial derivative $\vec{\nabla}\phi$, related to the fifth force, is applied to compute the total particle acceleration as in Eq. 6.10

- *Back-reaction:*

Using both the new solution of the field and the new masses of neutrinos, the *back-reaction* contribution of the two species to the background H evolution is calculated, and the total $H(a)$ is calculated on the fly

As we showed, the implementation we presented is based on a generalisation of coupled dark energy and modified gravity models, that is able to perform accurate and computationally efficient simulations of a very wide range of cosmological models. GNQ is one of the theoretical models for which this new implementation of P-GADGET3 could provide precise numerical predictions at the largest scales, thus verifying or falsifying the model itself.

The flexibility of the multi-grid NGS solver introduced can indeed open the door to a lot of numerical simulations for models in which the solution of a non-linear Poisson equation is involved. In the future, we plan to apply this new module to probe a vast number of Coupled Dark Energy and Modified Gravity models beyond Λ CDM, exploring different scales and regimes. This step was not possible during the time-frame of the present Ph.D. work due to lack of time, but will be pursued in the near future.

Part IV

Conclusions

7

Discussion & Conclusions

In the Λ CDM framework, the large-scale structure formation and the late-time accelerated expansion of the Universe are driven by dark matter and dark energy, respectively. Despite multiple evidence on a wide range of scales are consistent with the presence of the two, the fundamental nature of this dark component is still elusive. Indeed, it is still unknown whether these components of the *dark sector* consist of a yet undetected fundamental particle within the Standard Model of particle physics, an underlying scalar – or more complex – field, or they represent an indirect effect of some modification of Einstein’s General Relativity theory of gravity.

In particular, the failure of detecting heavy dark matter particle candidates – such as WIMPs – both indirectly, through decay/annihilation signals from the cores of massive astrophysical structures (see e.g. [Albert *et al.*, 2017](#)), and directly, through dark matter scattering recoil signals (see e.g. [Danninger, 2017](#)) or the signatures of supersymmetry in high-energy collisions experiments as the LHC at CERN (see e.g.

Buonaura, 2018), has posed serious challenges to the solution of this enigma. Moreover, the apparent inconsistencies of the standard cosmological model at small-scales – e.g. the cusp-core problem (Oh *et al.*, 2011), the missing satellite problem (Klypin *et al.*, 1999) or the too-big-to-fail problem (Boylan-Kolchin *et al.*, 2012) – could be related to underlying fundamental nature of dark matter.

The new generation of wide-field and high-precision surveys – e.g. Euclid (Lau-reijs *et al.*, 2011), LSST (Ivezic *et al.*, 2008), and SKA (Blake *et al.*, 2004) – will tackle this problem, reaching an unprecedented observational accuracy that will demand theoretical predictions of comparable quality in return. The need for precise and statistically significant predictions will be supplied by refined cosmological numerical simulations, which should be able to verify theoretical models and disentangle the possible degeneracies arising between different descriptions. Since this great amount of data is going to probe also the highly non-linear regime of large-scale structure evolution, more sophisticated numerical techniques will be required to improve the description of non-linear systems.

Our main project involved the numerical implementation of an intriguing alternative to the standard collision-less dark matter scenario, called *Fuzzy Dark Matter* (Hu *et al.*, 2000). In this model, dark matter is represented by an extremely light non-thermal boson field which, due to its corresponding tiny mass, exhibits quantum behaviours at cosmological scales. The effective description of this dark matter flavour is one of a self-interacting fluid, that experiences the repulsive net effect of a highly non-linear *Quantum Potential*, accounting for decoherence and interference processes.

In this thesis, we presented the AX-GADGET code (Nori and Baldi, 2018) featuring an efficient and accurate implementation of the Quantum Potential that characterises Fuzzy Dark Matter models and in particular *Ultra Light Axion* particles as candidates for the cosmological budget of dark matter. We have described the algorithm implemented in the code, the strategies we adopted to improve its accuracy compared to standard SPH techniques, and shown tests for analytical density distributions. We recovered the formation of a stable solitonic core within a dark matter halo, which is a characteristic aspect of Fuzzy Dark Matter models. We have also

employed the code for realistic cosmological simulations, showing that a consistent treatment of the Quantum Potential in the dynamical evolution of the system is necessary to account for the full suppression of power at small scales that represents the most prominent observational feature of Fuzzy Dark Matter scenarios.

We have also presented the results of a cosmological application of the AX-GADGET code: for the first time in the literature, we performed a suite of hydrodynamical simulations of a statistically significant volume of the universe for Fuzzy Dark Matter models, featuring a fully consistent implementation of the Quantum Potential effects on the dynamical evolution of the system (Nori *et al.*, 2018). These simulations allowed to perform for the first time a fully consistent comparison of mock Lyman- α observations with available data and to update existing constraints on the allowed FDM mass range. As the new constraints are tighter but not significantly different from previous ones, this represents the first direct validation of the effectiveness of gravitational recovery of the intermediate suppressed scales that are involved with the Lyman- α observations. Furthermore, our large halo sample allowed us to perform an extensive characterisation of the properties of dark matter haloes in the context of FDM scenarios, highlighting the scaling relations that link the typical mass scale below which FDM effects start to appear. Moreover, we observed a systematic mass transfer from smaller to bigger collapsed structures, that has never been noticed before, due to the limited statistical sample of collapsed objects in FDM simulations in the literature. Higher resolution simulations will soon allow us to explore even smaller scales where we expect to observe the formation of solitonic cores. We also plan to expand our halo sample to investigate the mass transfer mechanism and its possible observational consequences.

Finally, we presented a project regarding a more general simulation approach to strongly coupled models that is still in progress. In particular, it involves the combination of particle-based and grid-based approaches to study a wide range of theoretical models featuring a scalar field coupled with one or more matter species. Our generalised approach is flexible and adaptable to different Coupled Dark Energy and Modified Gravity models, including for example $f(R)$ and Growing Neutrino Quintessence. The technical implementation regards the extension of the multi-grid Newton–Gauss–Seidel scheme encoded in MG-GADGET (Puch-

wein et al., 2013) to account for different parameters and functions, as well as relativistic aspects of the fluid involved. This new approach will allow us to probe unexplored scales and regimes of such strongly coupled models – as e.g. Growing Neutrino Quintessence to the largest scales –, for which numerical simulations were numerically prohibitive.

To conclude, we have developed sophisticated numerical tools for highly non-linear dark matter simulations, that are able to follow accurately the non-linear dynamics of interacting models. We have mixed and refined particle-based and grid-based techniques to reduce sensibly the computational cost with respect to other codes in the literature, allowing simulations of scales that have been so far unexplored. When applied to cosmological set-ups, accurate theoretical predictions were achieved and constraints on the model parameters have been set in the comparison with observations. In conclusion, we believe that these new simulation modules could have a valuable and significant role in the era of Precision Cosmology.

7.1 Future Prospects

In the next years, I plan to focus my research activity on the mathematical modelling and numerical implementation of cosmological models beyond the standard scenario.

With the use of the AX-GADGET code, I intend to explore the Fuzzy Dark Matter scenario down to smaller and smaller cosmological scales to investigate halo distribution, abundance and peculiar properties and to characterise the impact of the wave-like interference features that are expected to appear at galactic scales. In particular, I will focus on the formation of solitonic cores at the centre of dark matter haloes and their dynamics, performing high-resolution zoom simulations of Milky-way-like systems as well as studying configurations of colliding objects -- i.e. in Bullet-cluster-like systems -. The estimation of observables like galaxy-galaxy lensing in Fuzzy Dark Matter cosmologies will be also object of investigation, which can be a powerful tool to constrain the mass of the ultra-light boson.

As an interesting by-product, the small-scales simulations performed with AX-GADGET can be used to probe the theoretical and numerical limits of the statistical (and fluid) representation of quantum fields, namely exploring the numerical evolution of many-body quantum systems in the De-Broglie-Bohm interpretation of quantum mechanics. I intend to study this aspect and use AX-GADGET as an exciting test bench to examine the extent of the theoretical and numerical equivalence between a particle-based and field-based approaches in the description of quantum systems.

The use of statistical techniques, that largely characterizes complex systems in other fields like biophysics, image processing, and econometrics, has raised interest in the astrophysics field in recent years. I plan to expand the post-process analysis of cosmological simulations with advanced statistical observables as the one involved in Machine-Learning algorithms, in order to fully exploit the information encoded. In fact, the outstanding amount of forthcoming observational and simulated cosmological data is going to challenge the community to adopt new procedures to store it, condense it and extract meaningful information out of it.

I also intend to expand my research to alternative scenarios of Dark Energy and Modified Gravity and their interaction with matter species, applying our generalized implementation of strongly coupled scenarios in the P-GADGET3 code to several cases as Growing Neutrino Quintessence, Lorentz violating theories of gravity, Clustering Dark Energy and other of coupled Dark Energy and Modified Gravity models that can be described through interactions between matter and a scalar field. In this way, it will be possible to predict the effects of different models on astrophysical observables using the same code, contributing to the understanding of the physical mechanisms that originate the accelerated cosmic expansion of the Universe.

BIBLIOGRAPHY

Aarseth, S.J. (1963). Dynamical evolution of clusters of galaxies, I. *Mon. Not. Roy. Astron. Soc.*, **126**, 223.

Aarseth, S.J., Gott, III, J.R. and Turner, E.L. (1979). N-body simulations of galaxy clustering. I - Initial conditions and galaxy collapse times. *Astrophys. J.*, **228**, 664–683.

Abbott, B.P. et al (2017). Gw170817: Observation of gravitational waves from a binary neutron star inspiral. *Phys. Rev. Lett.*, **119**, 161101.

Achitouv, I., Baldi, M., Puchwein, E. and Weller, J. (2016). Imprint of $f(R)$ gravity on nonlinear structure formation. *Phys. Rev.*, **D93(10)**, 103522.

Ade, P.A.R. et al (2016). Planck 2015 results. XIII. Cosmological parameters. *Astron. Astrophys.*, **594**, A13.

Afshordi, N., Zaldarriaga, M. and Kohri, K. (2005). On the stability of dark energy with mass-varying neutrinos. *Phys. Rev.*, **D72**, 065024.

Alam, S. et al (2017). The clustering of galaxies in the completed SDSS-III Baryon Oscillation Spectroscopic Survey: cosmological analysis of the DR12 galaxy sample. *Mon. Not. Roy. Astron. Soc.*, **470**, 2617–2652.

Albert, A. et al (2017). Searching for Dark Matter Annihilation in Recently Discovered Milky Way Satellites with Fermi-LAT. *Astrophys. J.*, **834(2)**, 110.

Alimi, J.M. et al (2010). Imprints of dark energy on cosmic structure formation - I. Realistic quintessence models and the non-linear matter power spectrum. *Mon. Not. Roy. Astron. Soc.*, **401**, 775–790.

- Alpher, R.A. and Herman, R. (1948). Evolution of the universe. *Nature*, **162**, 774 EP –.
- Alpher, R.A., Bethe, H. and Gamow, G. (1948). The origin of chemical elements. *Phys. Rev.*, **73**, 803–804.
- Amendola, L. (2000). Coupled quintessence. *Phys. Rev.*, **D62**, 043511.
- Amendola, L. (2004). Linear and non-linear perturbations in dark energy models. *Phys. Rev.*, **D69**, 103524.
- Amendola, L. et al (2018). Cosmology and fundamental physics with the Euclid satellite. *Living Rev. Rel.*, **21**(1), 2.
- Amendola, L., Quercellini, C., Tocchini-Valentini, D. and Pasqui, A. (2003). Cosmic microwave background as a gravity probe. *The Astrophysical Journal Letters*, **583**(2), L53.
- Amendola, L., Baldi, M. and Wetterich, C. (2008). Quintessence cosmologies with a growing matter component. *Phys. Rev.*, **D78**, 023015.
- Angulo, R.E., Hahn, O. and Abel, T. (2013). The warm dark matter halo mass function below the cut-off scale. *Mon. Not. Roy. Astron. Soc.*, **434**, 3337–3347.
- Arinyo-i Prats, A., Miralda-Escudé, J., Viel, M. and Cen, R. (2015). The Non-Linear Power Spectrum of the Lyman Alpha Forest. *JCAP*, **1512**(12), 017.
- Armengaud, E., Palanque-Delabrouille, N., Marsh, D.J.E., Baur, J. and Yèche, C. (2017). Constraining the mass of light bosonic dark matter using SDSS Lyman- α forest. *Mon. Not. Roy. Astron. Soc.*, **471**(4), 4606–4614.
- Arnold, C., Puchwein, E. and Springel, V. (2015). The Lyman α forest in $f(R)$ modified gravity. *Mon. Not. Roy. Astron. Soc.*, **448**(3), 2275–2283.
- Arnold, C., Springel, V. and Puchwein, E. (2016). Zoomed cosmological simulations of Milky Way-sized haloes in $f(R)$ gravity. *Mon. Not. Roy. Astron. Soc.*, **462**(2), 1530–1541.
- Ayaita, Y., Weber, M. and Wetterich, C. (2009). Peculiar Velocity Anomaly from Forces Beyond Gravity?
- Ayaita, Y., Weber, M. and Wetterich, C. (2012). Structure formation and backreaction in growing neutrino quintessence. *Physical Review D*, **85**(12), 123010.

- Ayaita, Y., Baldi, M., Führer, F., Puchwein, E. and Wetterich, C. (2016). Nonlinear growing neutrino cosmology. *Phys. Rev.*, D93(6), 063511.
- Baccigalupi, C., Matarrese, S. and Perrotta, F. (2000). Tracking extended quintessence. *Phys. Rev. D*, 62, 123510.
- Bahcall, N.A. and Fan, X.h. (1998). The Most massive distant clusters: Determining Ω_m and σ_8 . *Astrophys. J.*, 504, 1.
- Baldi, M. (2012). Dark Energy Simulations. *Phys. Dark Univ.*, 1, 162–193.
- Baldi, M. (2012). Multiple dark matter as a self-regulating mechanism for dark sector interactions. *Annalen der Physik*, 524, 602–617.
- Baldi, M., Pettorino, V., Robbers, G. and Springel, V. (2010). Hydrodynamical N-body simulations of coupled dark energy cosmologies. *Mon. Not. Roy. Astron. Soc.*, 403, 1684–1702.
- Baldi, M., Pettorino, V., Amendola, L. and Wetterich, C. (2011). Oscillating nonlinear large scale structure in growing neutrino quintessence. *Mon. Not. Roy. Astron. Soc.*, 418, 214.
- Balsara, D.S. (1995). Von neumann stability analysis of smoothed particle hydrodynamics: suggestions for optimal algorithms. *Journal of Computational Physics*, 121(2), 357 – 372.
- Bartolo, N., Corasaniti, P.S., Liddle, A.R. and Malquarti, M. (2004). Perturbations in cosmologies with a scalar field and a perfect fluid. *Phys. Rev. D*, 70, 043532.
- Bean, R., Flanagan, E.E., Laszlo, I. and Trodden, M. (2008). Constraining Interactions in Cosmology’s Dark Sector. *Phys. Rev.*, D78, 123514.
- Bekenstein, J.D. (2004). Relativistic gravitation theory for the MOND paradigm. *Phys. Rev.*, D70, 083509. [Erratum: *Phys. Rev.* D71, 069901(2005)].
- Bel, J. et al (2014). The VIMOS Public Extragalactic Redshift Survey (VIPERS). Ω_{m0} from the galaxy clustering ratio measured at $z \sim 1$. *A&A*, 563, A37.
- Bennett, C.L. et al (2013). Nine-year wilkinson microwave anisotropy probe (wmap) observations: Final maps and results. *The Astrophysical Journal Supplement Series*, 208(2), 20.

- Bernstein, G.M. et al (2002). Volume-phase holographic spectrograph for the Magellan telescopes. In A. M. Larar and M. G. Mlynczak, editors, *Optical Spectroscopic Techniques, Remote Sensing, and Instrumentation for Atmospheric and Space Research IV*, volume 4485 of *Proceedings of the SPIE*, pages 453–459.
- Berti, E. et al (2015). Testing General Relativity with Present and Future Astrophysical Observations. *Class. Quant. Grav.*, **32**, 243001.
- Bertone, G., Hooper, D. and Silk, J. (2005). Particle dark matter: Evidence, candidates and constraints. *Phys. Rept.*, **405**, 279–390.
- Bertotti, B., Iess, L. and Tortora, P. (2003). A test of general relativity using radio links with the cassini spacecraft. *Nature*, **425**, 374 EP –.
- Blake, C.A., Abdalla, F.B., Bridle, S.L. and Rawlings, S. (2004). Cosmology with the Square Kilometre Array. *New Astron. Rev.*, **48**, 1063–1077.
- Bode, P., Bahcall, N.A., Ford, E.B. and Ostriker, J.P. (2001a). Evolution of the cluster mass function: Gpc^3 dark matter simulations. *Astrophys. J.*, **551**, 15–22.
- Bode, P., Ostriker, J.P. and Turok, N. (2001b). Halo formation in warm dark matter models. *Astrophys. J.*, **556**, 93–107.
- Boehmer, C.G. and Harko, T. (2007). Can dark matter be a Bose-Einstein condensate? *JCAP*, **0706**, 025.
- Bohm, D. (1952). A Suggested Interpretation of the Quantum Theory in Terms of “Hidden” Variables. I. *Physical Review*, **85**, 166–179.
- Bolton, J.S. et al (2017). The Sherwood simulation suite: overview and data comparisons with the Lyman α forest at redshifts $2 \leq z \leq 5$. *Mon. Not. Roy. Astron. Soc.*, **464**(1), 897–914.
- Bond, J.R. and Efstathiou, G. (1984). Cosmic background radiation anisotropies in universes dominated by nonbaryonic dark matter. *The Astrophysical Journal*, **285**, L45.
- Bondi, H. and Gold, T. (1948). The Steady-State Theory of the Expanding Universe. *Mon. Not. Roy. Astron. Soc.*, **108**, 252.
- Bonometto, S.A., Sassi, G. and La Vacca, G. (2012). Dark energy from dark radiation in strongly coupled cosmologies with no fine tuning. *JCAP*, **1208**, 015.

- Bosma, A. (1981). 21-cm line studies of spiral galaxies. 2. The distribution and kinematics of neutral hydrogen in spiral galaxies of various morphological types. *Astron. J.*, **86**, 1825.
- Boyardsky, A., Lesgourgues, J., Ruchayskiy, O. and Viel, M. (2009). Lyman-alpha constraints on warm and on warm-plus-cold dark matter models. *JCAP*, **0905**, 012.
- Boylan-Kolchin, M., Bullock, J.S. and Kaplinghat, M. (2012). The Milky Way's bright satellites as an apparent failure of LCDM. *Mon. Not. Roy. Astron. Soc.*, **422**, 1203–1218.
- Bramble, J. (1993). *Multigrid Methods*. Chapman & Hall/CRC Research Notes in Mathematics Series. Taylor & Francis.
- Brax, P. and Martin, J. (1999). Quintessence and supergravity. *Phys. Lett.*, **B468**, 40–45.
- Briggs, W.L., Henson, V.E. and McCormick, S.F. (2000). *A Multigrid Tutorial, Second Edition*. Society for Industrial and Applied Mathematics.
- Brookfield, A.W., van de Bruck, C. and Hall, L.M.H. (2008). New interactions in the dark sector mediated by dark energy. *Phys. Rev.*, **D77**, 043006.
- Brooks, A.M., Kuhlen, M., Zolotov, A. and Hooper, D. (2013). A Baryonic Solution to the Missing Satellites Problem. *Astrophys. J.*, **765**, 22.
- Brookshaw, L. (1985). A method of calculating radiative heat diffusion in particle simulations. In *Proceedings of the Astronomical Society of Australia*, volume 6, pages 207–210.
- Brouzakis, N., Pettorino, V., Tetradis, N. and Wetterich, C. (2011). Nonlinear matter spectra in growing neutrino quintessence. *JCAP*, **1103**, 049.
- Buchdahl, H.A. (1970). Non-linear Lagrangians and cosmological theory. *Mon. Not. Roy. Astron. Soc.*, **150**, 1.
- Buonaura, A. (2018). Status and physics of the SHiP experiment at CERN. *PoS*, **DIS2017**, 079.
- Cai, Y.F., Capozziello, S., De Laurentis, M. and Saridakis, E.N. (2016). $f(T)$ teleparallel gravity and cosmology. *Rept. Prog. Phys.*, **79**(10), 106901.
- Carlberg, R.G. and Couchman, H.M.P. (1989). Mergers and bias in a cold dark matter cosmology. *Astrophys. J.*, **340**, 47–68.

- Casas, S., Pettorino, V. and Wetterich, C. (2016). Dynamics of neutrino lumps in growing neutrino quintessence. *Phys. Rev.*, **D94**(10), 103518.
- Cataneo, M. et al (2015). New constraints on $f(R)$ gravity from clusters of galaxies. *Phys. Rev.*, **D92**(4), 044009.
- Chavanis, P.H. (2012). Growth of perturbations in an expanding universe with Bose-Einstein condensate dark matter. *A&A*, **537**, A127.
- Chesler, P.M. and Loeb, A. (2017). Constraining Relativistic Generalizations of Modified Newtonian Dynamics with Gravitational Waves. *Phys. Rev. Lett.*, **119**(3), 031102.
- Cleary, P.W. and Monaghan, J.J. (1999). Conduction modelling using smoothed particle hydrodynamics. *Journal of Computational Physics*, **148**(1), 227 – 264.
- Clowe, D. et al (2006). A direct empirical proof of the existence of dark matter. *Astrophys. J.*, **648**, L109–L113.
- Colberg, J.M. et al (2000). Clustering of galaxy clusters in CDM universes. *Mon. Not. Roy. Astron. Soc.*, **319**, 209.
- Coles, P. and Lucchin, F. (2002). *Cosmology: The Origin and Evolution of Cosmic Structure*. Wiley.
- Colin, F., Egli, R. and Lin, F.Y. (2006). Computing a null divergence velocity field using smoothed particle hydrodynamics. *J. Comput. Phys.*, **217**(2), 680–692.
- Courant, R., Friedrichs, K. and Lewy, H. (1928). über die partiellen differenzengleichungen der mathematischen physik. *Mathematische Annalen*, **100**(1), 32–74.
- Creminelli, P., D’Amico, G., Norena, J. and Vernizzi, F. (2009). The Effective Theory of Quintessence: the $w < -1$ Side Unveiled. *JCAP*, **0902**, 018.
- Crocce, M., Pueblas, S. and Scoccimarro, R. (2006). Transients from Initial Conditions in Cosmological Simulations. *Mon. Not. Roy. Astron. Soc.*, **373**, 369–381.
- Damour, T., Gibbons, G.W. and Gundlach, C. (1990). Dark matter, time-varying g , and a dilaton field. *Phys. Rev. Lett.*, **64**, 123–126.
- Danninger, M. (2017). Review of indirect detection of dark matter with neutrinos. *J. Phys. Conf. Ser.*, **888**(1), 012039.

- Davis, M., Efstathiou, G., Frenk, C.S. and White, S.D.M. (1985). The evolution of large-scale structure in a universe dominated by cold dark matter. *Astrophys. J.*, **292**, 371–394.
- de Bernardis, P. et al (2000). A flat universe from high-resolution maps of the cosmic microwave background radiation. *Nature*, **404**, 955 EP –.
- De Felice, A. and Tsujikawa, S. (2010). $f(R)$ theories. *Living Rev. Rel.*, **13**, 3.
- Dehnen, W. and Aly, H. (2012). Improving convergence in smoothed particle hydrodynamics simulations without pairing instability. *Mon. Not. Roy. Astron. Soc.*, **425**, 1068–1082.
- Duncan, M.J., Levison, H.F. and Lee, M.H. (1998). A Multiple Time Step Symplectic Algorithm for Integrating Close Encounters. *Astronomic. J.*, **116**, 2067–2077.
- Dvali, G.R., Gabadadze, G. and Porrati, M. (2000). 4-D gravity on a brane in 5-D Minkowski space. *Phys. Lett.*, **B485**, 208–214.
- Efstathiou, G. and Bond, J.R. (1986). Microwave background fluctuations and dark matter. *Philosophical Transactions of the Royal Society A: Mathematical, Physical and Engineering Sciences*, **320**(1556), 585–594.
- Efstathiou, G. and Eastwood, J.W. (1981). On the clustering of particles in an expanding universe. *Mon. Not. Roy. Astron. Soc.*, **194**, 503–525.
- Efstathiou, G., Sutherland, W.J. and Maddox, S.J. (1990). The cosmological constant and cold dark matter. *Nature*, **348**, 705 EP –.
- Einstein, A. (1905). On the electrodynamics of moving bodies. *Annalen Phys.*, **17**, 891–921. [Annalen Phys.14,194(2005)].
- Einstein, A. (1916). The Foundation of the General Theory of Relativity. *Annalen Phys.*, **49**(7), 769–822. [,65(1916)].
- Einstein, A. (1917). Kosmologische Betrachtungen zur allgemeinen Relativitätstheorie. *Sitzungsberichte der Königlich Preußischen Akademie der Wissenschaften (Berlin)*, Seite 142-152.
- Eisenstein, D.J. and Hu, W. (1998). Baryonic features in the matter transfer function. *Astrophys. J.*, **496**, 605.
- Ferreira, P.G. and Joyce, M. (1998). Cosmology with a primordial scaling field. *Phys. Rev. D*, **58**, 023503.

- Feyerabend, P. (1975). *Against Method: Outline of an Anarchist Theory of Knowledge*. New Left Books.
- Forest, E. (1989). *Canonical integrators as tracking codes (or how to integrate perturbation theory with tracking)*. American Institute of Physics, United States.
- Frenk, C.S., White, S.D.M. and Davis, M. (1983). Nonlinear evolution of large-scale structure in the universe. *Astrophys. J.*, **271**, 417–430.
- Friedmann, A. (1924). Über die möglichkeit einer welt mit konstanter negativer krümmung des raumes. *Zeitschrift für Physik*, **21**(1), 326–332.
- Frigo, M. and Johnson, S.G. (2005). The design and implementation of fftw3. In *PROCEEDINGS OF THE IEEE*, pages 216–231.
- Führer, F. and Wetterich, C. (2015). Backreaction in growing neutrino quintessence. *Physical Review D*, **91**(12), 123542.
- Galassi, M.e.a. (2018). Gnu scientific library reference manual.
- Gasperini, M., Piazza, F. and Veneziano, G. (2001). Quintessence as a runaway dilaton. *Phys. Rev. D*, **65**, 023508.
- Gelb, J.M. and Bertschinger, E. (1994). Cold dark matter. 1: The Formation of dark halos. *Astrophys. J.*, **436**, 467.
- Gingold, R.A. and Monaghan, J.J. (1977). Smoothed particle hydrodynamics - Theory and application to non-spherical stars. *Mon. Not. Roy. Astron. Soc.*, **181**, 375–389.
- Governato, F. et al (1999). Properties of galaxy clusters. Mass and correlation functions. *Mon. Not. Roy. Astron. Soc.*, **307**, 949.
- Gross, E.P. (1961). Structure of a quantized vortex in boson systems. *Il Nuovo Cimento*, **20**, 454–477.
- Gunn, J.E. and Gott, III, J.R. (1972). On the Infall of Matter Into Clusters of Galaxies and Some Effects on Their Evolution. *Astrophys. J.*, **176**, 1.
- Guth, A.H. (1981). Inflationary universe: A possible solution to the horizon and flatness problems. *Phys. Rev. D*, **23**, 347–356.

- Guzman, F.S. and Urena-Lopez, L.A. (2006). Gravitational cooling of self-gravitating Bose-Condensates. *Astrophys. J.*, **645**, 814–819.
- Harlow, F.H. (1988). Pic and its progeny. *Computer Physics Communications*, **48**(1), 1 – 10.
- Heymans, C. et al (2013). CFHTLenS tomographic weak lensing cosmological parameter constraints: Mitigating the impact of intrinsic galaxy alignments. *Mon. Not. Roy. Astron. Soc.*, **432**, 2433–2453.
- Hildebrandt, H. et al (2017). KiDS-450: cosmological parameter constraints from tomographic weak gravitational lensing. *Mon. Not. Roy. Astron. Soc.*, **465**, 1454–1498.
- Hinterbichler, K. and Khoury, J. (2010). Symmetron Fields: Screening Long-Range Forces Through Local Symmetry Restoration. *Phys. Rev. Lett.*, **104**, 231301.
- Hlozek, R., Grin, D., Marsh, D.J.E. and Ferreira, P.G. (2015). A search for ultralight axions using precision cosmological data. *Phys. Rev.*, **D91**(10), 103512.
- Hockney, R.W. and Eastwood, J.W. (1981). *Computer Simulation Using Particles*.
- Hu, W. and Sawicki, I. (2007). Models of $f(R)$ Cosmic Acceleration that Evade Solar-System Tests. *Phys. Rev.*, **D76**, 064004.
- Hu, W. and White, M. (1996). Acoustic signatures in the cosmic microwave background. *The Astrophysical Journal*, **471**(1), 30–51.
- Hu, W., Barkana, R. and Gruzinov, A. (2000). Cold and fuzzy dark matter. *Phys. Rev. Lett.*, **85**, 1158–1161.
- Hubble, E. (1929). A Relation between Distance and Radial Velocity among Extra-Galactic Nebulae. *Proceedings of the National Academy of Science*, **15**, 168–173.
- Hubble, E. and Humason, M.L. (1931). The Velocity-Distance Relation among Extra-Galactic Nebulae. *Astrophys. J.*, **74**, 43.
- Huey, G. and Wandelt, B.D. (2006). Interacting quintessence. The Coincidence problem and cosmic acceleration. *Phys. Rev.*, **D74**, 023519.
- Hui, L. and Gnedin, N.Y. (1997). Equation of state of the photoionized intergalactic medium. *Mon. Not. Roy. Astron. Soc.*, **292**, 27.

- Hui, L., Ostriker, J.P., Tremaine, S. and Witten, E. (2017). Ultralight scalars as cosmological dark matter. *Phys. Rev.*, **D95**(4), 043541.
- Iršič, V. et al (2017a). New Constraints on the free-streaming of warm dark matter from intermediate and small scale Lyman- α forest data. *Phys. Rev.*, **D96**(2), 023522.
- Iršič, V. et al (2017b). The Lyman α forest power spectrum from the XQ-100 Legacy Survey. *Mon. Not. Roy. Astron. Soc.*, **466**(4), 4332–4345.
- Iršič, V., Viel, M., Haehnelt, M.G., Bolton, J.S. and Becker, G.D. (2017c). First constraints on fuzzy dark matter from Lyman- α forest data and hydrodynamical simulations. *Phys. Rev. Lett.*, **119**(3), 031302.
- Ivezic, Z. et al (2008). LSST: from Science Drivers to Reference Design and Anticipated Data Products. *arXiv:0805.2366*.
- Jain, B. and VanderPlas, J. (2011). Tests of Modified Gravity with Dwarf Galaxies. *JCAP*, **1110**, 032.
- Jenkins, A. et al (1998). Evolution of Structure in Cold Dark Matter Universes. *Astrophys. J.*, **499**, 20–40.
- Jubelgas, M., Springel, V. and Dolag, K. (2004). Thermal conduction in cosmological SPH simulations. *Mon. Not. Roy. Astron. Soc.*, **351**, 423.
- Jungman, G., Kamionkowski, M., Kosowsky, A. and Spergel, D.N. (1996). Cosmological-parameter determination with microwave background maps. *Physical Review D*, **54**(2), 1332–1344.
- Kamionkowski, M., Spergel, D.N. and Sugiyama, N. (1994). Small-scale cosmic microwave background anisotropies as probe of the geometry of the universe. *The Astrophysical Journal*, **426**, L57.
- Kaplinghat, M., Knox, L. and Turner, M.S. (2000). Annihilating the cold dark matter cusp crisis. *Phys. Rev. Lett.*, **85**, 3335.
- Kashlinsky, A. (1998). Determining Omega from cluster correlation function. *Phys. Rept.*, **307**, 67–73.
- Kernighan, B.W. and Ritchie, D.M. (1978). *The C Programming Language*.

- Khoury, J. and Weltman, A. (2004). Chameleon cosmology. *Phys. Rev.*, **D69**, 044026.
- Kinoshita, H., Yoshida, H. and Nakai, H. (1991). Symplectic integrators and their application to dynamical astronomy. *Celestial Mechanics and Dynamical Astronomy*, **50**, 59–71.
- Klypin, A.A., Kravtsov, A.V., Valenzuela, O. and Prada, F. (1999). Where are the missing Galactic satellites? *Astrophys. J.*, **522**, 82–92.
- Kobayashi, T., Murgia, R., De Simone, A., Iršič, V. and Viel, M. (2017). Lyman- α constraints on ultralight scalar dark matter: Implications for the early and late universe. *Phys. Rev.*, **D96**(12), 123514.
- Koopmans, L.V.E. and Treu, T. (2003). The structure and dynamics of luminous and dark matter in the early-type lens galaxy of 0047-281 at $z=0.485$. *Astrophys. J.*, **583**, 606–615.
- Koyama, K. (2016). Cosmological Tests of Modified Gravity. *Rept. Prog. Phys.*, **79**(4), 046902.
- Laureijs, R. et al (2011). Euclid Definition Study Report. *ArXiv e-prints*.
- Lemaître, G. (1933). The expanding universe. *Gen. Rel. Grav.*, **29**, 641–680. [Annales Soc. Sci. Bruxelles A53,51(1933)].
- Lewis, A., Challinor, A. and Lasenby, A. (2000). Efficient Computation of CMB anisotropies in closed FRW models. *Astrophys. J.*, **538**, 473–476.
- Li, B. and Zhao, H. (2009). Structure Formation by Fifth Force I: N-Body vs. Linear Simulations. *Phys. Rev.*, **D80**, 044027.
- Li, B., Zhao, G.B., Teyssier, R. and Koyama, K. (2012). ECOSMOG: An Efficient Code for Simulating Modified Gravity. *JCAP*, **1201**, 051.
- Li, Y. and Hu, W. (2011). Chameleon Halo Modeling in $f(R)$ Gravity. *Phys. Rev.*, **D84**, 084033.
- Linde, A.D. (1982). A New Inflationary Universe Scenario: A Possible Solution of the Horizon, Flatness, Homogeneity, Isotropy and Primordial Monopole Problems. *Phys. Lett.*, **108B**, 389–393. [Adv. Ser. Astrophys. Cosmol.3,149(1987)].
- López, S. et al (2016). Xq-100: A legacy survey of one hundred 3.5 5 quasars observed with vlt/x-shooter. *A&A*, **594**, A91.

- Lovell, M.R. et al (2014). The properties of warm dark matter haloes. *Mon. Not. Roy. Astron. Soc.*, **439**, 300–317.
- Lucy, L.B. (1977). A numerical approach to the testing of the fission hypothesis. *Astronomic. J.*, **82**, 1013–1024.
- Ma, C.P., Caldwell, R.R., Bode, P. and Wang, L.M. (1999). The mass power spectrum in quintessence cosmological models. *Astrophys. J.*, **521**, L1–L4.
- Macció, A.V., Quercellini, C., Mainini, R., Amendola, L. and Bonometto, S.A. (2004). N-body simulations for coupled dark energy: Halo mass function and density profiles. *Phys. Rev.*, **D69**, 123516.
- Macció, A.V., Paduroiu, S., Anderhalden, D., Schneider, A. and Moore, B. (2012). Cores in warm dark matter haloes: a Catch 22 problem. *Mon. Not. Roy. Astron. Soc.*, **424**, 1105–1112.
- Maddox, S.J., Efstathiou, G., Sutherland, W.J. and Loveday, J. (1990). Galaxy correlations on large scales. *Mon. Not. Roy. Astron. Soc.*, **242**, 43P–47P.
- Madelung, E. (1927). Quantentheorie in hydrodynamischer form. *Zeitschrift für Physik*, **40**(3), 322–326.
- Marsh, D.J.E. (2015). Nonlinear hydrodynamics of axion dark matter: Relative velocity effects and quantum forces. *Phys. Rev.*, **D91**(12), 123520.
- Marsh, D.J.E. (2016a). Axion Cosmology. *Phys. Rept.*, **643**, 1–79.
- Marsh, D.J.E. (2016b). WarmAndFuzzy: the halo model beyond CDM. *ArXiv e-prints*.
- Marsh, D.J.E. and Ferreira, P.G. (2010). Ultra-Light Scalar Fields and the Growth of Structure in the Universe. *Phys. Rev.*, **D82**, 103528.
- Marsh, D.J.E. and Pop, A.R. (2015). Axion dark matter, solitons and the cusp?core problem. *Mon. Not. Roy. Astron. Soc.*, **451**(3), 2479–2492.
- Masi, S. et al (2002). The BOOMERanG experiment and the curvature of the universe. *Prog. Part. Nucl. Phys.*, **48**, 243–261. [,243(2002)].
- Mateo, M. (1998). Dwarf galaxies of the Local Group. *Ann. Rev. Astron. Astrophys.*, **36**, 435–506.

- McDonald, P. et al (2006). The Lyman-alpha forest power spectrum from the Sloan Digital Sky Survey. *Astrophys. J. Suppl.*, **163**, 80–109.
- Medvedev, M.V. (2014). Cosmological Simulations of Multicomponent Cold Dark Matter. *Phys. Rev. Lett.*, **113**(7), 071303.
- Melott, A.L. and Shandarin, S.F. (1989). Gravitational instability with high resolution. *Astrophys. J.*, **343**, 26–30.
- Milgrom, M. (1983). A modification of the Newtonian dynamics as a possible alternative to the hidden mass hypothesis. *Astrophys. J.*, **270**, 365–370.
- Miyoshi, K. and Kihara, T. (1975). Development of the correlation of galaxies in an expanding universe. *Publications of the Astronomical Society of Japan*, **27**, 333–346.
- Mocz, P. and Succi, S. (2015). Numerical solution of the nonlinear Schrödinger equation using smoothed-particle hydrodynamics. *Phys. Rev.*, **E91**(5), 053304.
- Mocz, P., Lancaster, L., Fialkov, A. and Becerra, F. (2018). On the Schrodinger-Poisson-Vlasov-Poisson correspondence. *ArXiv e-prints*.
- Monaghan, J. (2012). Smoothed particle hydrodynamics and its diverse applications. *Annual Review of Fluid Mechanics*, **44**(1), 323–346.
- Monaghan, J.J. (1992). Smoothed particle hydrodynamics. *Annual review of astronomy and astrophysics*, **30**, 543–574.
- Monaghan, J.J. (1997). SPH and Riemann Solvers. *Journal of Computational Physics*, **136**, 298–307.
- Monaghan, J.J. (2005). Smoothed particle hydrodynamics. *Reports on Progress in Physics*, **68**(8), 1703.
- Monaghan, J.J. and Gingold, R.A. (1983). Shock Simulation by the Particle Method SPH. *Journal of Computational Physics*, **52**, 374–389.
- Moore, B. et al (1999). Dark matter substructure within galactic halos. *Astrophys. J.*, **524**, L19–L22.
- Moré, J.J. (1971). Global convergence of newton-gauss-seidel methods. *SIAM Journal on Numerical Analysis*, **8**(2), 325–336.

- Mota, D.F., Pettorino, V., Robbers, G. and Wetterich, C. (2008). Neutrino clustering in growing neutrino quintessence. *Phys. Lett.*, **B663**, 160–164.
- Murgia, R., Iršič, V. and Viel, M. (2018). Novel constraints on non-cold (non-thermal) Dark Matter from Lyman- α forest data. *ArXiv e-prints*.
- Navarro, J.F., Frenk, C.S. and White, S.D.M. (1996). The Structure of cold dark matter halos. *Astrophys. J.*, **462**, 563–575.
- Navarro, J.F., Frenk, C.S. and White, S.D.M. (1997). A Universal density profile from hierarchical clustering. *Astrophys. J.*, **490**, 493–508.
- Nicolis, A., Rattazzi, R. and Trincherini, E. (2009). The Galileon as a local modification of gravity. *Phys. Rev.*, **D79**, 064036.
- Nori, M. and Baldi, M. (2018). AX-GADGET: a new code for cosmological simulations of Fuzzy Dark Matter and Axion models. *Mon. Not. Roy. Astron. Soc.*, **478**, 3935.
- Nori, M., Murgia, R., Iršič, V., Baldi, M. and Viel, M. (2018). Lyman- α forest and non-linear structure characterization in fuzzy dark matter cosmologies. *Monthly Notices of the Royal Astronomical Society*, page sty2888.
- Oh, S.H., de Blok, W.J.G., Brinks, E., Walter, F. and Kennicutt, Jr, R.C. (2011). Dark and luminous matter in THINGS dwarf galaxies. *Astron. J.*, **141**, 193.
- Oman, K.A. et al (2015). The unexpected diversity of dwarf galaxy rotation curves. *Mon. Not. Roy. Astron. Soc.*, **452**, 3650–3665.
- Oyaizu, H. (2008). Nonlinear evolution of $f(r)$ cosmologies. i. methodology. *Phys. Rev. D*, **78**, 123523.
- Oyaizu, H., Lima, M. and Hu, W. (2008). Nonlinear evolution of $f(r)$ cosmologies. ii. power spectrum. *Phys. Rev. D*, **78**, 123524.
- Peacock, J.A. (1999). *Cosmological Physics*.
- Peebles, P.J.E. (1970). Structure of the Coma Cluster of Galaxies. *Astronomic. J.*, **75**, 13.
- Peebles, P.J.E. (1980). *The large-scale structure of the universe*. Princeton University Press Princeton, N.J.

- Peebles, P.J.E. (1993). *Principles of physical cosmology*. Princeton University Press.
- Peel, A., Pettorino, V., Giocoli, C., Starck, J.L. and Baldi, M. (2018). Breaking degeneracies in modified gravity with higher (than 2nd) order weak-lensing statistics.
- Penzias, A.A. and Wilson, R.W. (1965). A Measurement of Excess Antenna Temperature at 4080 Mc/s. *Astrophys. J.*, **142**, 419–421.
- Perlmutter, S. et al (1999). Measurements of Omega and Lambda from 42 high redshift supernovae. *Astrophys. J.*, **517**, 565–586.
- Perrotta, F., Baccigalupi, C. and Matarrese, S. (1999). Extended quintessence. *Phys. Rev. D*, **61**, 023507.
- Persic, M., Salucci, P. and Stel, F. (1996). The Universal rotation curve of spiral galaxies: 1. The Dark matter connection. *Mon. Not. Roy. Astron. Soc.*, **281**, 27.
- Pettorino, V. and Baccigalupi, C. (2008). Coupled and Extended Quintessence: theoretical differences and structure formation. *Phys. Rev.*, **D77**, 103003.
- Pettorino, V., Wintergerst, N., Amendola, L. and Wetterich, C. (2010). Neutrino lumps and the Cosmic Microwave Background. *Phys. Rev.*, **D82**, 123001.
- Pettorino, V., Amendola, L., Baccigalupi, C. and Quercellini, C. (2012). Constraints on coupled dark energy using CMB data from WMAP and South Pole Telescope. *Physical Review D*, **86**(10), 103507.
- Pitaevskii, L.P. (1961). Vortex lines in an imperfect Bose gas. *Sov. Phys. JETP*, **13**(2), 451–454.
- Pizzuti, L. et al (2017). CLASH-VLT: constraints on $f(R)$ gravity models with galaxy clusters using lensing and kinematic analyses. *JCAP*, **1707**(07), 023.
- Planck Collaboration (2018). Planck 2018 results. VI. Cosmological parameters. *ArXiv e-prints*.
- Planck Collaboration et al (2015). Planck 2015 results. XV. Gravitational lensing. *ArXiv e-prints*.
- Power, C. et al (2003). The inner structure of Λ CDM haloes - I. A numerical convergence study. *Mon. Not. Roy. Astron. Soc.*, **338**, 14–34.

- Puchwein, E., Baldi, M. and Springel, V. (2013). Modified Gravity-GADGET: A new code for cosmological hydrodynamical simulations of modified gravity models. *Mon. Not. Roy. Astron. Soc.*, **436**, 348.
- Quinn, T.R., Katz, N., Stadel, J. and Lake, G. (1997). Time stepping N body simulations. *Submitted to: Astrophys. J.*
- Ratra, B. and Peebles, P.J.E. (1988). Cosmological consequences of a rolling homogeneous scalar field. *Phys. Rev. D*, **37**, 3406–3427.
- Riess, A.G. et al (1998). Observational evidence from supernovae for an accelerating universe and a cosmological constant. *Astron. J.*, **116**, 1009–1038.
- Rocha, M. et al (2013). Cosmological Simulations with Self-Interacting Dark Matter I: Constant Density Cores and Substructure. *Mon. Not. Roy. Astron. Soc.*, **430**, 81–104.
- Rubin, V.C., Ford, W.K.J. and Thonnard, N. (1980). Rotational properties of 21 SC galaxies with a large range of luminosities and radii, from NGC 4605 /R = 4kpc/ to UGC 2885 /R = 122 kpc/. *Astrophys. J.*, **238**, 471–487.
- Rugh, S. and Zinkernagel, H. (2002). The quantum vacuum and the cosmological constant problem. *Studies in History and Philosophy of Science Part B: Studies in History and Philosophy of Modern Physics*, **33**(4), 663 – 705.
- Saha, P. and Tremaine, S. (1992). Symplectic integrators for solar system dynamics. *Astronomical J.*, **104**, 1633–1640.
- Sakharov, A.D. (1966). The Initial Stage of an Expanding Universe and the Appearance of a Nonuniform Distribution of Matter. *Soviet Journal of Experimental and Theoretical Physics*, **22**, 241.
- Sanders, R.H. and McGaugh, S.S. (2002). Modified Newtonian dynamics as an alternative to dark matter. *Ann. Rev. Astron. Astrophys.*, **40**, 263–317.
- Schive, H.Y., Tsai, Y.C. and Chiueh, T. (2010). GAMER: a GPU-Accelerated Adaptive Mesh Refinement Code for Astrophysics. *Astrophys. J. Suppl.*, **186**, 457–484.
- Schive, H.Y., Chiueh, T. and Broadhurst, T. (2014). Cosmic Structure as the Quantum Interference of a Coherent Dark Wave. *Nature Phys.*, **10**, 496–499.

- Schive, H.Y., Chiueh, T., Broadhurst, T. and Huang, K.W. (2016). Contrasting Galaxy Formation from Quantum Wave Dark Matter, ψ DM, with Λ CDM, using Planck and Hubble Data. *Astrophys. J.*, **818**(1), 89.
- Schive, H.Y. et al (2017). GAMER-2: a GPU-accelerated adaptive mesh refinement code – accuracy, performance, and scalability. *ArXiv e-prints*.
- Schmidt, B.P. et al (1998). The High Z supernova search: Measuring cosmic deceleration and global curvature of the universe using type Ia supernovae. *Astrophys. J.*, **507**, 46–63.
- Schmidt, F. (2008). Weak Lensing Probes of Modified Gravity. *Phys. Rev.*, **D78**, 043002.
- Schmidt, F. (2010). Dynamical Masses in Modified Gravity. *Phys. Rev.*, **D81**, 103002.
- Schmidt, F., Lima, M.V., Oyaizu, H. and Hu, W. (2009). Non-linear Evolution of f(R) Cosmologies III: Halo Statistics. *Phys. Rev.*, **D79**, 083518.
- Schneider, A., Smith, R.E., Maccio, A.V. and Moore, B. (2012). Nonlinear Evolution of Cosmological Structures in Warm Dark Matter Models. *Mon. Not. Roy. Astron. Soc.*, **424**, 684.
- Sefusatti, E. and Vernizzi, F. (2011). Cosmological structure formation with clustering quintessence. *JCAP*, **1103**, 047.
- Seljak, U., Slosar, A. and McDonald, P. (2006). Cosmological parameters from combining the lyman-alpha forest with cmb, galaxy clustering and sn constraints. *JCAP*, **0610**, 014.
- Silk, J. (1968). Cosmic Black-Body Radiation and Galaxy Formation. *Astrophys. J.*, **151**, 459.
- Smoot, G.F. et al (1992). Structure in the COBE differential microwave radiometer first-year maps. *Astrophys. J. Letters*, **396**, L1–L5.
- Spergel, D.N. and Steinhardt, P.J. (2000). Observational evidence for selfinteracting cold dark matter. *Phys. Rev. Lett.*, **84**, 3760–3763.
- Springel, V. (2005). The Cosmological simulation code GADGET-2. *Mon. Not. Roy. Astron. Soc.*, **364**, 1105–1134.
- Springel, V. et al (2005). Simulating the joint evolution of quasars, galaxies and their large-scale distribution. *Nature*, **435**, 629–636.

- Springel, V. and Hernquist, L. (2002). Cosmological SPH simulations: The Entropy equation. *Mon. Not. Roy. Astron. Soc.*, **333**, 649.
- Springel, V., White, S.D.M., Tormen, G. and Kauffmann, G. (2001). Populating a cluster of galaxies - I. Results at $z=0$. *Mon. Not. Roy. Astron. Soc.*, **328**, 726–750.
- Springel, V. et al (2008). The Aquarius Project: the subhalos of galactic halos. *Mon. Not. Roy. Astron. Soc.*, **391**, 1685–1711.
- Starobinsky, A.A. (1982). Dynamics of Phase Transition in the New Inflationary Universe Scenario and Generation of Perturbations. *Phys. Lett.*, **117B**, 175–178.
- Suginohara, T. and Suto, Y. (1991). Galaxy clustering in cold dark matter scenario with nonvanishing cosmological constant. *Publications of the Astronomical Society of Japan*, **43**, L17–L25.
- Suzuki, M. (1992). General theory of higher-order decomposition of exponential operators and symplectic integrators. *Physics Letters A*, **165**(5), 387 – 395.
- Szewc, K., Pozorski, J. and Minier, J.P. (2012). Analysis of the incompressibility constraint in the smoothed particle hydrodynamics method. *International Journal for Numerical Methods in Engineering*, **92**, 343–369.
- Tsujikawa, S. (2011). Dark energy: investigation and modeling. *370*(2010), 331–402.
- Vainshtein, A. (1972). To the problem of nonvanishing gravitation mass. *Physics Letters B*, **39**(3), 393 – 394.
- Veltmaat, J. and Niemeyer, J.C. (2016). Cosmological particle-in-cell simulations with ultralight axion dark matter. *Phys. Rev.*, **D94**(12), 123523.
- Viel, M., Haehnelt, M.G. and Springel, V. (2004). Inferring the dark matter power spectrum from the Lyman-alpha forest in high-resolution QSO absorption spectra. *Mon. Not. Roy. Astron. Soc.*, **354**, 684.
- Viel, M., Lesgourgues, J., Haehnelt, M.G., Matarrese, S. and Riotto, A. (2005). Constraining warm dark matter candidates including sterile neutrinos and light gravitinos with wmap and the lyman- α forest. *Phys. Rev. D*, **71**(6), 1–10.

- Viel, M., Becker, G.D., Bolton, J.S. and Haehnelt, M.G. (2013a). Warm dark matter as a solution to the small scale crisis: New constraints from high redshift Lyman- α forest data. *Phys. Rev.*, **D88**, 043502.
- Viel, M., Becker, G.D., Bolton, J.S. and Haehnelt, M.G. (2013b). Warm dark matter as a solution to the small scale crisis: New constraints from high redshift Lyman- α forest data. *Phys. Rev.*, **D88**, 043502.
- Vogt, S.S. et al (1994). HIRES: the high-resolution echelle spectrometer on the Keck 10-m Telescope. In D. L. Crawford and E. R. Craine, editors, *Instrumentation in Astronomy VIII*, volume 2198 of *Proceedings of the SPIE*, page 362.
- von Braun-Bates, F., Winther, H.A., Alonso, D. and Devriendt, J. (2017). The $f(R)$ halo mass function in the cosmic web. *JCAP*, **1703(03)**, 012.
- Wambsganss, J., Bode, P. and Ostriker, J.P. (2004). Giant arc statistics in concordance with a concordance LCDM universe. *Astrophys. J.*, **606**, L93–L96.
- Wang, J. and White, S.D.M. (2007). Discreteness effects in simulations of Hot/Warm dark matter. *Mon. Not. Roy. Astron. Soc.*, **380**, 93–103.
- Warren, M.S. and Salmon, J.K. (1993). A parallel hashed oct-tree n-body algorithm. In *Proceedings of the 1993 ACM/IEEE Conference on Supercomputing, Supercomputing '93*, pages 12–21, New York, NY, USA. ACM.
- Warren, M.S. and Salmon, J.K. (1995). A portable parallel particle program. *Computer Physics Communications*, **87(1)**, 266 – 290. Particle Simulation Methods.
- Warren, M.S., Quinn, P.J., Salmon, J.K. and Zurek, W.H. (1992). Dark halos formed via dissipationless collapse: 1. shapes and alignment of angular momentum. *Astrophys. J.*, **399**, 405.
- Watkins, R., Feldman, H.A. and Hudson, M.J. (2009). Consistently Large Cosmic Flows on Scales of 100 Mpc/h: a Challenge for the Standard LCDM Cosmology. *Mon. Not. Roy. Astron. Soc.*, **392**, 743–756.
- Weinberg, S. (1989). The cosmological constant problem. *Rev. Mod. Phys.*, **61**, 1–23.
- Wendland, H. (1995). Piecewise polynomial, positive definite and compactly supported radial functions of minimal degree. *Advances in Computational Mathematics*, **4(1)**, 389–396.

- Wetterich, C. (1988). Cosmology and the fate of dilatation symmetry. *Nuclear Physics B*, 302(4), 668 – 696.
- Wetterich, C. (1995). The Cosmon model for an asymptotically vanishing time dependent cosmological 'constant'. *Astron. Astrophys.*, 301, 321–328.
- White, S.D.M. (1976). The dynamics of rich clusters of galaxies. *Mon. Not. Roy. Astron. Soc.*, 177, 717–733.
- White, S.D.M., Frenk, C.S., Davis, M. and Efstathiou, G. (1987). Clusters, filaments, and voids in a universe dominated by cold dark matter. *Astrophys. J.*, 313, 505–516.
- Will, C.M. (2006). The confrontation between general relativity and experiment. *Living Reviews in Relativity*, 9(1), 3.
- Wintergerst, N. and Pettorino, V. (2010). Clarifying spherical collapse in coupled dark energy cosmologies. *Phys. Rev.*, D82, 103516.
- Wintergerst, N., Pettorino, V., Mota, D.F. and Wetterich, C. (2010). Very large scale structures in growing neutrino quintessence. *Phys. Rev.*, D81, 063525.
- Winther, H.A. et al (2015). Modified Gravity N-body Code Comparison Project. *Mon. Not. Roy. Astron. Soc.*, 454(4), 4208–4234.
- Woo, T.P. and Chiueh, T. (2009). High-resolution simulation on structure formation with extremely light bosonic dark matter. *The Astrophysical Journal*, 697(1), 850.
- Yoshida, H. (1990). Construction of higher order symplectic integrators. *Physics Letters A*, 150(5), 262 – 268.
- Yoshida, H. (1993). Recent Progress in the Theory and Application of Symplectic Integrators. *Celestial Mechanics and Dynamical Astronomy*, 56, 27–43.
- Zhao, G.B., Li, B. and Koyama, K. (2011). N-body Simulations for $f(R)$ Gravity using a Self-adaptive Particle-Mesh Code. *Phys. Rev.*, D83, 044007.
- Zhao, H., Macciò, A.V., Li, B., Hoekstra, H. and Feix, M. (2010). Structure Formation by Fifth Force: Power Spectrum from N-Body Simulations. *Astrophys. J. Letters*, 712, L179–L183.

Zlatev, I., Wang, L. and Steinhardt, P.J. (1999). Quintessence, cosmic coincidence, and the cosmological constant. *Phys. Rev. Lett.*, **82**, 896–899.

Zurek, W.H., Quinn, P.J., Salmon, J.K. and Warren, M.S. (1994). Large-scale structure after COBE: Peculiar velocities and correlations of cold dark matter halos. *Astrophys. J.*, **431**, 559–568.

Zwicky, F. (1937). On the Masses of Nebulae and of Clusters of Nebulae. *Astrophys. J.*, **86**, 217–246.